RICE UNIVERSITY

Synthesis and Characterization of Three Dimensional Nanostructures Based on Interconnected Carbon Nanomaterials
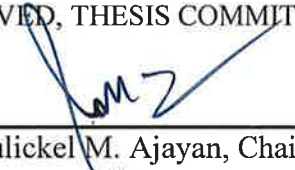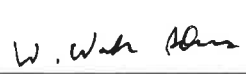
by

Ryota Koizumi

A THESIS SUBMITTED
IN PARTIAL FULFILLMENT OF THE
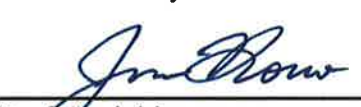REQUIREMENTS FOR THE DEGREE

Master of Science

APPROVED, THESIS COMMITTEE

Prof. Pulickel M. Ajayan, Chair
Benjamin M. and Mary Greenwood
Anderson Professor of Engineering, Chair
of Materials Science and NanoEngineering

Dr. W. Wade Adams
Senior Faculty Fellow

Prof. Junichiro Kono
Professor of Electrical and Computer
Engineering; Professor of Physics and
Astronomy

HOUSTON, TEXAS
May 2016

ABSTRACT

Synthesis and Characterization of Three Dimensional Nanostructures Based on Interconnected Carbon Nanomaterials

by

Ryota Koizumi

This thesis addresses various types of synthetic methods for novel three dimensional nanomaterials and nanostructures based on interconnected carbon nanomaterials using solution chemistry and chemical vapor deposition (CVD) methods. Carbon nanotube (CNT) spheres with porous and scaffold structures consisting of interconnected CNTs were synthesized by solution chemistry followed by freeze-drying, which have high elasticity under nano-indentation tests. This allows the CNT spheres to be potentially applied to mechanical dampers. CNTs were also grown on two dimensional materials--such as reduced graphene oxide (rGO) and hexagonal boron nitride (h-BN)--by CVD methods, which are chemically interconnected. CNTs on rGO and h-BN interconnected structures performed well as electrodes for supercapacitors. Furthermore, unique interconnected flake structures of alpha-phase molybdenum carbide were developed by a CVD method. The molybdenum carbide can be used for a catalyst of hydrogen evolution reaction activity as well as an electrode for supercapacitors.

Acknowledgments

I would like to begin by thanking my advisor, Professor Pulickel M. Ajayan, for all of the support and advice he has provided. I greatly appreciated the insight he provided and the sharing of his extensive knowledge with me. I am also extremely grateful to Dr. Robert Vajtai for all of the opportunities he has given me throughout my stay at Rice University. Dr. Vajtai has always taken the time to support me and has given plenty of advices not only for my research projects but also for course work when I was taking his courses. I would also like to thank Professor Junichiro Kono for his warmhearted assistance since I arrived in Houston. I deeply appreciate him for taking the time out to serve on my thesis committee and to provide a new perspective on my work. I would also like to express my gratitude to Dr. Walter Wade Adams for being on my thesis committee and giving me fruitful advice.

I am grateful to Dr. Chandra Sekhar Tiwary for all of the conversations and brainstorming sessions we have had together. I also appreciate Dr. Gustavo Brunetto, Dr. Sanjit Bhowmick, Marco Tulio Fonseca Rodrigues, Ana Paula Pereira Alves and Gonglan Ye for their contributions on my research projects. My colleagues and friends at Rice have also contributed much to the completion of my work. I would like to thank Amelia Heather-Sarah Church Hart, Sehmus Ozden, John Thomas Hamel and the rest of the MSNE students for all of our interactions.

Contents

List of Figures

List of Tables

List of Equations

Nomenclature

CNTs	Carbon Nanotubes
1D	One Dimensional
SWCNT	Single Wall Carbon Nanotube
DWCNTs	Double Wall Carbon Nanotubes
MWCNTs	Multi Wall Carbon Nanotubes
CVD	Chemical Vapor Deposition
YAG	Yttrium Aluminum Garnet
HiPCO	High-Pressure CO Conversion
WACVD	Water Assisted Chemical Vapor Deposition
HOPG	Highly Oriented Pyrolytic Graphite
2D	Two Dimensional
TCF	Transparent Conducting Film
ITO	Indium Tin Oxide
GO	Graphene Oxide
rGO	reduced Graphene Oxide
TMCs	Transition Metal Carbides
HER	Hydrogen Evolution Reaction
WC	Tungsten Carbide
3D	Three Dimensional
GAD	Glutaraldehyde
F-GO	Fluorinated GO

h-BN	hexagonal Boron Nitride
MD	Molecular Dynamics
SEM	Scanning Electron Microscopy
TEM	Transmission Electron Microscopy
IPA	IsoPropyl Alcohol
XRD	X-ray Diffraction
XPS	X-ray Photoelectron Spectroscopy
TGA	Thermo-Gravimetric Analysis
SSA	Specific Surface Area
BET	Brunauer, Emmet and Teller
CV	Cyclic Voltammetry
PDMS	Poly-DiMethylpolySiloxane
PPy	PolyPyrrole
LSV	Linear Sweep Voltammogram

Chapter 1

Introduction

1.1. Carbon Nanomaterials

1.1.1. Carbon Nanotubes

Carbon nanotubes (CNTs) are one of the most astonishing one dimensional (1D) carbon nanomaterials in the nanotechnology field. Carbon atoms form structures such as graphite, diamond and fullerenes (C_{60})[1,2] (Figure 1.1). CNTs have a hollow tube structure which consists only of carbon atoms[3]. Basically, CNTs form concentric circles of tube layers, where one single layer CNT is referred to as a single wall carbon nanotube (SWCNT), two layer CNTs are called double wall carbon nanotubes (DWCNTs), and more than two layer CNTs are known as multi wall carbon nanotubes (MWCNTs) (Figure 1.2). CNT's material properties vary according to their structural formation pattern--"chirality"--as well as its diameter, which determine if CNTs are either conductors or semiconductors[4]. The electronic

characteristics of CNT depend on its chiral vector, "C=(n,m)." Chirality patterns are classified in three shapes; zigzag, chiral and armchair (Figure 1.3)[5]. In the zigzag pattern, CNTs behave as a metal when "n" equals multiples of 3, and acts as a semiconductor when it does not. In the chiral pattern, CNTs behave as a metal when "2n+m" equals multiples of 3, and acts as a semiconductor when it does not. However, in the armchair pattern, CNTs only behave as a metal. Since CNTs can be used in many fields, such as for high stiffness and lightweight materials, CNTs can be utilized for mechanical[6-8], electrical[9-11] and chemical applications[12], and can also be used as gas detectors[13]. Moreover, CNTs can also be functionalized chemically for further applications[14]. Therefore, CNTs have a variety of applications for energy storage, water purification, automobiles, transportations, sports gears, electronics, and even in medical devices[15-17]. For example, "bicycles, tennis racquets, sail boats, antistatic parts for fuel filter lines, and packaging materials used in the electronics industries" are made by CNT-containing nanocomposites; as well as other kinds of products, such as semiconductors, that contain CNTs[18-20]. CNTs have the potential to be used in supercapacitors because of their large surface area which increases specific capacitance[21]. Usually CNTs are synthesized as a bundle that contains various species of chiralities with the number of species being "around 5-50 species from any preparation method"[22]. Although most applications--especially for semiconductors--require one specific chirality, the presence of a majority of a specific chirality is acceptable due to the difficulty in producing just one chirality[23].

Figure 1.1 – The schematic structures of graphite, diamond and fullerene[24].
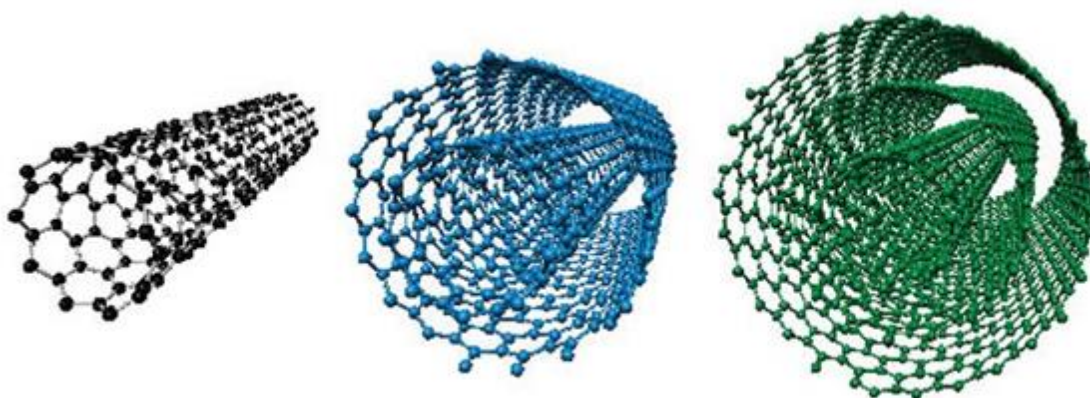
Figure 1.2 – SWCNT (left, black), DWCNTs (middle, blue) and MWCNTs (right, green)[25].
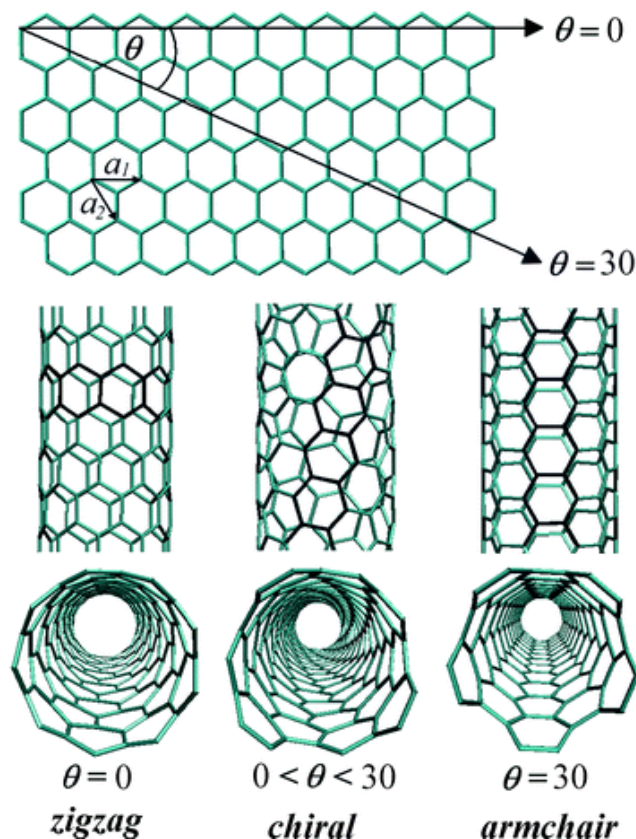
Figure 1.3 – CNT chirality patterns; zigzag, chiral and armchair[5].

After MWCNTs were examined and first reported in 1991[26] and SWCNTs in 1993[27], many researchers have studied the optimization of CNTs. As pristine CNTs are not soluble in most solvents, it was previously considered difficult to purify and refine CNTs based on its application usages. Since then, many kinds of CNT synthetic procedures and characterization methods have been developed. Publications and patents in regards to CNTs have been steeply increasing in number since 2000, due to the interesting and novel properties[28]. There are several ways to synthesize CNTs including: arc discharge[27,29], laser ablation[30], and chemical vapor deposition (CVD) methods[31-34]. Figure 1.4 shows one schematic example

of an ethanol CVD setup[34]. Although it was previously considered difficult to produce large volumes of CNTs, there are many synthetic methods to produce CNTs in bulk today. In CNT's embryonic stage, CNTs were compounded by one of two methods: arc discharge or laser ablation methods. The arc discharge method is the process of synthesizing MWCNTs around a negative carbon electrode. Arc discharge occurs between two carbon electrodes under argon or hydrogen atmospheres. SWCNTs can be synthesized around a vessel of the experimental setup when carbon electrodes involve some catalysts such as nickel or cobalt. Laser ablation is the method of synthesizing SWCNTs when YAG (Yttrium Aluminum Garnet) laser is irradiated to any carbon source with catalysts such as nickel or cobalt. The chirality of CNTs can be adjusted by changing the experimental conditions. However, it is hard to synthesize CNTs in bulk with these two aforementioned methods.

Many CVD procedures have been developed since the embryonic period of CNT development. These methods allow for CNTs' carbon precursor to come from many kinds of carbon sources such as ethylene and ethanol. In the CVD method, CNTs deposit or "grow" up on a substrate with the help of some metal catalysts when chemical bonds of carbon atoms are broken in inert atmospheres at the temperature of around 600-1,200°C[35]. There have been many efforts for optimizing CVD methods. High pressure carbon monoxide (CO) conversion (HiPCO) synthesis is one example of modified CVD ways to produce SWCNTs using high pressure carbon monoxide as a carbon source and iron pentacarbonyl ($Fe(CO)_5$) as a catalyst[36]. HiPCO has been proven to be able to produce approximately 1 nm diameter CNTs in high purity. The ethanol CVD method can produce vertically

aligned CNTs, using ethanol vapor as a carbon source[37,38]. Super growth synthesis can elongate CNTs to a height of 1 cm, injecting little amounts of water bubbles, known as water assisted chemical vapor deposition (WACVD) method[39]. The bubbled water acts to remove extra carbon atoms on the surface of the substrate which prevent further CNTs growth. The enhanced direct injection pyrolytic synthesis (eDips) method allows the synthesis of continuous SWCNTs by injecting catalyst particles into carbon gas sources[40]. Generally speaking, arc discharge and laser ablation methods can produce low defect and high purity CNTs but are not suitable for mass production, whereas CVD methods can synthesize large amount of CNTs at one time but the purity is relatively low[41].
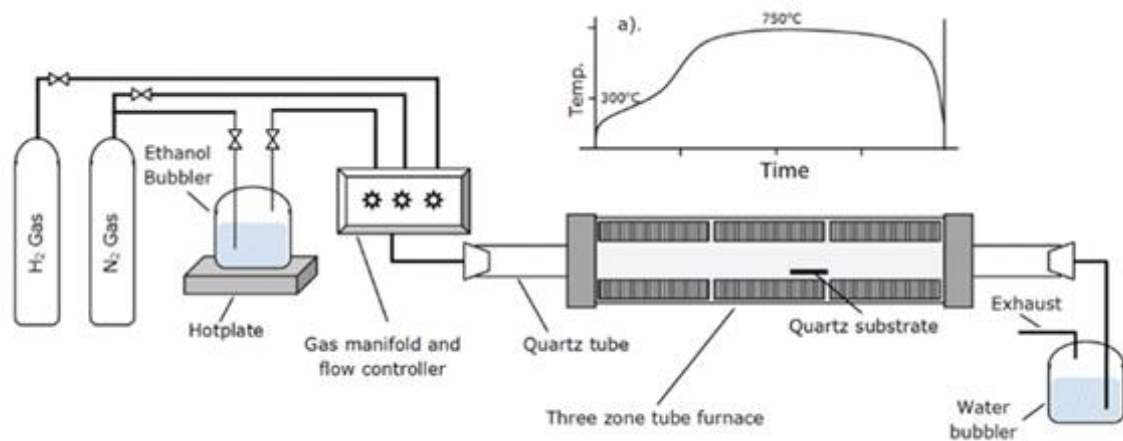
Figure 1.4 – One schematic example of a CVD apparatus[34]. Ethanol (a carbon source) is heated on a hotplate and the gas is injected with hydrogen and nitrogen gases. A quartz substrate is heated inside a furnace.

When using CNTs, especially for semiconductor applications, it is very important to choose a single chirality because semiconductors require very high purity to perform well. Utilizing CNTs in semiconductor applications has proven to be difficult due to the mixed chiralities during synthesis[42]. Although many scientists have tried to synthesize CNTs which have one particular chirality index, a technique for selecting chirality indices still remains a challenge[43,44]. There are some ways which were proposed by many researchers to obtain single chirality CNTs such as using a conditioning catalyst[45-48]. In 2014, Sanchez-Valencia et al. published an article regarding highly pure chirality selected armchair SWCNTs that were synthesized in high purity (6,6) using a precursor[49]. This method has two main steps: (1) a "suitably designed polycyclic hydrocarbon precursor" ($C_{96}H_{54}$) which forms a capped ultrashort (6,6) SWCNT seed through cyclodehydrogenation (CDH); (2) the nanotube starts growth from the seed by "epitaxial elongation" (EE) (Figure 1.5)[49]. Also in 2014, Yang et al. proposed a way to synthesize (12,6) SWCNTs using "tungsten based bimetallic alloy nanocrystals" as a catalyst, reaching 92% purity[50]. Figure 1.6 shows the process of specified (n,m) SWCNTs synthesis: (1) a molecular cluster--such as tungsten and cobalt alloy--forms a nanocrystal; (2) SWCNTs start to compound from the specified seed by an ethanol CVD method[50]. Other than these two ways, other unique methods have been suggested such as nanoring growth[51], cap formation[52], and open-end growth[53]. In 2014, Artyukhov et al. published a report about the mechanism of chiral growth of CNTs using computer simulations based on the idea of cutting a coffee cup[54]. Since they

proposed the system of CNT formation on this theoretical view, it might also be helpful to improve chirality selective methods.
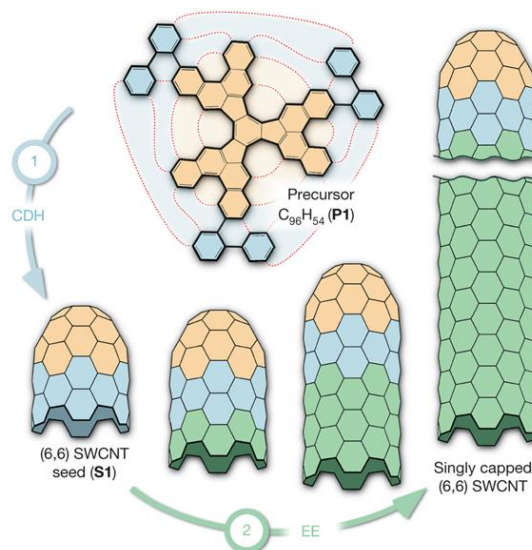
Figure 1.5 – The process of (6,6) SWCNT synthesis. (1) The precursor ($C_{96}H_{54}$) forms a capped ultrashort (6,6) SWCNT seed through CDH, (2) The CNT starts growth from the seed by EE[49].
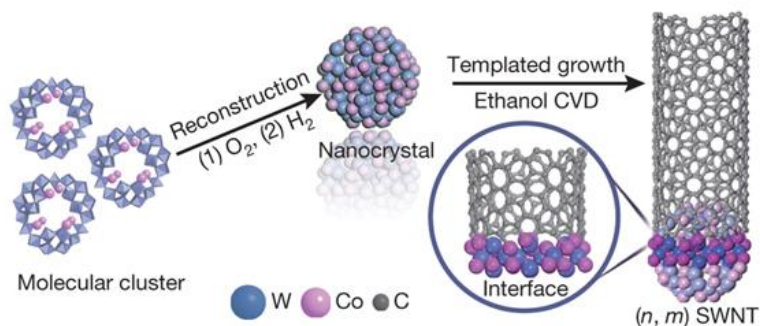
Figure 1.6 – The process of specified (n,m) SWCNT synthesis. (1) A molecular cluster forms a nanocrystal, (2) The CNT starts growth form the seed[50].

Because pristine CNTs are insoluble in most solvents[55], CNT solubility, if available, expands application ideas. Figure 1.7 shows a variety of CNT functionalization[14]. Adding carboxyl groups (-COOH) is a major way to reform CNT solubility[14]. Carboxyl groups can be added to CNTs by strong acids (such as nitric acid (HNO_3) and sulfuric acid (H_2SO_4)), ozone (O_3), and plasma reactions[56]. Moreover, there are also ways to incorporate hydroxyl groups (-OH) or methyl groups (-CH_3) as well[57]. CNTs consisting of carboxyl groups can be used as a gateway for other functional foams of CNTs, because many functionalization methods are based on CNTs with carboxyl group moities[14].
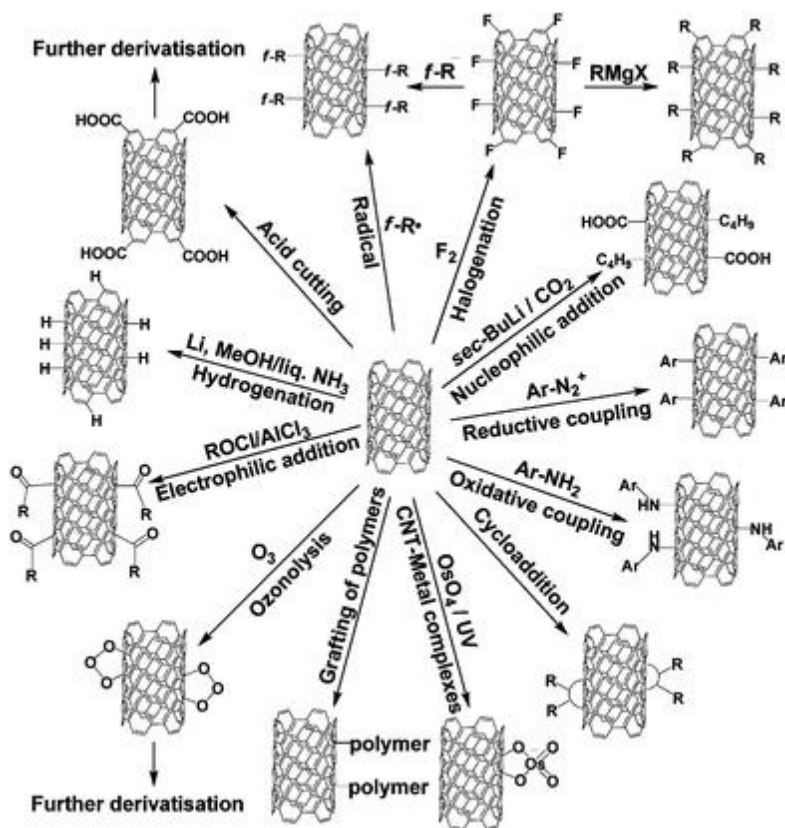
Figure 1.7 – A variety of CNT surface functionalization[14].

1.1.2. Graphene

Graphene is a nanomaterial which was discovered by Geim and Novoselov leading to their awarding of the Nobel Prize in 2010. They showed that they can peel off one single graphene sheet (Figure 1.8) from highly oriented pyrolytic graphite (HOPG) using adhesive tape[58]. Graphene is a completely two dimensional (2D) layer material (Figure 1.9) while graphite is consisted of stacked multilayer graphene sheets[59]. Graphene consists of hexagonal covalently combined carbon atoms like a honey comb structure which are sp^2 hybridized[60]. Graphene has superior material properties such as high stiffness, high electric and thermal conductivity[61,62]. A large number of scientists have engaged in the study of graphene as well as CNTs.
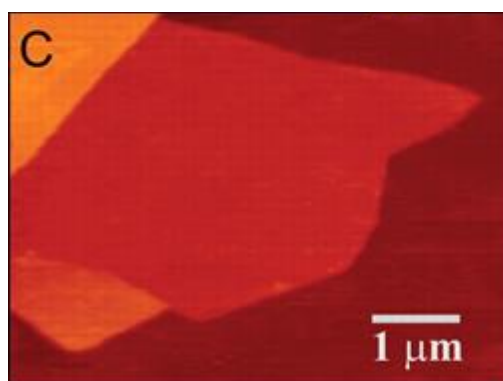
Figure 1.8 – Atomic force microscope image of single-layer graphene; "Colors: dark brown, SiO$_2$ surface; brown-red (central area), 0.8 nm height; yellow-brown (bottom left), 1.2 nm; orange (top left), 2.5 nm"[58].
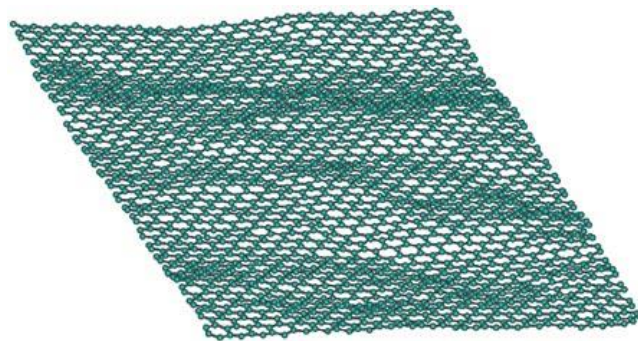
Figure 1.9 – An image of a graphene sheet[59].

Graphene sheets are hard to tear even when stretched by very strong forces[63]. Though it would be difficult to make, a single layer graphene "hammock"--the size of a newspaper (1 m^2)--would not break under the weight of an average sized cat (Figure 1.10)[64]. However, making large sizes of single layer graphene is still challenging[65]. Since graphene properties have been studied extensively this decade, it is still a relatively new field.
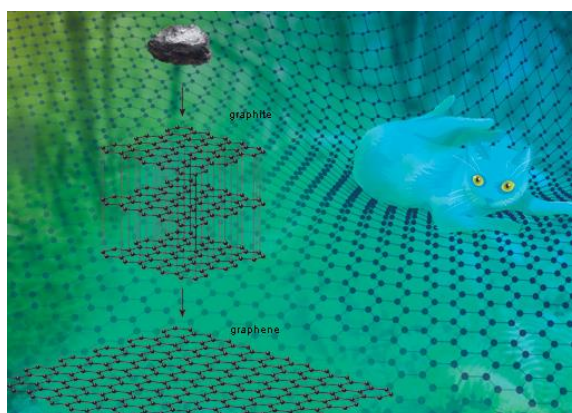
Figure 1.10 – A cat lies on graphene "hammock": the size of a newspaper (1 m^2) [64].

One of the most remarkable properties of graphene is its electrical performance[66,67]. Its electron mobility is more than 100 times greater compared to silicon, and it can be applied in a very quick response transistor and other large scale integrated circuits[68]. The electrons inside graphene can perform as not only "massless" Dirac fermions but also can exhibit the quantum Hall effect even at room temperature[69,70]. Since graphene is a very thin and highly conductive material, it can potentially be used as a transparent conducting film (TCF)[71]. In 2011, Zhu et al. developed a flexible TCF based on graphene--"metallic grid and graphene hybrid film"--which performs as a transparent electrode not only on a glass substrate but also even on a flexible polyethylene terephthalate film substrate (Figure 1.11)[72]. TCF has been used for sensor applications such as touch screens built into smart phones and tablets. Indium tin oxide (ITO) is currently the main material for touch screens primary because ITO is a clear and conductive material. Since ITO works well on glass, a touch screen made by ITO is typically vulnerable. In addition, the price of indium has increased due to the recent large demand for solar panels. In contrast, TCFs made by graphene can be flexible and hard to break.
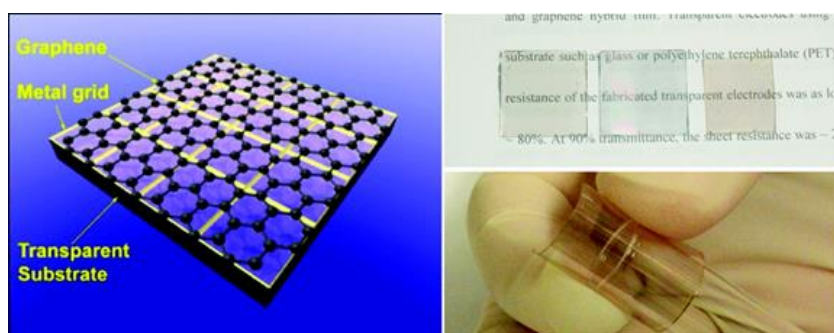
Figure 1.11 – Metal grid and graphene hybrid transparent electrode[72].

Currently, synthetic methods for the production of graphene have been proposed the as following: the HOPG, CVD methods[73-75] and reducing graphene oxide (GO) (Figure 1.12)[76]. CVD methods for graphene mainly use some metals as a catalyst such as copper or nickel, and a carbon source such as methane gas (CH_4)[77]. After Brodie synthesized GO in 1859, many synthetic methods have been developed so far[78]. In 1958, Hummers et al. proposed a synthetic route which uses potassium permanganate ($KMnO_4$), phosphoric acid (H_3PO_4) and sulfuric acid (H_2SO_4)[79]. GO is usually synthesized from graphite flakes providing many different types of synthetic methods (Figure 1.13)[79,80]. GO is a graphene sheet which contains hydroxyl, carboxyl, and epoxy groups[81,82]. GO has limited solubility in water due to such functional groups unlike graphene[83]. When GO is reduced, its material structure would become close to graphene but it is difficult to reduce GO completely to obtain pure graphene[84]. In 2015, Li et al. synthesized graphene on a flexible commercial polyimide film using a CO_2 laser cutter system, and the sample can be applicable for supercapacitors[85]. This technique enabled scientists to obtain graphene films at room temperature and in atmospheric conditions, which does not require a CVD technique, high temperature or an inert atmosphere.
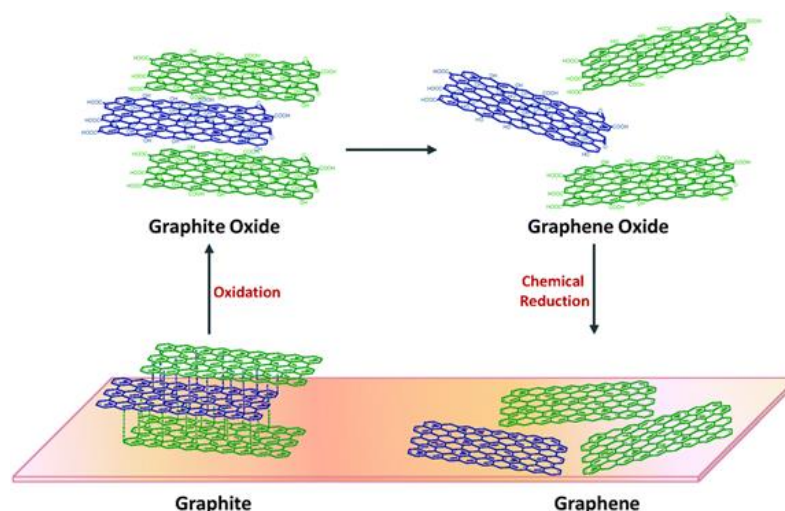
Figure 1.12 – A flow of graphene synthesis. 1) Graphite is oxidese to Graphite Oxide, 2) Graphite Oxide becomes GO, 3) GO is reduced to Graphene[76].
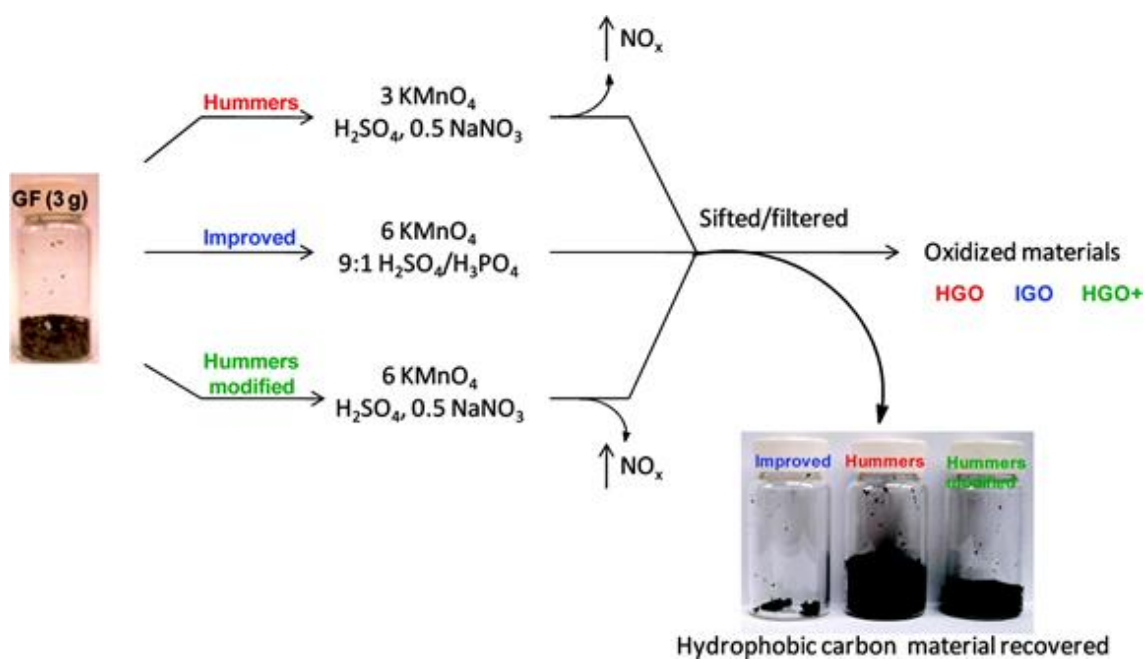
Figure 1.13 – Comparison of three synthetic methods of GO production based upon the Hummer's method[80].

Reduced graphene oxide (rGO) is one of the most popular graphene materials for the application of supercapacitors[86-89]. Therefore, rGO is considered to be suitable for supercapacitors because of its large surface area, since this respective property is an important parameter for high capacitance. GO is not conductive due to sp^3 hybridization, whereas rGO is conductive because "rGO has a wide range of conductivity depending on the oxidation state"[90]. In 2011, Gao et al. demonstrated rGO as "a new type of separator/electrolyte membrane system" (Figure 1.14)[91]. They used laser irradiation to reduce and pattern GO films, and synthesized micro-supercapacitors[91].
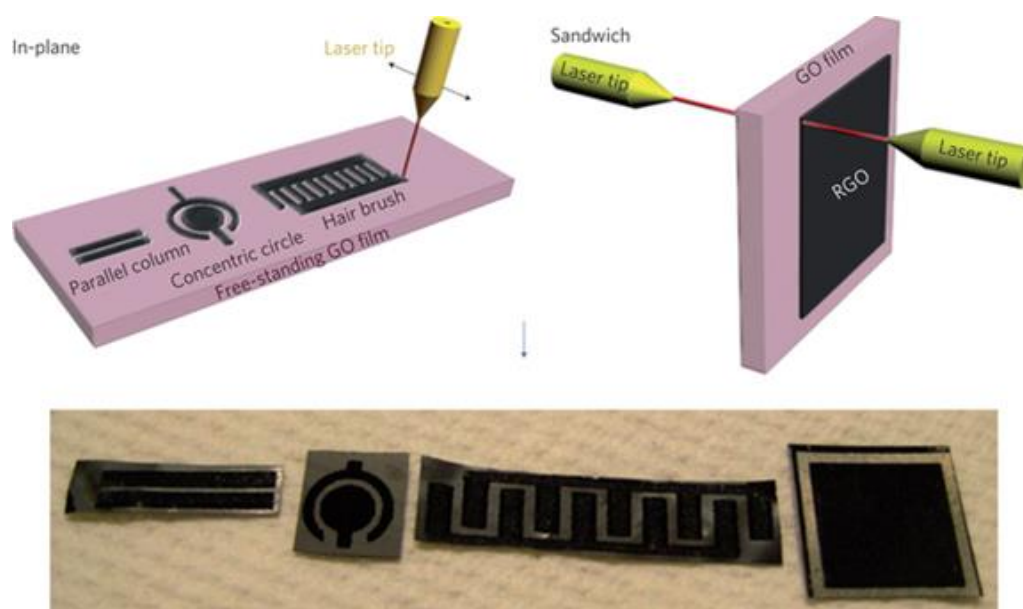
Figure 1.14 – The schematic images of micro-supercapacitor synthesis by a CO$_2$ laser patterning[91].

1.2. Transition Metal Carbides

1.2.1. Molybdenum Carbide

According to recent research, transition metal carbides (TMCs) have great potential as catalysts for hydrogen evolution reactions (HERs) activity as well as materials for battery electrodes[92-97]. Rare earth metals--such as platinum--have been used for HER catalysts so far, but these metals are very expensive and securing stable supplies is difficult[98,99]. Substitutes for these scarce materials have been desired for a long time, and many candidate materials have been developed[100,101]. The examples of these candidates are TMCs, which have melting points over $1,000°C$[102]. One TMC that is a great HER catalyst is molybdenum carbide (Mo_2C), which has a melting point of $2,705°C$[103]. Although molybdenum disulfide (MoS_2) has also been examined high activity for a catalyst of HER activity[99,101,104], molybdenum carbide is more advantageous due to the fact that it is sulfur free. Tuomi et al. also mentioned the fact that the catalytic activity of molybdenum carbide depends on its "surface orientation" while molybdenum disulfide's catalyst activity is "limited by the number of edge sites"[103,105,106]. Molybdenum carbide's usages as potential battery electrodes are due to "its high reversible capacity"[107]; therefore, molybdenum carbide is a next generation versatile material which can help solve future expensive and scarce platinum crisis.

Although molybdenum carbide was believed to have a hexagonal structure, Parthe et al. discovered it has an orthorhombic structure via a neutron diffraction

study in 1962[108]. After that, however, some phase diagrams were proposed and in 1988 Dubois et al. summarized that molybdenum carbide can have different structures depending on temperature[109]. After a thorough investigating, Dubois et al. summarized molybdenum carbide can have an ordered orthorhombic ζ-Fe_2N structure (α-Mo_2C) under 1,400°C (Figure 1.15) and a disordered hexagonal L'3 structure (β-Mo_2C) over 1,400°C[109,110].
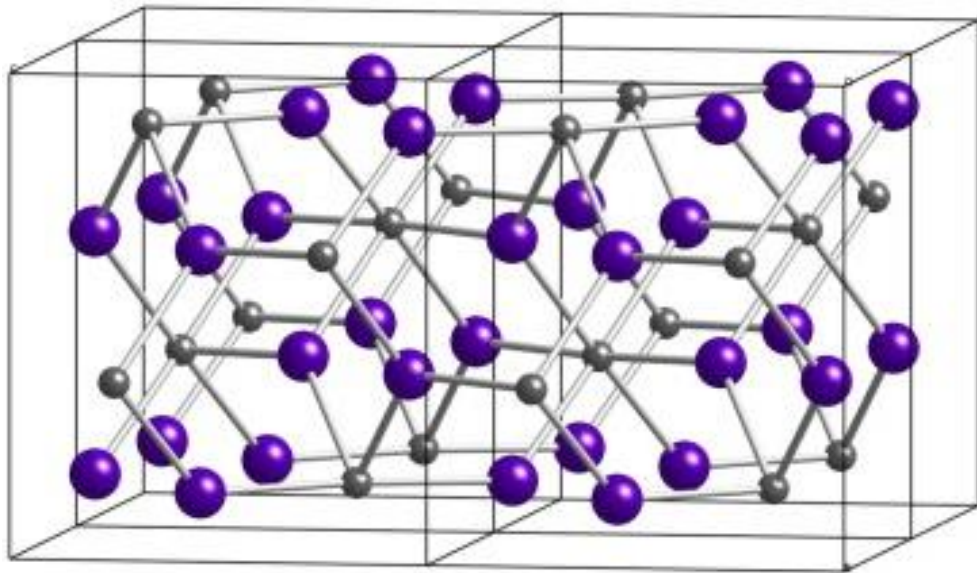
Figure 1.15 – The schematic figure of orthorhombic structure of α-Mo_2C[110].

1.2.2. Tungsten Carbide

Tungsten carbide (WC), which a simple hexagonal structure (Figure 1.16) and a melting point of 2,776°C, is another example of a viable TMC for a catalyst of HER activity[93,94,102,110]. Tungsten carbide has a very high stiffness, and is a very strong material; therefore, tungsten carbide is able to be applied to cemented carbide which is mixed with metals such as iron, cobalt or nickel. Hard materials made with tungsten carbide are currently used as a cutting tool for industrial machinery[111].
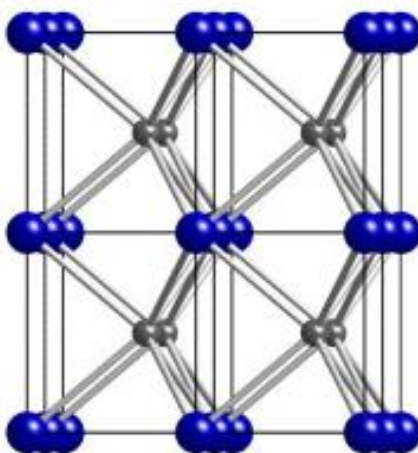
Figure 1.16 – The schematic figure of hexagonal structure of WC[110].

1.3. Three Dimensional Nanostructures

1.3.1. Overview

Building three dimensional (3D) structures using nanomaterials--such as CNTs--have been attempted, but it has proven difficult to control the properties of the 3D structures[112-116]. There are many kinds of carbon-based 3D structures, whose architectures have great potential in the applications of mechanical dampers, oil absorption materials, field emitters and supercapacitors[117-120]. Ozden et al. focused on applying CNTs to 3D scaffold structures[121,122]; they showed the 3D CNT scaffold structures are mechanically superior to 2D GO.

1.3.2. Nanoscale Porous Structures by Freeze-drying Methods

Freeze-drying procedures are one of the synthetic methods of controlling 3D structures[123]. The architectures made by an assistance of a lyophilization process can form scaffold structures because the water within in the material sublimates giving the scaffolds favorable mechanical and thermal stabilities[124]. In 2013, Sudeep et al. published work using GO 3D solid scaffold structures in the application of gas storage[125]. A synthetic method was proposed to create GO 3D solid scaffold structures interconnected by chemical linkages, showing the prototype of 3D "poly-GO" (Figure 1.17)[125]. Although some ideas of GO structures have been suggested so far, few of them depend on chemical covalent bonding[126,127]. These previously suggested structures are typically weak compared with covalent bonding whereas the covalent linkage can achieve "superior properties to such structures"

because of the chemical properties of covalent bonding if the structures can be formed by covalent bonding[125]. To mitigate this weakness, chemically cross-linked "poly-GO" was synthesized (Figure 1.17)[125]. Because GO contains many hydroxyl groups at the edges, "glutaraldehyde (GAD; $CH_2(CH_2CHO)_2$) contains two aldehyde groups that can interact with -OH to form hemiacetal structures"[125]. Therefore, GO can be functionalized with GAD in a short time period at room temperature, and the functionalized GO forms interconnected GO-sheet networks[125]. The water in the initial GO/GAD mixture joins the GO into networks allowing the freeze-drying process to cement the GO together into 3D poly-GO[125]. Through the freeze-drying process, the water is gone, and leaves "various simple cavities" inside poly-GO[125]. The authors also synthesized fluorinated GO (F-GO) following the same procedure[125]. In order to enforce the mechanical stability, resorcinol ($C_6H_4(OH)_2$) was added with GAD to form "amorphous gelation"[125].

In 2014, Vinod et al. improved upon the previous 3D structures by using not only GO but also conformal hexagonal boron nitride (h-BN) platelets so as to reinforce the layers[128]. The structure of h-BN is similar to graphene because boron atoms and nitrogen atoms consist of hexagonal structures alternately. Basically, h-BN is a carbon-like material, often referred to as "white graphite"[129], whereas it is not conductive but chemically and thermally stable[130,131]. Generally, h-BN is inert, and it is insoluble even in strong acid or base solutions[132]. Because of its splendid material properties, h-BN is also used in some high temperature solid lubricants, which require stability at high temperatures (up to 1,000℃ in air, up to 1,400℃ under vacuum, and up to 2,800℃ in inert

atmosphere)[129]. Vinod et al. reported that the "mechanical and thermal stability" of the 3D structure of GO was improved by containing h-BN[128]. They focused on the previous studies where the structure formed by h-BN with graphene led to very interesting optical, electronic, thermal properties as well as mechanical strength[128,133,134]. They also paid attention to the fact that "h-BN is the most structurally compatible form and is an isomorph of graphene;" therefore, the hybrid structure of h-BN and GO is "a good lattice matching"[128,135,136]. The authors showed the hybrid scaffold structure is a "fairly uniform distribution of h-BN platelets throughout the foam"[128]. The layers of the structures also seem to be stacked orderly and the porous morphology joined perpendicular to "the larger layer" (Figure 1.18)[128]. Vinod et al. measured the mechanical properties of the structure which were controlled strain experiments and load experiments (Figure 1.19)[128]. For controlled strain tests, Figure 1.19a shows the results of GO without h-BN (GO-0.0BN), and Figure 1.19b shows the results of GO with 0.5% h-BN (GO-0.5BN)[128]. Although GO-0.5BN performed "an increase in stiffness as time increases" for each loading, GO-0.0BN dropped the stiffness at higher strain "due to its deformation"[128]. For loading experiments, Figure 1.19c shows loading cycles, Figure 1.19d shows the results of GO-0.0BN, and Figure 1.19e shows the results of GO-0.5BN[128]. For GO-0.0BN, the maximum stiffness ended shortly, and it was broken into "a clean fracture in foam"[128]. For GO-0.5BN, it remained the foam[128]. Figure 1.19f shows the result of the test using Instron at a strain rate of 10^{-3} s^{-1}[128]. Although the samples increased in stress till 30-35%, they started to

compact on further load[128]. The authors also calculated the mechanical performance using molecular dynamics (MD) simulation[128].
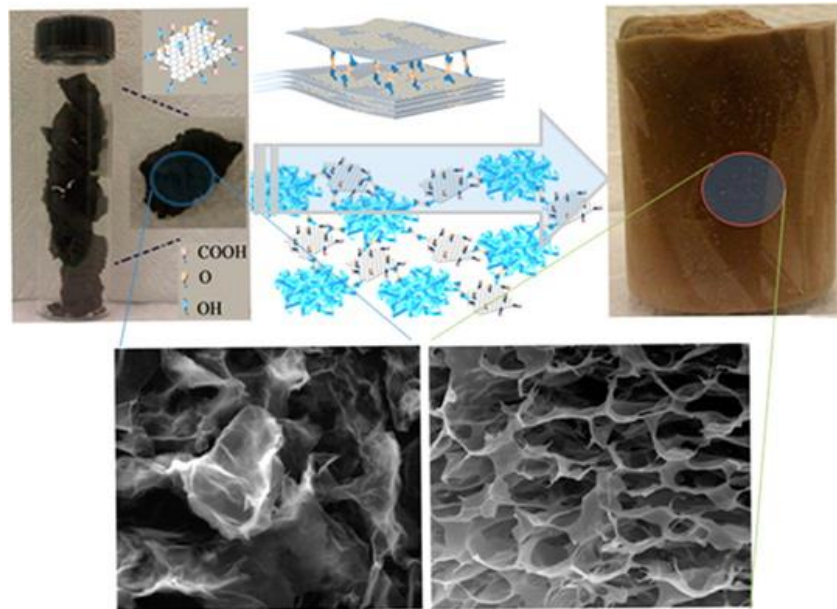
Figure 1.17 – Chemically interconnected 3D GO foam[125].
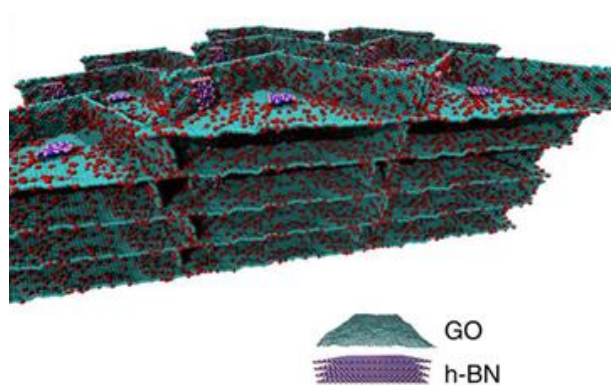
Figure 1.18 – "Proposed schematic for GO-0.5BN foam based on SEM observations"[128].
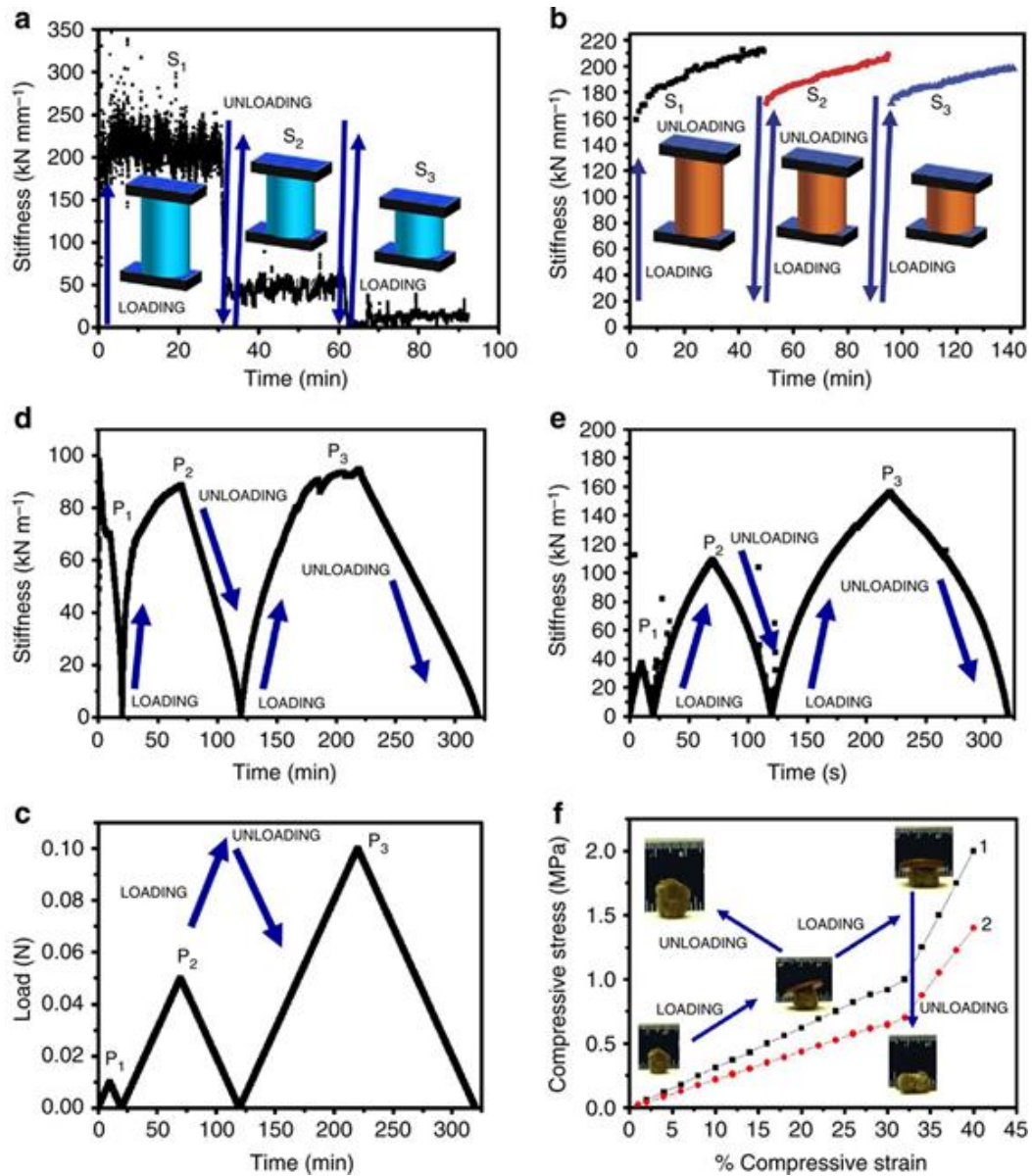
Figure 1.19 – Mechanical test results of h-BN containing GO foam. a) Controlled strain experiment by GO-0.0BN, b) Controlled strain experiment by GO-0.5BN with strains; S$_1$:0.5%, S$_2$:1%, S$_3$:2%, c) The load-unload cycles for (d,e), d) Controlled load experiment by GO-0.0BN, e) Controlled load experiment by GO-0.5BN, f) Compression test results[128].

1.3.3. Hybrid Materials by CNTs and 2D Materials

Hybrid materials consisting of 2D materials--such as graphene and graphene like materials--and CNTs have very good electrical properties because graphene and CNTs have not only extreme material properties but also their large specific surface areas play major roles in their energy densities[137-139]. There are many reports regarding CNTs and graphene hybrid materials (Figure 1.20) (especially focusing on supercapacitors) and these kinds of hybrid structures are combined with each other by either physical or chemical interactions[140,141]. Typically, physically interacted hybrid materials are made by mixing CNTs and 2D materials like a "sandwich" (Figure 1.21)[142,143], whereas the chemical ones are synthesized seamlessly by bottom-up CNT growth on 2D materials' surfaces (Figure 1.22)[144-146]. Du et al. showed "3D Pillared Carbon Nanotube–Graphene Networks" originated from HOPG by tuning CNT growth[147]. As rGO is a better material for supercapacitors among graphene based materials, there are many reports regarding physical mixtures of CNTs and rGO[148-150]. Although CNTs and rGO are an "effective combination"[104], there are few reports regarding a covalent bonding of the both hybrid structures.

The combination of CNTs and h-BN also plays a significant role for hydrogen storage and high-performance field emission devices, since h-BN has a wide band gap (around 5.9 eV)[151-154]. Yang et al. mentioned CNTs coated with h-BN can enhance its field emission because h-BN coating plays a role in decreasing "the height of the surface potential barrier of the emitter"[151]. On the other hand,

Muthu et al. concluded that the presence of h-BN nanoparticles helped to increase the hydrogen storage capacity[152].
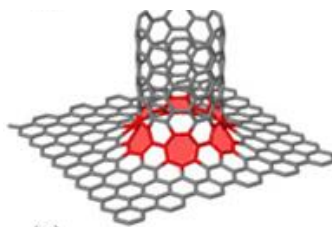
Figure 1.20 – Schematic of CNT and graphene hybrid material[155].
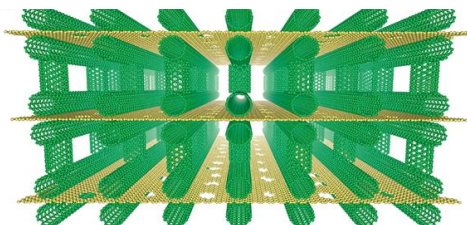
Figure 1.21 – One example of physically mixed 3D CNTs and graphene hybrid material[143].
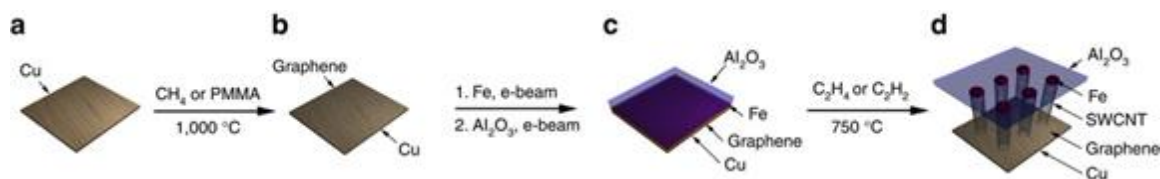
Figure 1.22 – Schematic procedure of CNTs on graphene hybrid material. Graphene is formed on copper, and iron and alumina are deposited on the surface. Allinged SWCNTs are synthesized on the surface[144].

1.4. Organization of Thesis

This thesis includes an introduction regarding carbon nanomaterials, TMCs, and 3D nanostructures briefly, and then discusses about novel 3D nanomaterials and nanostructures such as sphere shaped 3D CNT porous and scaffold structures, hybrid structures of CNTs and 2D materials, and unique flake structures of molybdenum carbide. Each experimented section mentions the motivation, experimental procedures, characterization methods, result, and conclusions. At last, this thesis concludes each project and mentions their future outlooks.

Chapter 2

Scalable Freeze-dried Carbon Nanotubes Based on Spherical Structures

2.1. Overview and Motivation

Though many scientists have attempted to build 3D structures from nanomaterials, such as CNTs, it is still difficult to control the properties of these structures[112-116]. 3D carbon-based architectures have great applications for mechanical dampers, oil absorption materials, field emitters and supercapacitors because of their structures and properties; therefore, precise control of the synthesis of these 3D structures is necessary for optimal performance in these applications[117-120].

Freeze-drying is one way to efficiently control the synthesis of nano/micro-3D structures by enabling atomic interconnections inside the materials[123]. 3D

nano architectures synthesized by a lyophilization process usually form scaffold structures because the water included inside of the materials is sublimated[124]. The material is made up of seamlessly interconnected individual layers, creating a porous structure[125,128]. As the number of layers created within the material increase, the surface area increases. This enables the 3D porous structures to have strong mechanical properties as well as being easily scalable[128].

This chapter discusses the synthesis of sphere-shaped 3D structures using carboxyl group-functionalized CNTs. The important things are not only controlling the structure but also enabling mass production in order for future applications. The spheres have a scaffold structure interconnected by functionalized CNTs containing carboxyl groups (-COOH). The interconnection is formed by GAD and resorcinol to create the structures. When the spheres were made, the mixed solution was pipetted dropwise into liquid nitrogen and the solution started to form a sphere shape. Since the diameter of the CNT spheres is tiny, it is able to immediately freeze when immersed in the liquid nitrogen. This method can easily be scaled up because the solution for the CNT spheres can be pipetted continuously. The diameter of the CNT spheres is also variable by changing pipet or needle size, or spray pressure. The structures of the CNT spheres were examined by electron microscopies and their images show the samples have 3D porous structures even inside the structures. Furthermore, in order to examine the interaction of 3D CNT structures, detailed MD simulations were performed which demonstrated the mechanism of combining functionalized CNTs, as well as explained how the CNT functional groups interact with each other.

2.2. Synthesis of the CNT Spheres

2.2.1. CNT Functionalization

The functionalized CNTs used in the spheres are commercial MWCNTs (Table 2.1) with carboxyl groups (-COOH) attached to the side walls. The CNTs were functionalized with nitric acid (HNO_3) in an oil bath (70~80°C) for approximately 5 days, which yielded carboxyl groups[157-159]. Figure 2.1 shows the Fourier Transform Infrared Spectroscopy (FTIR) patterns of the MWCNT powder (The lower blue line is before functionalization and the upper red line is after functionalization). Figure 2.1b shows the magnification of Figure 2.1a between 3,200 and 3,500 cm^{-1}. The FTIR patterns were measured by using Thermo Fisher Scientific Model: Nicolet iS50. The FTIR peaks for after the functionalization are: the C=O stretch peak at 1785 cm^{-1} (Figure 2.1a) and the O-H peak around 3,230-3,430 cm^{-1} (Figure 2.1b)[160,161].

Manufacturer	Cheap Tubes Inc., Cambridgeport, VT
Outer Diameter	20-30 nm
Length	10-30 μm
Purity	more than 95 weight %
Ash	less than 1.5 weight %

Table 2.1 – The description of the commercial MWCNTs (Cheap Tubes Inc.)[162].
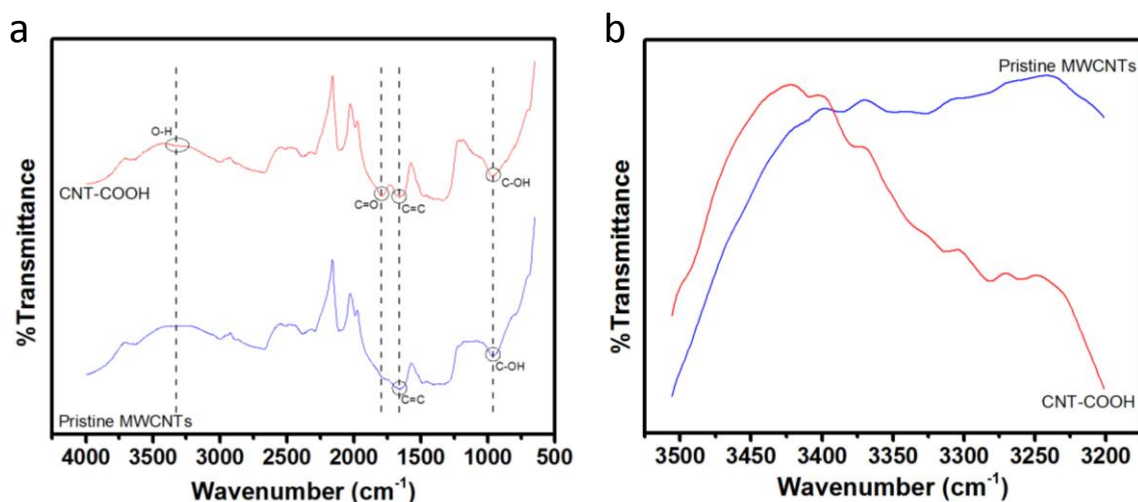
Figure 2.1 – a) FTIR patterns of MWCNT powder. After the functionalization, there are the C=O stretch peak at 1,785 cm^{-1} and the O-H peak around 3,230-3,430 cm^{-1} showed up. b) The magnification of (a) between 3,200 and 3,500 cm^{-1}. The O-H peak broaden around 3,230-3,430 cm^{-1} for the functionalized CNTs' pattern (CNT-COOH).

2.2.2. Formation of Sphere Structures

Functionalized CNTs were dispersed in deionized (DI) water (10 mg CNTs/1 mL DI water), and the CNT solution was sonicated for 1 hour. After sonication, GAD (7 μL/1 mL, Sigma-Aldrich, G6257, Grade II, 25% in H$_2$O), resorcinol (1.2 mg/1 mL, Sigma-Aldrich, 398047, ACS reagent, ≥99.0%) and borax (tiny amount as a catalyst) were added to the CNT solution, then the mixed solution was sonicated further 3~4 hours. This solution was dropped directly into liquid nitrogen using a pipet or a needle with syringe. Every single droplet started a nucleation process resulting in a

sphere shape (Figure 2.2). The diameter of the CNT spheres can be varied by changing the tip size of a pipet or needle. Figure 2.3 shows the optical images of the CNT spheres where the sizes varies from 20 μm (Figure 2.3A) to 3.5 mm (Figure 2.3B). Though it is easy to accumulate a large number of spheres, the limiting factor is the space inside the container of liqud nitrogen; if the spheres touch as they are dropped in, they adhere to each other connecting two spheres together. Once the freezing process was complete when immersed in liquid nitrogen, the spheres were able to touch and not attach to each other. To ensure they are totally frozen, the spheres were allowed to stay immersed in the liquid nitrogen for a few minutes, then the samples were moved into small vials for the lyophilization process. The freeze-drying machine (Millrock Technology freeze drier) was maintained at approximately -50℃ and 40 mtorr for around 4 days. During the freeze-drying process, the water inside the CNT spheres was sublimated and the scaffold structures were formed. Since the density of water's ice phase is greater than liquid phase, the spheres shrink slightly after the lyophilization process because the inside water has gone. The scaffold structures were shaped when the solution was dropped into the liquid nitrogen; therefore, the CNT spheres can retain these structures even after the water has gone. When the CNT spheres were dropped into liquid nitrogen by using 3 mL pipet, the average diameter was 3.36 mm, the average weight was 0.50 mg and the average density of the CNT spheres was calculated as approximately 3.1 kg/m^3.
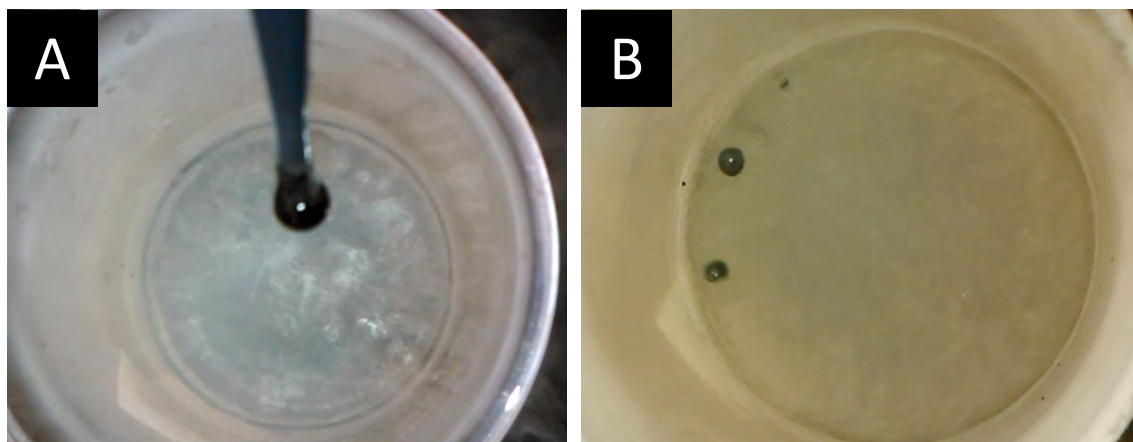
Figure 2.2 – The pictures of the formation of CNT spheres in liquid nitrogen. A) The solution of CNT spheres on the tip of a pipet. B) CNT sphere samples in liquid nitrogen.
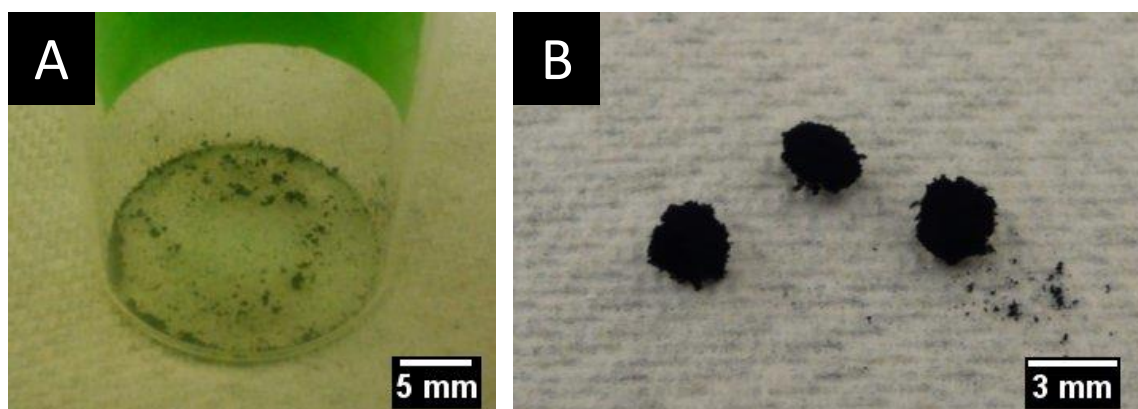
Figure 2.3 – A) The optical image of CNT sphere samples whose diamter is around 20-100 μm. These samples were dropped by a needle. B) The optical image of CNT sphere samples whose diameter is about 3 mm. These samples were dropped by a 3 mL pipet.

2.3. Results and Discussion

2.3.1. Characterization by Electron Microscopy

The characterization by electron microscopies were carried out by FEI Quanta 400 scanning electron microscopy (SEM) at accelerating voltage of 15-20 kV and JEOL 2100 field emission gun transmission electron microscopy (TEM) at operating at 200 kV. Figure 2.4 and Figure 2.5A-D show SEM images of functionalized CNTs connected with other CNTs to form interconnected porous 3D scaffold structures. Figure 2.4 shows SEM images of a 3 mm diameter CNT sphere; Figure 2.4A shows a bird's eye view of the isotropic sphere; Figure 2.4B,C show magnified images of the sphere's top, indicating a porous structure and interconnected CNTs; Figure 2.4D-F show the sphere's inside, further indicating an inner porous structure and interconnected CNTs. Figure 2.5A shows SEM images of a 100 μm diameter CNT sphere. Figure 2.5B-D show the magnification of the sphere's inside. The CNT spheres also maintained the porous structures even with the smaller diameter. Figure 2.5E,F show TEM images of the CNT sphere. Although the sample was dispersed in isopropyl alcohol (IPA) and sonicated about 10 minutes so as to make a TEM sample, the TEM images show each CNT connects with other CNTs and still forms an interconnected structure.
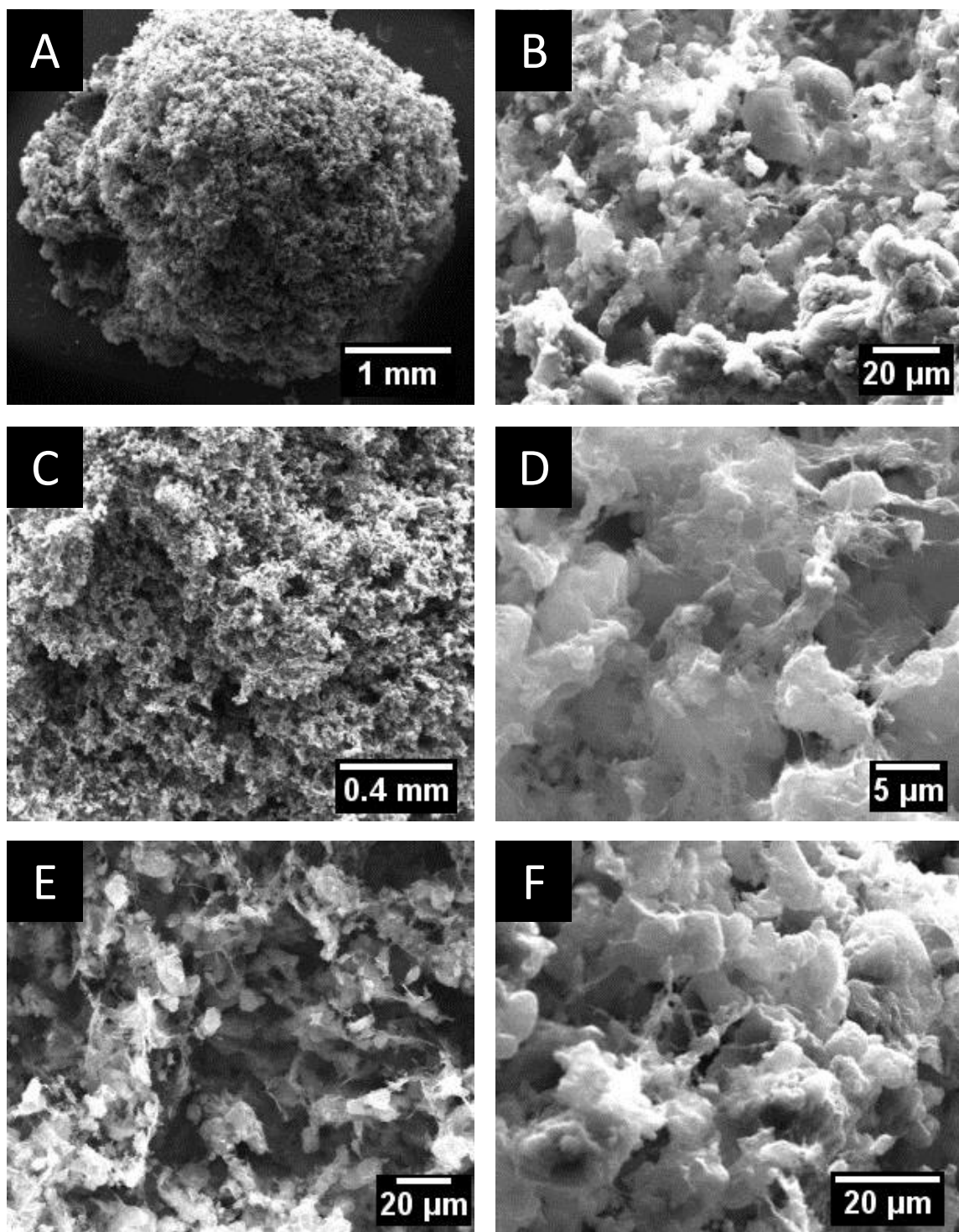
Figure 2.4 –SEM images of a 3 mm diameter CNT sphere.
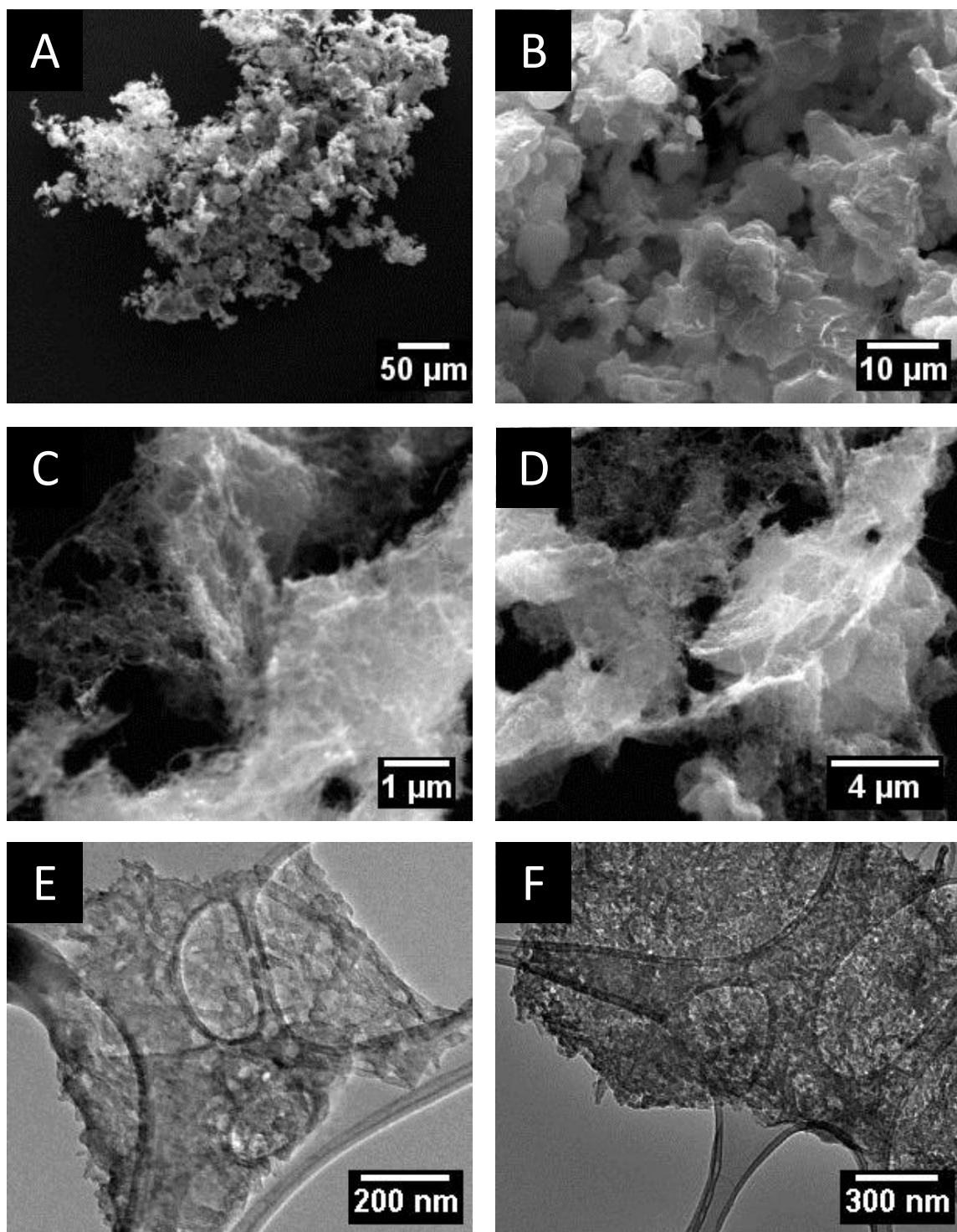
Figure 2.5 – The SEM and TEM images of a CNT sphere. A-D) SEM images of an

100 μm diameter CNT sphere. E,F) TEM images of a CNT sphere.

2.3.2. Characterization by Raman Microscopy

Raman spectroscopy of the samples was carried out by RENISHAW inVia Raman Microscopy using a 514 nm laser. Figure 2.6 shows the comparison of the Raman spectrum of a CNT sphere: functionalized CNTs (CNT-COOH) and pristine MWCNTs. CNTs have mainly two major peaks on Raman spectra, which are D band and G band[163]. The D band shows disorder of CNTs, and the G band shows graphitic layer[163]. The spectrum of the CNT sphere shows typical CNT peaks: D band at 1,342 cm^{-1}, G band at 1,577 cm^{-1}, 2D band at 2,691 cm^{-1} and 2G band at 2,935 cm^{-1}[163]. The spectrum of functionalized CNTs (CNT-COOH) also shows typical CNT peaks: D band at 1,343 cm^{-1}, G band at 1,570 cm^{-1}, 2D band at 2,677 cm^{-1} and 2G band at 2,917 cm^{-1}[163]. Similarly, the spectrum of pristine MWCNTs shows typical CNT peaks: D band at 1,346 cm^{-1}, G band at 1,572 cm^{-1}, 2D band at 2,703 cm^{-1} and 2G band at 2,921 cm^{-1}[163]. The peak positions of each spectrum have almost the same values after the functionalization and synthesizing the CNT spheres; therefore, the Raman spectra show the CNTs have retained their structure throughout their initial pristine state to the sphere state.

The Raman spectra also provide information that not only the CNT spheres contain CNT itself but also the density of defects between the D band and G band (I_D/I_G) is less than one (approximately 0.81 for a CNT sphere). For functionalized CNTs (CNT-COOH), the value of I_D/I_G is approximately 0.86. For pristine MWCNTs, the value of I_D/I_G is approximately 0.68. Since all of the three values of the density of defects are below one, there are fewer defects and imperfection on the CNTs even at

the sphere structure comparing with the CNTs which have greater D band peak than
G band's.
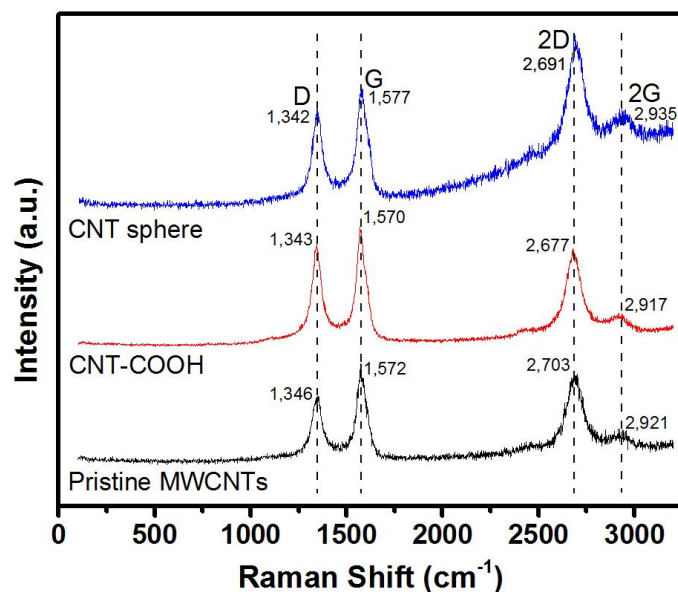
**Figure 2.6 – Raman spectra of a CNT sphere, functionalized CNTs (CNT-COOH)
and pristine MWCNTs. There are clear peaks of D band, G band and 2D band
for each epsctrum, and the positions of the peaks do not move throughout
pristine states to sphere states. All of the values of I_D/I_G are below one.**

2.3.3. Characterization by X-Ray Diffraction

X-ray diffraction (XRD) pattern was measured by Rigaku D/Max Ultima II
Powder XRD using a CuKα x-ray tube. Figure 2.7 shows the XRD pattern of a CNT
sphere and it reveals typical CNT peaks which are C(002) at 25.9° and C(100) at

43.4°[164]. Similarly to the Raman spectra, this XRD pattern also confirms the existence of CNTs in the sphere.
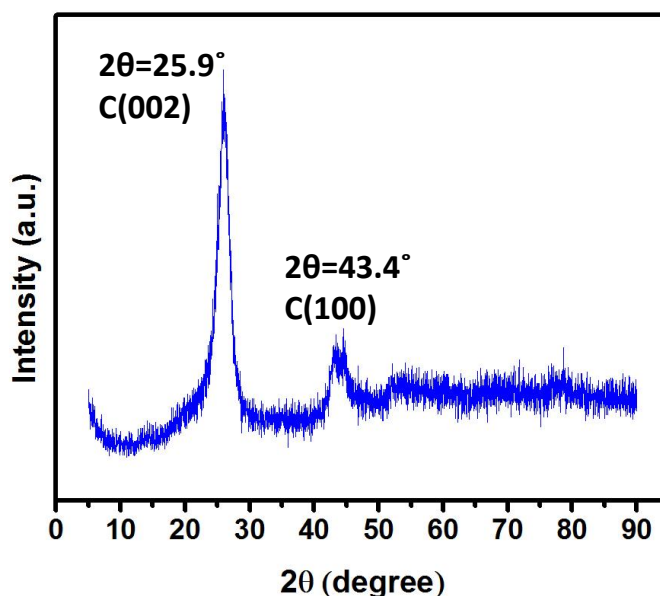
Figure 2.7 – XRD pattern of a CNT sphere. There are two major CNT peaks which are C(002) at 25.9° and C(100) at 43.4°.

2.3.4. Characterization by X-Ray Photoelectron Spectroscopy

X-ray photoelectron spectroscopy (XPS) pattern was examined by PHI Quantera XPS using an AlKα x-ray tube. Figure 2.8 is the XPS pattern of pristine MWCNTs; Figure 2.9 is XPS pattern of functionalized CNTs (CNT-COOH); Figure 2.10 is XPS pattern of a CNT sphere. Each figure has the fitting of the C1s peak as the insets. The inset of Figure 2.8 shows C-C bonding at 284.6 eV, C-O bonding at 286.5 eV, C=O bonding at 289.3 eV, and O-C=O bonding at 291.2 eV[165]. The inset of

Figure 2.9 shows C-C bonding at 284.4 eV, C-O bonding at 286.7 eV, C=O bonding at 288.9 eV, and O-C=O bonding at 291.0 eV[165]. The inset of Figure 2.10 shows C-C bonding at 284.5 eV, C-O bonding at 286.9 eV, C=O bonding at 289.2 eV, and O-C=O bonding at 291.3 eV[165]. Each position of binding energy is almost the same among the three. The intensity of the O1s peaks increased comparing the XPS patterns of MWCNTs and functionalized CNTs, and of functionalized CNTs and CNT spheres. Since the ingredients of CNT spheres are functionalized CNTs, GAD, and resorcinol, the peaks should mainly show carbon and oxygen. These results help to show CNT spheres have carboxyl groups and hydroxyl groups, and also that these functional groups retain their bonding even after the freeze-drying process.
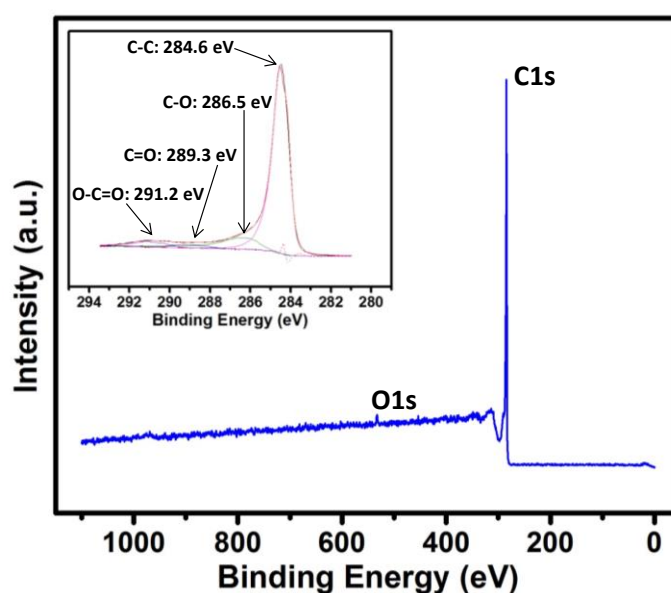
Figure 2.8 – XPS pattern of pristine MWCNTs. The C1s peak has C-C, C-O, C=O and O-C=O peaks (inset).
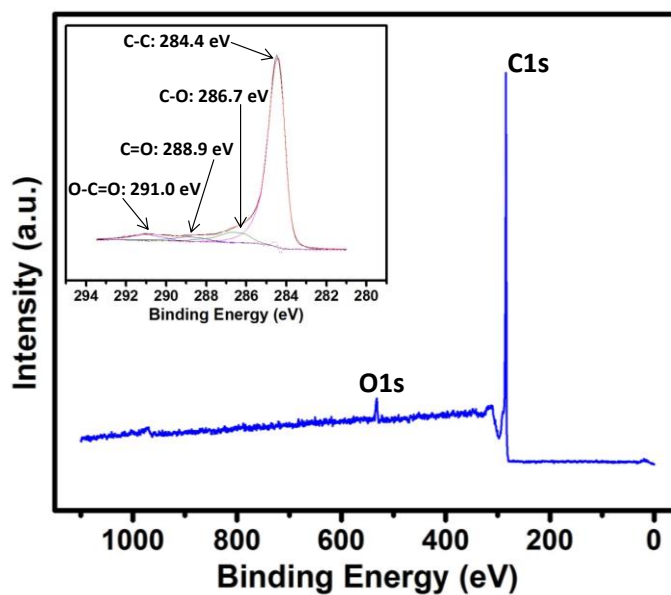
Figure 2.9 – XPS pattern of functionalized CNTs. The C1s peak has C-C, C-O, C=O and O-C=O peaks (inset).
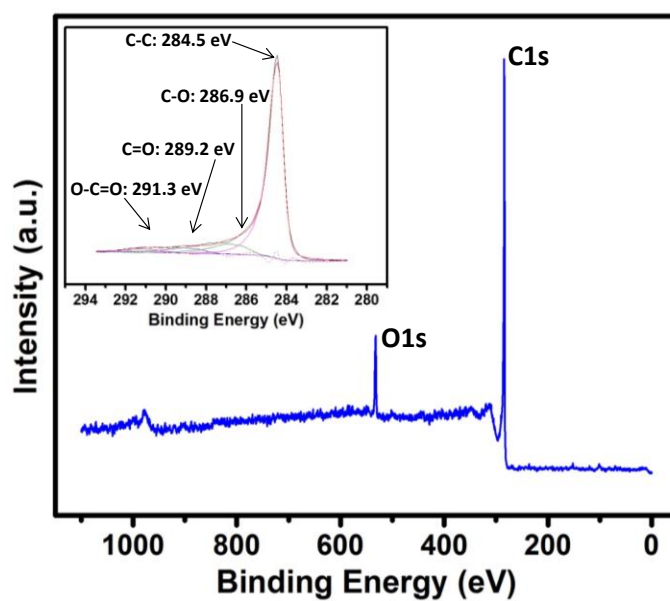
Figure 2.10 – XPS pattern of a CNT sphere. The C1s peak has C-C, C-O, C=O and O-C=O peaks (inset).

2.3.5. Characterization by Thermo-Gravimetric Analysis

Thermo-gravimetric analysis (TGA) was carried out by TA Instruments' Q-600 in air (the flow rate of 100 mL/min) and argon gas atmosphere (the flow rate of 45 mL/min). Figure 2.11 shows the result of TGA. Due to the instrument sensitivity and crowded work area, instrument error due to noise is unavoidable. In air, the weight gradually reduced below 400℃ but reduced steeply above 400℃. Since more than half of the CNT spheres are CNTs, the steeple change over 400℃ might be caused by burning some of the CNTs. In argon, the weight reduced with a constant slope. Since the CNT spheres contain GAD and resorcinol, it is possible that these reagents evaporated or reacted as the temperature increased. The boiling temperature of the GAD solution is 101℃ at 1,013 hPa, and the boiling temperature of resorcinol is 178℃ at 21 hPa[166,167]. The flash point of resorcinol is 127℃[167]. As the density of the GAD solution is 1.060 g/cm^3, the GAD's weight percentage of the CNT spheres is approximately 39.8 %[166]. The resorcinol's weight percentage of the CNT spheres is approximately 6.44 %. Therefore, these materials might have gone above these temperatures either in air and argon gas.
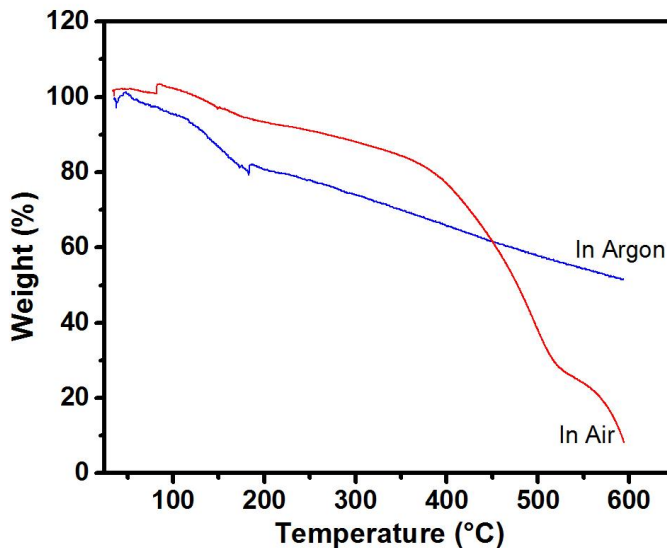
Figure 2.11 – TGA results of the CNT spheres. The weight reduced constantly below 400°C but steeply over 400°C in air while the weight reduced constantly in argon below 600°C.

2.3.6. Characterization of Specific Surface Area

Specific surface area (SSA) of a CNT sphere was measured by the surface analyzer (Quantachrome Autosorb-3b) based on Brunauer, Emmet and Teller (BET)'s equation (Equation 2.1) where W is the adsorbed gas quantity, W_m is the monolayer adsorbed gas quantity, P is the equilibrium of adsorbates at the temperature of adsorption, P_0 is the saturation pressure of adsorbates at the temperature of adsorption, and C is the BET constant ($C = K \cdot \exp\{(E_1\text{-}E_2)/RT)\}$) where E_1 is the heat of adsorption for the first layer and E_2 is that for the second and higher layers and is equal to the heat of liquefaction[168]. This equation is usually available for $0.05 < P/P_0 < 0.35$[168]. Nitrogen gas was used for this measurement.

Figure 2.12 shows the plots of the measurement and its trend line whose R^2 is 0.9086. The SSA of the CNT sphere was calculated as approximately 225 m²/g, which is not high value compared to any other 3D structure CNT materials[169].

$$\frac{1}{W[(P_0/P)-1]} = \frac{C-1}{W_mC}\left(\frac{P}{P_0}\right) + \frac{1}{W_mC}$$

Equation 2.1 – BET's equation[168].
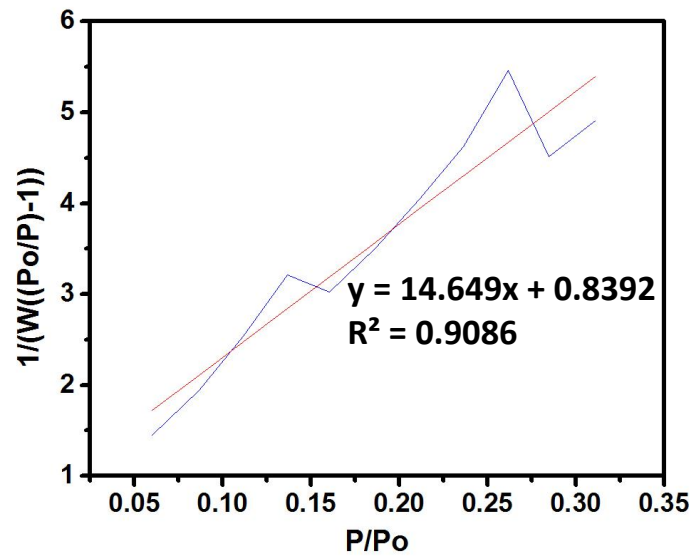
Figure 2.12 – The plots of the CNT sphere's SSA measurement (blue line) and its trend line whose R^2 is 0.9086 (red straight line).

2.3.7. Electrochemical Testing

In order to examine the electrical performance of the CNT spheres, they were tested as electrodes for supercapacitors. The electrodes were prepared by pressing the CNT spheres onto nickel foam, under a pressure of 10 MPa. The electrolyte used was a 1 M solution of potassium hydroxide (KOH) in DI water. The experiments were performed in a symmetric configuration, with the electrodes fully immersed in the electrolyte solution (Figure 2.13).
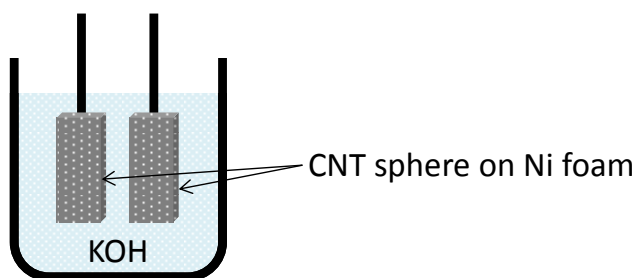
Figure 2.13 – The schematic of the experimental setup. The CNT sphere was put onto a nickel foam and compressed. The two same electrode was fully immersed in KOH.

The capacitance of the device was evaluated by cyclic voltammetry (CV) with scan rates in the range of 5 to 500 mV/s, obtained using an Autolab PGSTAT 302N potentiostat from Metrohm (Figure 2.14a). The voltammograms in Figure 2.14a shows the rectangular shape expected for capacitive behavior. The device presented poor performance at high rates and the maximum capacitance measured was 21 F/g

(Figure 2.14b). Previous reports in the literature shows CNTs-based supercapacitors tested under similar conditions presenting capacitances in the order of 150 F/g[170-172]. Figure 2.14c shows 800 cycles of charge and discharge of the CNT sphere's electrode, highlight the absence of fade in performance. The CNT spheres include functionalized CNTs, GAD, resorcinol and borax, and these ingredients were mixed in DI water, but most of the DI water was sublimated during the freeze-drying process. Although MWCNTs are basically conductive, resistances of GAD, resorcinol, and borax might reduce the electronic conductivity of the CNT spheres. Since the weight percentage of GAD and resorcinol is also more than 46 %, the excess weight of inactive materials largely limits the performance. The best carbon materials for supercapacitor applications also have specific surface areas that are at least four times larger the one measured for the CNT spheres, limiting the extent of formation of the electric double layer.
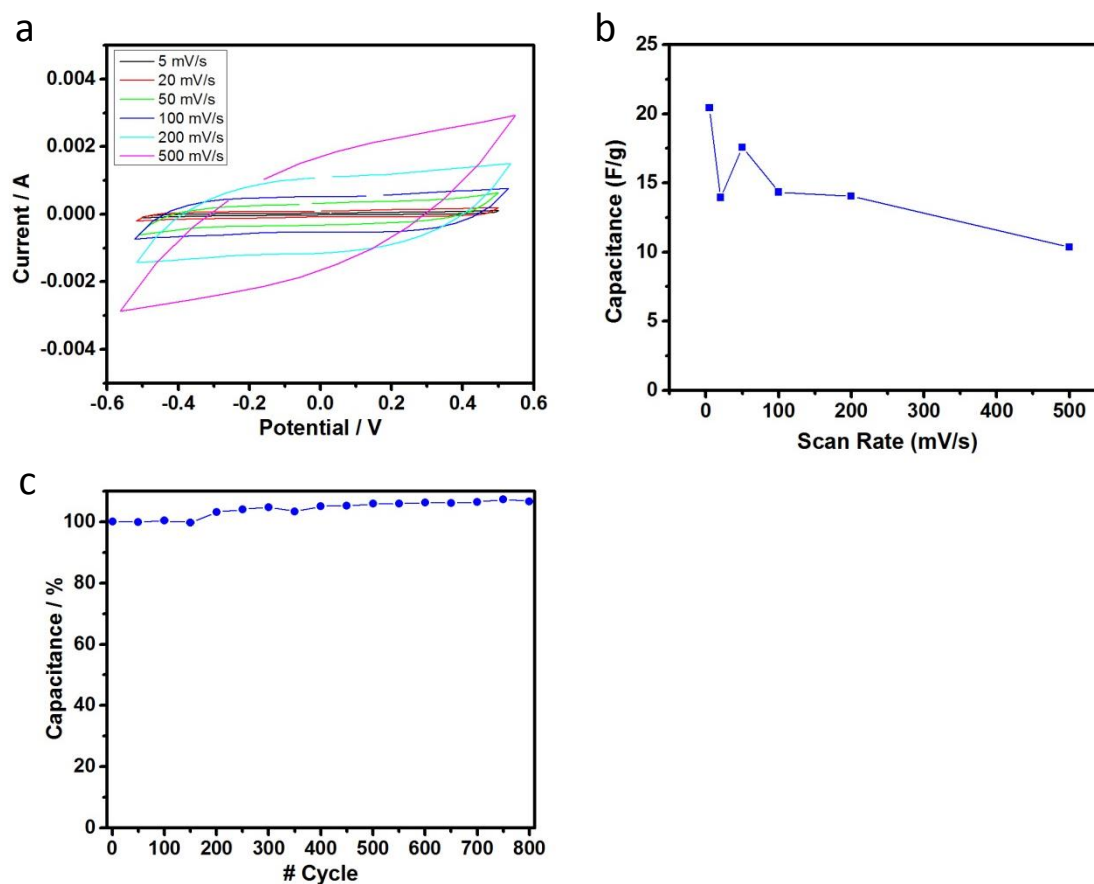
Figure 2.14 – a) The CV of the supercapacitor which consists of the CNT sphere's electrode. b)The capacitance of the supercapacitor which consists of the CNT sphere's electrode. c) 800 cycles of charge and discharge. After 800 cycles, the capacitance was stable.

2.3.8. In-situ Mechanical Testing

In order to evaluate the stiffness of CNT spheres, compression tests of a whole CNT sphere and high sensitive compression tests of a tip of CNT spheres were performed inside an SEM. Figure 2.15 shows one sequence of a compression test for a 3 mm diameter CNT sphere. The CNT sphere exhibited high elastic behavior as shown by its ability to spring back to the original shape once the load was removed. This behavior was not limited to a single loading cycle. The CNT sphere absorbed the load and dissipated it quickly thereby retaining its shape. Figure 2.16 shows an in-situ force-displacement curve of a 3 mm diameter CNT sphere. The CNT sphere was subjected to repeated load-unload cycles as shown at a strain of 10%. There was minimal loss of energy from one loading cycle to another. Furthermore, the CNT sphere exhibited very little hysteresis between cycles. In addition, the CNT sphere did not show any noticeable deformation after five cycles, maintaining its spherical shape. For a load less than 200 μN, the CNT sphere exhibited complete elastic behavior. The log-log plot on the elastic limit region allowed calculation of Young's modulus of the spheres (inset of Figure 2.16).

To further elucidate on the mechanical properties of interconnected CNTs in the CNT spheres, nano-indentation tests were carried out. Figure 2.17 shows the results of the highly sensitive compression tests. The highly sensitive compression tests were also done inside an SEM chamber as in-situ tests, and an SEM PicoIndenter (xrPI85, Hysitron, Inc., USA) tip used to push an outer scaffold structure of a CNT sphere. The loads selected were 1, 10, 15, 20, 30 and 50 μN. The scaffold parts showed high levels of elasticity and no hysteresis was observed. The

mechanical response of a spherical body under compression between two flat rigid surfaces is approximately expressed as Equation 2.2, where F is the applied force, R is the initial radius of sphere, E is the Young's modulus, v is the Poisson's ratio of the sphere which is assumed as zero due to its porous structure and h is deformation. The Young's modulus of a CNT sphere was measured as 4.2 KPa. Also, the Young's modulus of the tip of a CNT sphere was measured as 102.5±0.5 GPa at the low load compression of 10 µN. The Young's modulus of the CNT spheres should be smaller since the CNT spheres have porous structures whereas the Young's modulus of the tip of the CNT spheres might be larger because the tip consists of interconnected CNTs.

$$\mathrm{F} = \left(\frac{4R^{1/2}E}{3 \cdot 2^{3/2}(1 - v^2)}\right) h^{3/_2}$$

Equation 2.2 – Spherical body mechanical response.
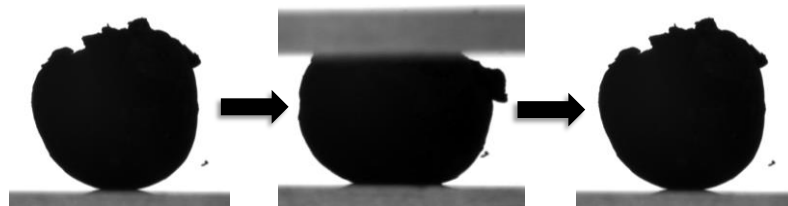
Figure 2.15 – A whole procedure of a compression test of a CNT sphere. The left is the initial state, the middle is the loading state, and the right is the final state. The final state's shape of the CNT sphere is almost same as the initial state.
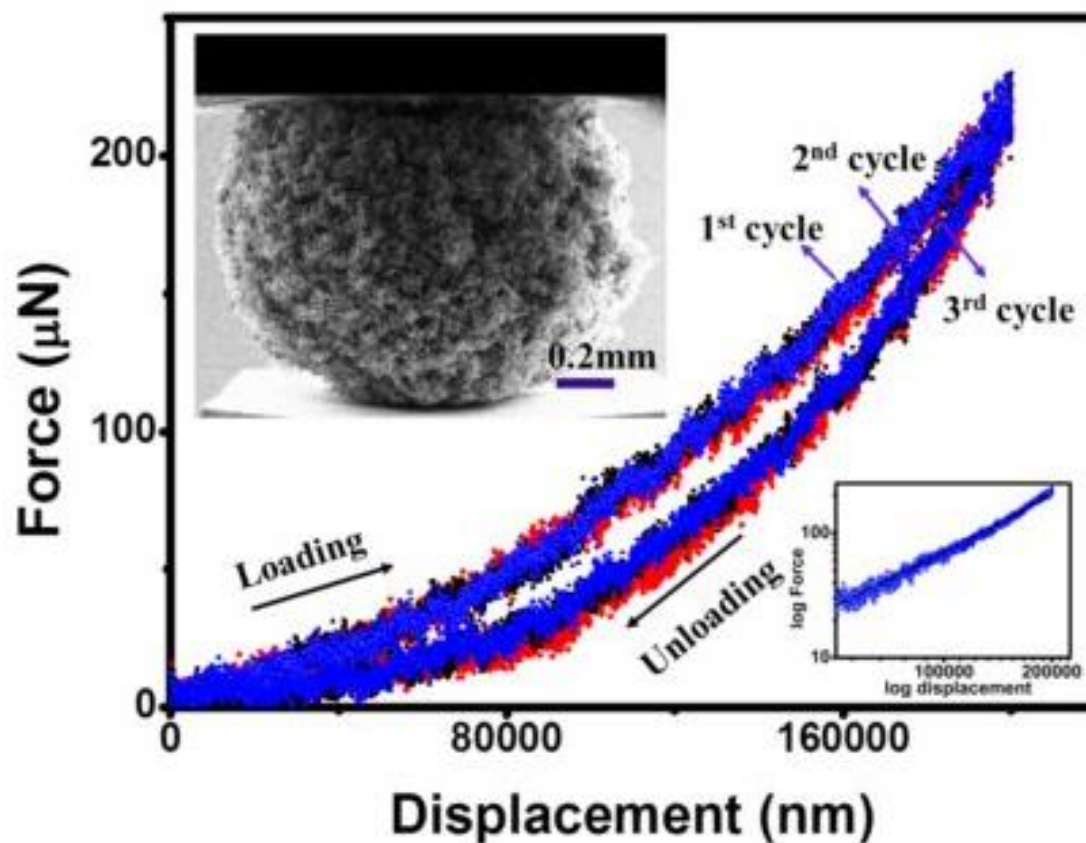
Figure 2.16 – Load and unload curves of the mechanical test. A CNT sphere behaves elastic performance. The inset picture is the state during loading and unloading test inside SEM. The inset graph shows log scale plots.
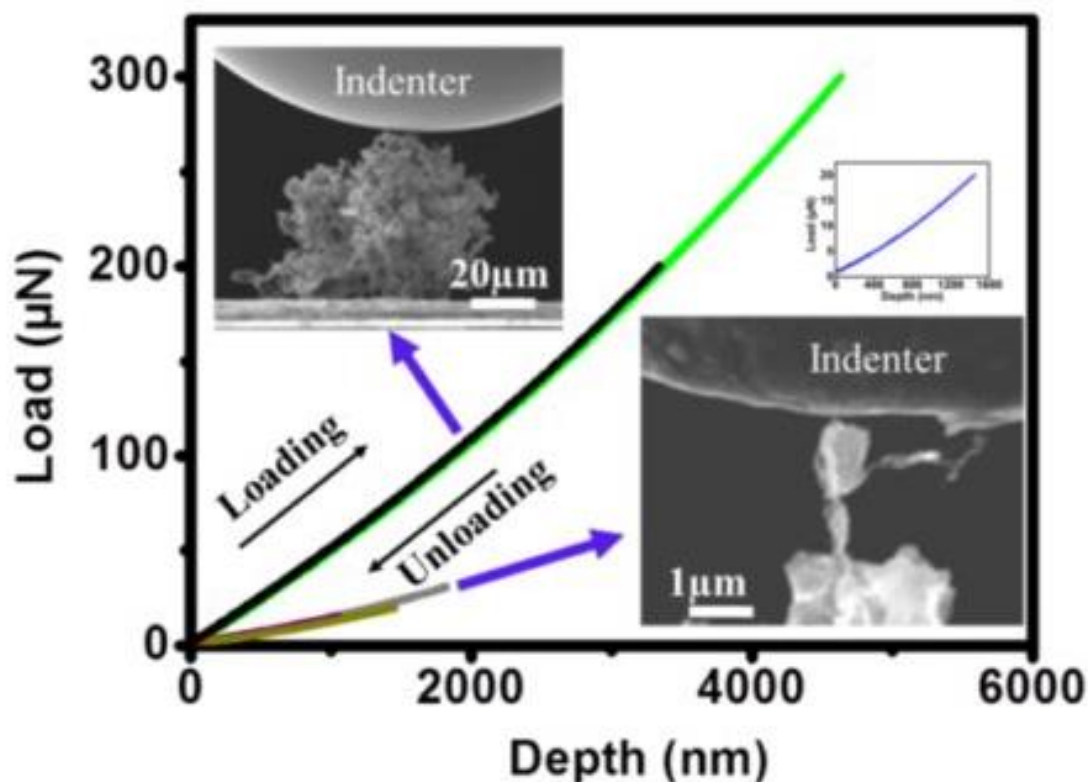
Figure 2.17 – High sensible load and unload curves of mechanical test. The loading and unloading curves are almost same treats. The two inset pictures are the tip of a CNT sphere during loading and unloading test inside SEM. The inset graph shows the magnification for small depth.

2.3.9. MD Simulation

MD simulations using the CHARMM force field as available in the LAMMPS code help to understand the mechanism of the role of functional groups[173-175]. The CNT simulation model was (10,10) chirality and 180 Å length. The functional groups were attached around the CNT's 20% of its external area. All of the parameters needed for this calculation were obtained from CGenFF[176]. During

simulations, the temperature was maintained at 10 K by a canonical ensemble, and all of the simulation models tried to imitate experimental conditions. Figure 2.18 shows the condition of a compression test. CNTs gathered like interconnected scaffold structures, and a tiny indentor (blue sphere; 90 Å of radius) pushes the CNTs' aggregation. Figure 2.18 (a) shows initial state of simulation of the interaction among functionalized CNTs, and Figure 2.18 (b) shows the interaction among pristine CNTs. The compression rate was a constant value as 0.4 Å/ps. Figure 2.19 shows the whole sequence of compression tests. The top row shows the whole sequence of functionalized CNTs, and they retained their interconnected structure even after unloading an indentor. However, the bottom row shows the whole sequence of pristine CNTs, and it was no longer a formed structure even at maximum loading (at 210ps). The middle row shows the condition of atoms' interaction during the tests. It shows that the functionalized group got together mainly because of Van der Waals force, while compression process and the interaction helped to remain the aggregation. The simulation also indicated the influence of Van der Waals energy. The Van der Waals energy of a charged part of functionalized CNTs changed a small amount around 0.05 kcal/mol/atom whereas the energy of a non-charged part of functionalized CNTs did not change (Figure 2.20). Figure 2.20 also shows the Van der Waals energy of pristine CNTs around 0.45 kcal/mol/atom due to the increase of contact area among the CNTs.
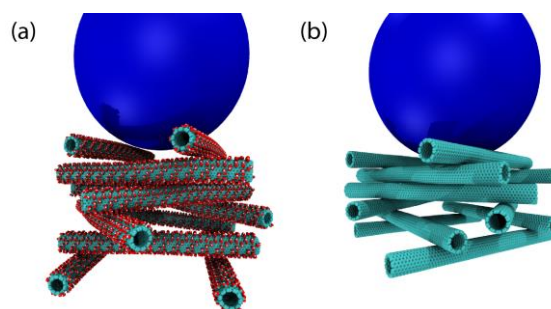
Figure 2.18 – Initial states of MD simulation (compression test). (a) Functionalized CNTs (CNT-COOH). (b) Pristine CNTs.
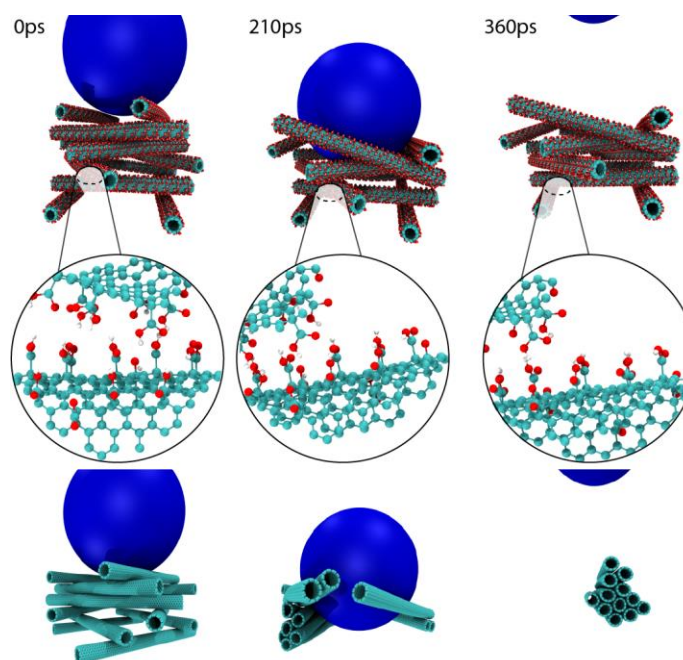
Figure 2.19 – A whole procedure of a compression test. The left column is the initial state (0 ps). The middle column is the maximum compression state (210 ps). The functionalized CNTs' structures retained the structure while the prictine CNT structures were broken. The right column is the final state (360 ps).
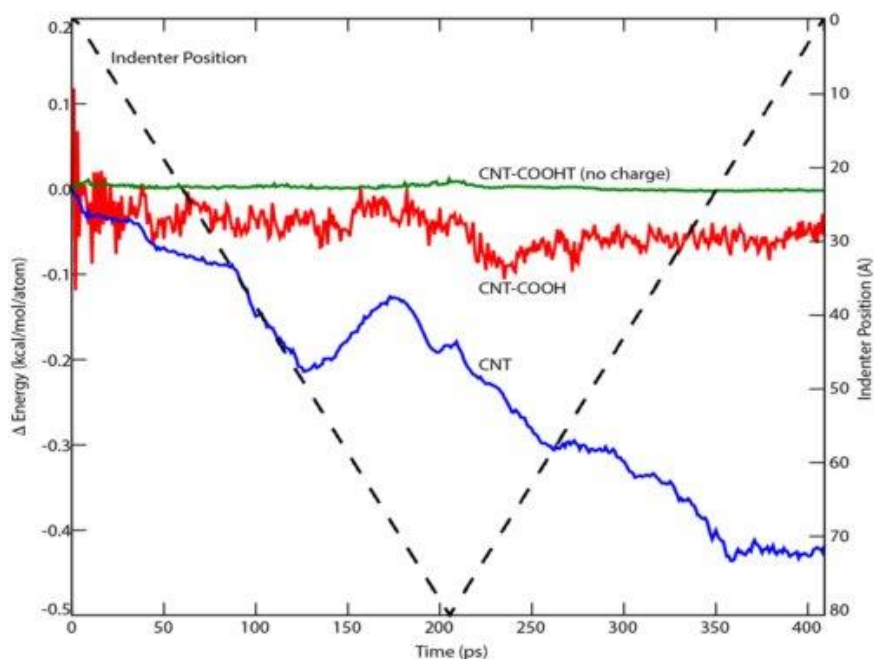
Figure 2.20 – Van der Waals energy evolution depending on the indenter position (The black dot line). The green line shows functionalized CNTs without charge and it behaved almost no Van der Waals energy change. The red line shows functionalized CNTs with charge and it behaved small amount of change around 0.05 kcal/mol/atom. The blue line shows pristine CNTs and it behaved around 0.45 kcal/mol/atom of change.

2.4. Summary

This chapter is focused on sphere shaped structures of interconnected CNTs using functionalized CNTs (CNT-COOH). A freeze-drying method can help for forming porous structures consisting of interconnected CNTs because a lyophilization process helps to remove water from the sample. Referring to previous studies[125,128], 3D interconnected structures can be shaped via a freeze-drying method using GAD, resorcinol and borax for functionalized CNTs which have carboxyl groups (CNT-COOH).

The CNT scaffold structures formed a sphere-shape inside liquid nitrogen, and the porous structures were shaped by removing inside water after a few days freeze-drying. Since the CNT spheres are synthesized by dropping the solution into liquid nitrogen using a pipet or needle, it is suitable for mass production because the spheres can be made continuously. After forming the CNT spheres, it was confirmed that the CNTs inside the spheres still retained their initial structures by Raman microscopy, XRD and XPS measurements. A series of three Raman spectra show CNTs can retain their structure even after functionalization (CNT-COOH) and the spheres' formation. XRD and XPS measurements of the CNT spheres also show typical CNT peaks. The TGA result shows the weight of the CNT sphere reduced gradually before CNTs' burning out when the temperature increased. Since the weight percentage of GAD and resorcinol is totally about 46 %, their evaporation and/or reaction should not be negligible. Although the CNT spheres seemed to have wider surface area due to their scaffold structures and SSA value, the performance

as an electrode for a supercapacitor was relatively low because the CNT spheres contain not only CNTs but also GAD and resorcinol. The effect of GAD and resorcinol is significant because of their weight percentage of the CNT spheres. In-situ mechanical test inside the SEM chamber was carried out, and both the CNT spheres and the tip of the CNT spheres behaved elastically under the load conditions. In order to understand the mechanism of interconnected CNTs, MD simulations were carried out and interaction of functionalized CNTs to maintain scaffold structures was revealed. Functionalized CNTs play a significant role in maintaining the structure by the interaction of functional groups.

Although the CNT spheres were synthesized by a method previously performed by others using GO, which typically has carboxyl groups (-COOH), hydroxyl groups (-OH), and epoxy groups (-CH$_3$), the spheres synthesized here used CNTs which were only functionalized with carboxyl groups (-COOH). The nano indentor test showed the CNT spheres were elastic under the test conditions, though it might be possible to build stronger structures if there were also hydroxyl and epoxy groups present. Since the CNT spheres can only behave elastically under microscale loading, stronger structures with additional functionalization might have mechanical properties similar to those in previous GO work. However, it is difficult to form 3D porous structures as strong as previous GO work because CNTs are a so-called 1D material.

2.5. Application and Future Work

The advantageous features of the CNT spheres are that they are a mainly lightweight (low density) porous material with high stiffness that are easily synthesized for mass production. Although one sphere breaks easily under practical usages (the order of N or kN), their easy mass production makes them ideal for use in large amounts to be used synergistically. Since the CNT spheres have high stiffness in spite of its low density, the CNT spheres might have some shock absorbing performances due to its scaffold structures if many samples of the CNT spheres are coated together by some polymers such as poly-dimethylpolysiloxane (PDMS).

Chapter 3

Carbon Nanotube Synthesis on Graphene Oxide and hexagonal Boron Nitride

3.1. Overview and Motivation

Hybrid materials consisting of 2D materials--such as graphene and h-BN--, and CNTs exhibit intriguing electronical properties due to their large surface areas[137-139]. There are a multitude of reports of the hybridization of CNTs and various 2D materials which comes about by either physical or chemical bonding them to each other[140,141]. Usually, physically combined hybrid materials are made by mixing CNTs and 2D materials like a "sandwich," whereas the chemical ones are synthesized by CNTs' growth on 2D materials' surface "bottom-up synthesis"[142-146].

This chapter discusses two types of bottom-up synthetic methods for hybrid structures of CNTs built with 2D materials. There are few reports which compare the electro-chemical properties between "CNTs and conductive 2D materials" and "CNTs and non-conductive 2D materials." The comparison of two similar structure types of hybrid materials provides interesting features when they are applied to an electrode. Graphene has a hexagonal layer structure only consisting of carbon atoms, while h-BN has a hexagonal layer structure consisting of boron and nitrogen atoms. Despite comparable material properties between these two nanomaterials, h-BN is not a conductive material as opposed to graphene[129-132].

For graphene hybrid materials, GO and/or rGO can also be used as the surface materials. As rGO is one of the most commonly utilized graphene materials for the application of supercapacitors, there are many reports of its material properties and potential for these devices[86-89]. For h-BN based hybrid materials, boron nitride tube has been examined by many researchers, but there are few reports regarding CNTs and h-BN being chemically bonded to form the hybrid structure. Since both hybrid materials have large surface areas, they can be considered as suitable for supercapacitor's electrodes.

3.2. CNT Synthesis on 2D Materials

3.2.1. CNT Synthesis on rGO

First, GO was synthesized by the improved Hummer's method[80]. The seed graphite powder (45 µm, 99.99%, SP-1 Bay Carbon) 3 g, potassium permanganate ($KMnO_4$) 18 g, phosphoric acid (H_3PO_4) 40 mL and sulfuric acid (H_2SO_4) 360 mL were mixed and stirred at 50-60℃ for 12 hours. After that, the mixed solution was poured into ice water, and hydrogen peroxide (H_2O_2) 14 mL was added. Then, the solution was stirred for 3 hours, and filtered using a vacuum filtering setup. The filtered sample was washed using DI water, 30 % hydrochloric acid (HCl) and ethanol 2 times for each cycle.

After the synthesis, the wet GO sample was dried on a hotplate at 80℃ in order to accelerate its dehydration. The GO seed was dispersed in DI water (60 mg GO/6 mL DI water), and the GO solution was sonicated by an ultrasound sonicator for 30 minutes. The mixed GO solution was poured onto a nickel foam (2 cm × 2 cm) using a vacuum filtering setup to help dry for 3 days at room temperature. Although GO was dried by a hotplate, it was confirmed GO was not reduced but retained its structure as a GO by XRD and XPS.

The GO on nickel foam sample was cut to the size 1 cm × 1 cm, and put into a glass tube of the WACVD setup. Figure 3.1 shows a schematic figure of CNT growth procedure on rGO. CNTs were synthesized by the WACVD method whose carbon source was ethylene (C_2H_4) at 775℃, inside 15 % hydrogen balanced argon gas atmosphere, for 30 minutes (Figure 3.2). During the CNT growth, a minimal amount

of water vapor was supplied in order to remove amorphous carbon and help the CNT synthesis. Figure 3.3 shows the optical images of samples. Figure 3.3A is GO on a nickel foam before the CNT growth sample, and Figure 3.3B is CNTs on rGO sample after the CNT growth. Before the CNT growth sample was covered by GO on the entire surface whereas almost half the area of GO was removed after the CNT growth due to temperature and air flow during the growth.

Usually, some catalysts or templates are required to synthesize CNTs. For this method, further catalysts or templates are not needed for CNT growth because a nickel foam can act as a catalyst. Although CNTs were synthesized on rGO even when aluminum and iron were deposited on the GO surface as its catalysts, it is feasible to make if any further catalysts or templates are not required.
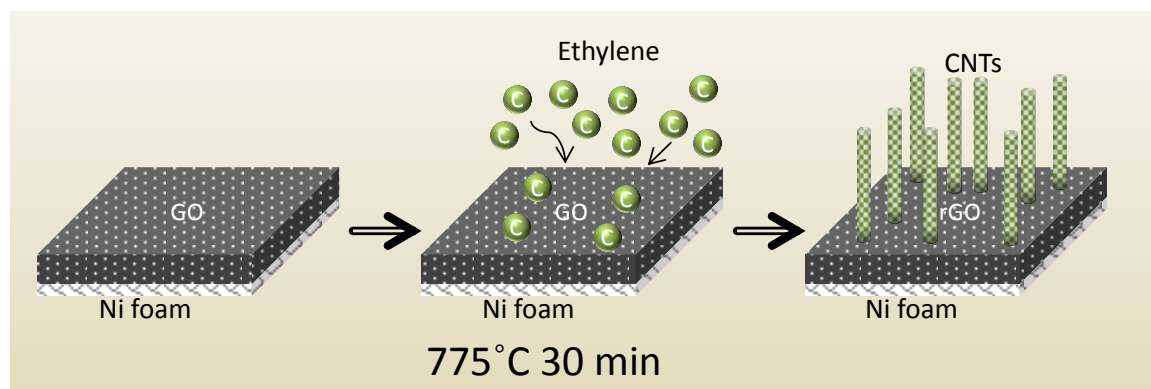
Figure 3.1 – Schematic figure of CNT growth procedure on rGO. The left shows the initial state which GO is prepared onto a nickel foam. The middle shows CNTs that are synthesized on GO and reduced to rGO. The right shows the final state which CNTs are grown on the rGO surface.

Figure 3.2 – Image of the WACVD setup. There are mass flow controllers (MFCs) on the left side. They can supply argon gas, 15 % hydrogen balanced argon gas and ethylene gas. The water bubbler is located behind the furnace. These gases and bubbled water are combined at the inset of the glass tube at the furnace.
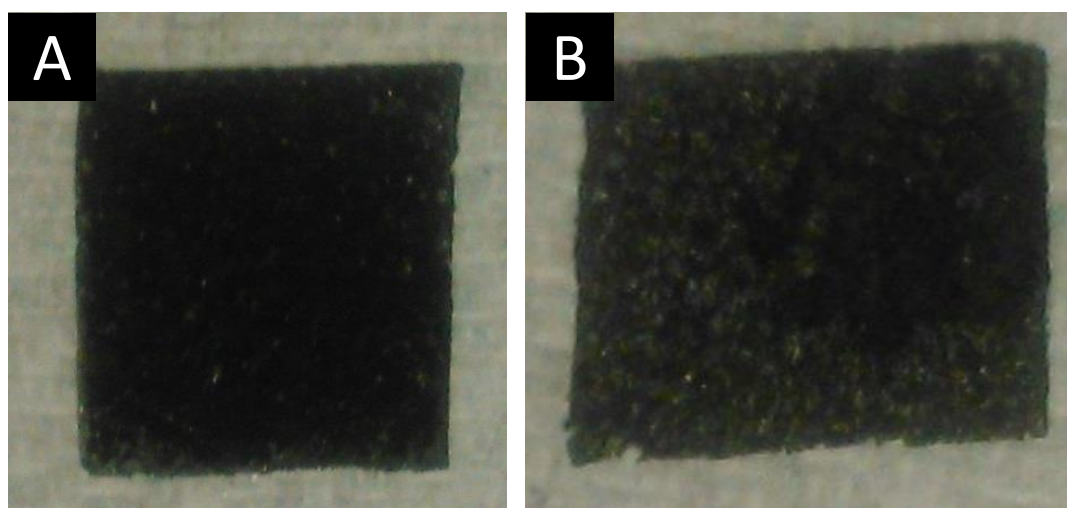
Figure 3.3 – The optical images of the samples. A) Before CNT growth (GO on nickel foam), B) After CNT growth (CNTs on rGO).

3.2.2. CNT Synthesis on h-BN

The powder of h-BN (Sigma-Aldrich Co. LLC., ~1 μm, 98%) was dispersed in IPA (60 mg h-BN/6 mL IPA), and then sonicated by an ultrasound sonicator for 30 minutes. The h-BN solution was poured onto a nickel foam and dried at room temperature for 3 days. Aluminum (10 nm) and iron (1.5 nm) were then deposited on the surface of the h-BN on nickel foam as the catalysts by e-beam evaporator.

The h-BN on nickel foam sample was cut to the size 1 cm × 1 cm, and then put into a ceramic boat and put into a CVD setup. Figure 3.4 shows a schematic figure of the CNT growth procedure on h-BN. CNTs were grown by CVD whose carbon source was xylene (C_8H_{10}) at 790℃, 15 % hydrogen balanced argon gas atmosphere, for 2 hours (Figure 3.5). Xylene was injected by a syringe at a liquid injection rate of 12 mL/hour. Figure 3.6 shows optical images of the samples. Figure 3.6A shows h-BN on a nickel foam before the CNT growth sample, and Figure 3.6B shows CNTs on h-BN sample after the CNT growth. Unlike CNTs on rGO sample, h-BN remained on the nickel foam surface even after CNT growth. Also the surface color turned black after growth due to the existence of carbon.

For this method, catalysts were required to obtain CNTs because CNTs were not synthesized on the h-BN surface without any catalysts even though there was a nickel foam.
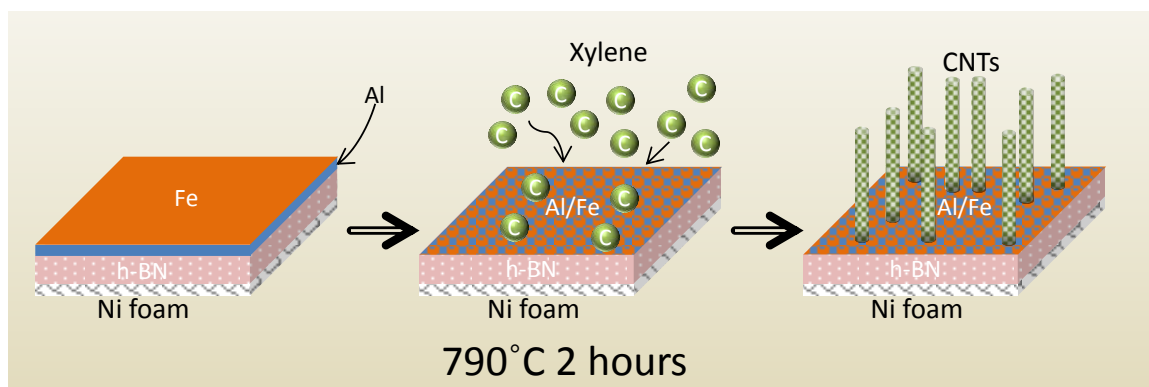
Figure 3.4 – Schematic figure of the CNT growth on h-BN. The left shows the initial state of h-BN with alminum and iron catalysts prepared on nickel foam. The middle shows CNTs synthesized on the h-BN surface. The right shows the final state of CNTs grown on the h-BN surface.

Figure 3.5 – The overall pictute of the xylene CVD setup. There are gas flow lines with a flow meter on the left of the wall. They can supply argon gas or 15 % hydrogen balanced argon gas. There is a liquid injector with a syringe that supplies xylene at a constant rate.
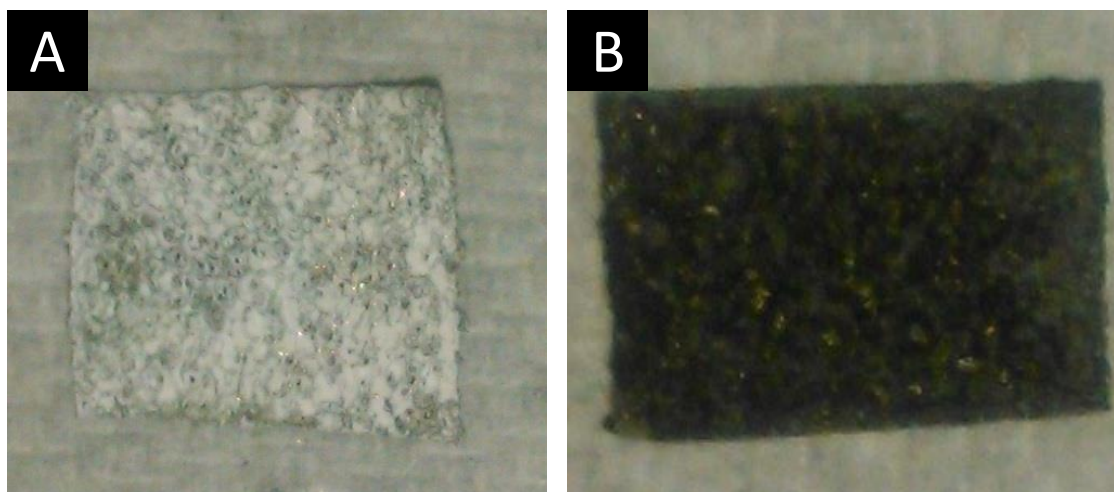
Figure 3.6 – The optical images of the samples. A) Before CNT growth (h-BN on nickel foam), B) After CNT growth (CNTs on h-BN).

3.3. Results and Discussion

3.3.1. Characterization by Electron Microscopy

The characterization by electron microscopies were carried out by FEI Quanta 400 SEM at accelerating voltage of 20 kV and JEOL 2100 field emission gun TEM at operating at 200 kV. Figure 3.7A-D show SEM images of CNTs on rGO samples. Figure 3.7A is a low magnification image of the sample, and CNTs on rGO pieces are placed on nickel foam. Figure 3.7B-D show there are CNTs on rGO distributed over the surface. Figure 3.7C shows there are CNTs even inside the layer of rGO. Although rGO layers are not flat and single, CNTs can be grown on rGO surfaces even inside the layer. Figure 3.7D is a high magnification SEM image of CNTs on the rGO sample. The CNTs are not straight or aligned but randomly

oriented. The diameter of the CNTs is estimated at a few dozen nano meters and are MWCNTs. Figure 3.7E,F are high magnification TEM images of the CNTs on rGO sample. These images show that the CNTs and rGO interfaces are chemically connected at the root of CNTs, and the images also show the synthesized CNTs are MWCNTs. Figure 3.7E shows metal particles at the top of the CNTs. Although further catalysts were not deposited, a nickel particle evaporated from a nickel foam behaved as a catalyst.

Figure 3.8A-D show SEM images of CNTs on h-BN samples. Figure 3.8A is a low magnification image of the sample. Unlike CNTs on rGO sample, CNTs on h-BN pieces are placed all over the nickel foam. Figure 3.8B-D show there are CNTs on the entire h-BN surface, and there are also CNTs inside the layer of h-BN surface. Therefore, CNTs can be grown even inside the layers of both rGO and h-BN. CNTs are not straight or aligned but randomly oriented as well as CNTs on the rGO sample. Figure 3.8E,F are high magnification TEM images of CNTs on h-BN sample. These images show that the CNT and h-BN interface are chemically connected at the root of the CNTs. The diameter of the CNTs is estimated at a few dozen nano meters and is MWCNTs as well as CNTs on rGO. However, the CNTs do not appear hollow but rather are filled on the inside. Therefore, it is possible that the CNTs contain atoms from catalyst metals--aluminum and iron--, a nickel foam and h-BN.

For both samples, each sample was dispersed in IPA and sonicated about 20 minutes when each TEM sample was prepared. Since each TEM images show CNTs and rGO and h-BN are directly connected to each other, this fact helps to estimate that these materials are connected chemically.
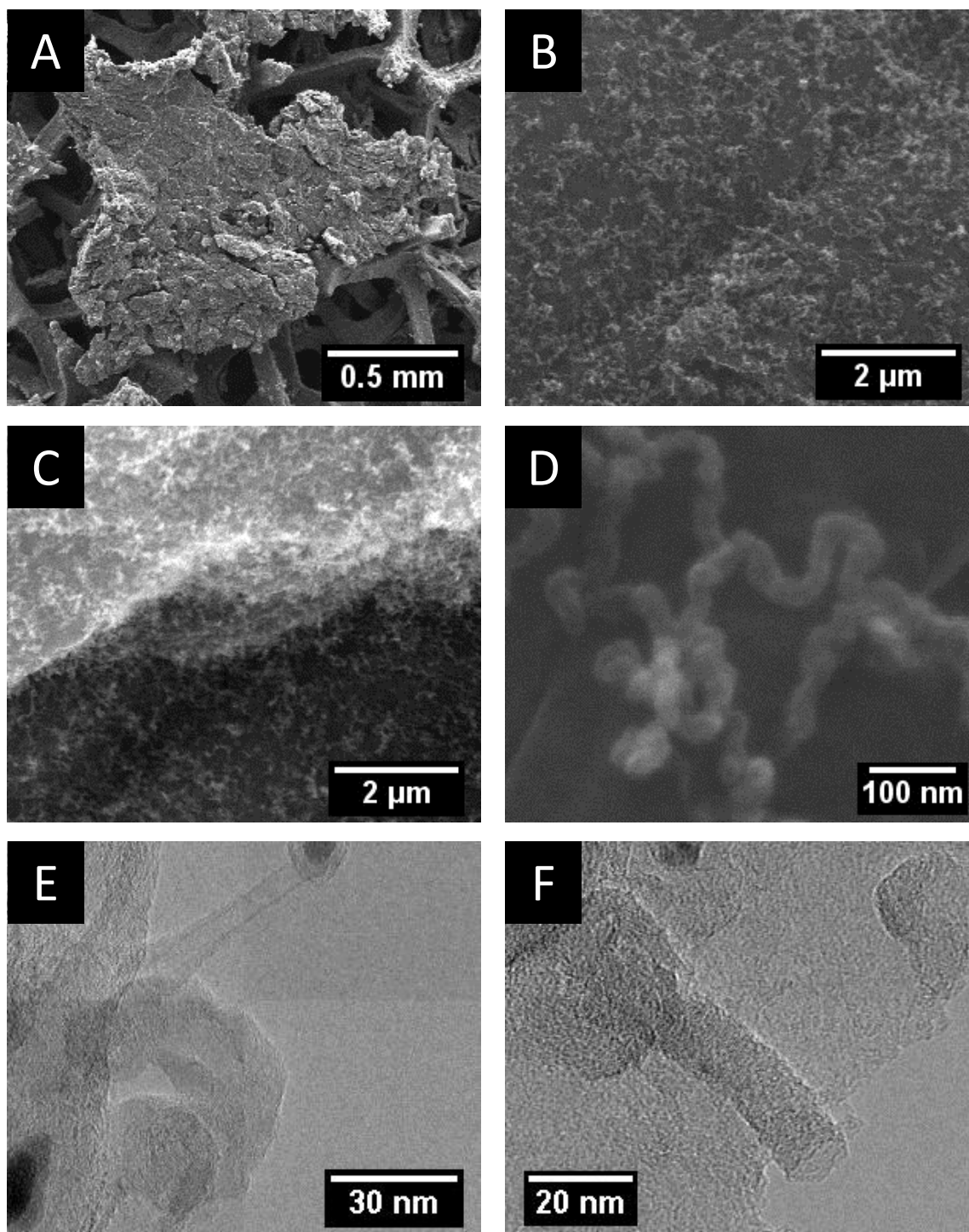
Figure 3.7 – The electron microscopy images of CNTs on rGO sample. A-D) SEM images of CNTs on rGO sample. E,F) TEM images of CNTs on rGO sample.
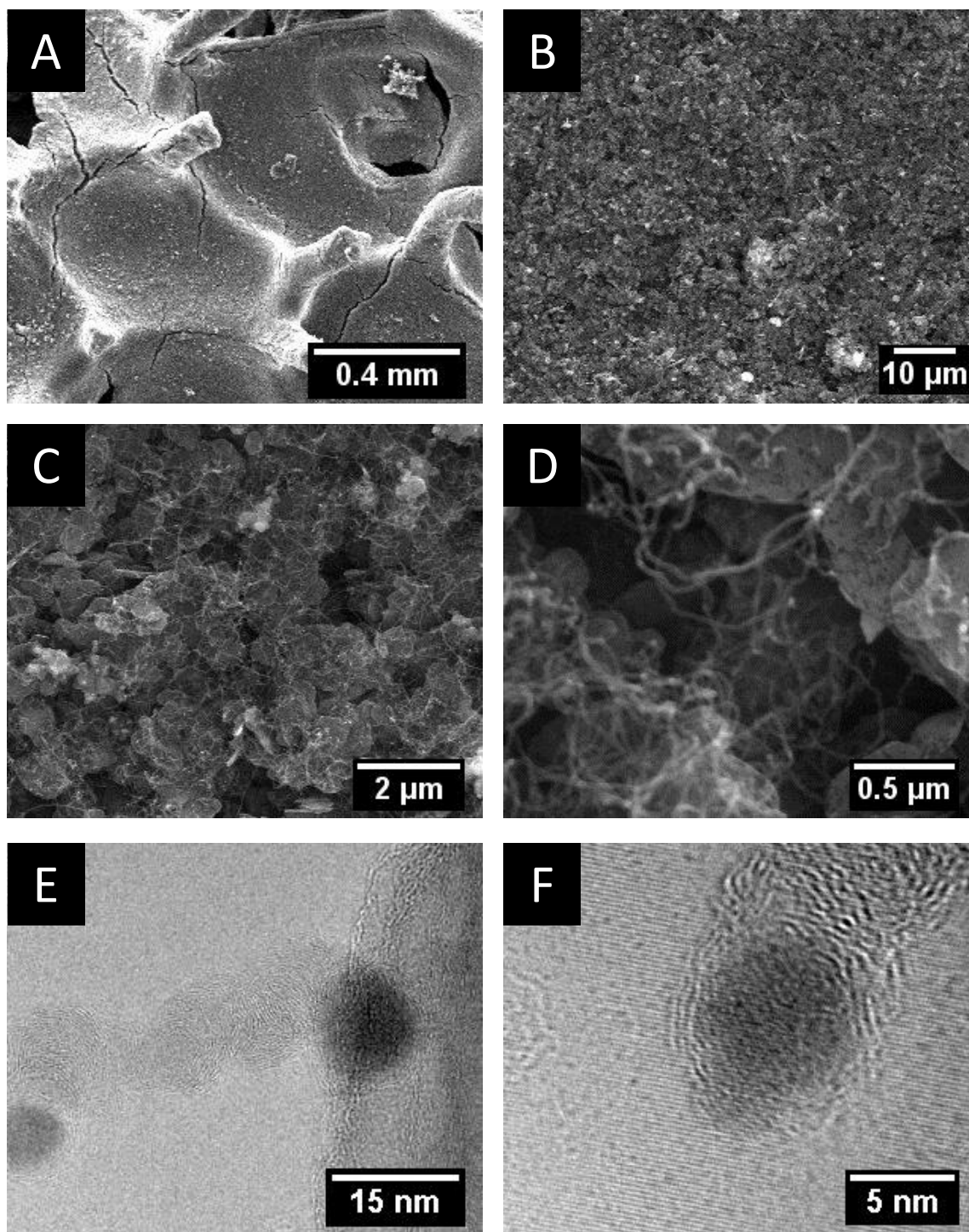
Figure 3.8 – The electron microscopy images of CNTs on h-BN sample. A-D) SEM images of CNTs on h-BN sample. E,F) TEM images of CNTs on h-BN sample.

3.3.2. Characterization by Raman Microscopy

Raman spectra of the samples were carried out by RENISHAW inVia Raman Microscope using a 514 nm laser. Figure 3.9a shows Raman spectra of CNTs on rGO samples. The spectrum shows typical GO peaks which contain a D band at 1,363 cm^{-1} and a G band at 1,597 cm^{-1} before the CNT growth[163]. On the other hand, Raman spectrum shows typical CNT peaks which are D band at 1,359 cm^{-1}, G band at 1,584 cm^{-1} and 2D (G') band at 2,726 cm^{-1} after CNT growth[163]. This result shows CNTs were detected after their growth procedure. After the CNT growth, each peak is clearer than GO, and the density of defects (I_D/I_G) is less than one (approximately 0.46). This result also shows the CNTs have fewer defects or insufficiencies comparing with the CNTs which have greater D band peak than G band's.

Figure 3.9b shows Raman spectra of CNTs on h-BN samples. There is a typical h-BN peak at 1,366 cm^{-1} before CNT growth and typical CNT peaks which incorporate a D band at 1,351 cm^{-1} and a G band at 1,591 cm^{-1}[163,177]. This result also shows CNTs were detected after their growth procedure as well as CNTs on rGO sample. However, the peaks of D band and G band are relatively dull and there is no clear peak of 2D (G') band after CNTs' growth. The I_D/I_G ratio is approximately 0.97. While the I_D/I_G ratio is below one, the value is more than double of the value of CNTs on rGO sample. Therefore, the quality of CNTs is worse than CNTs on rGO samples.
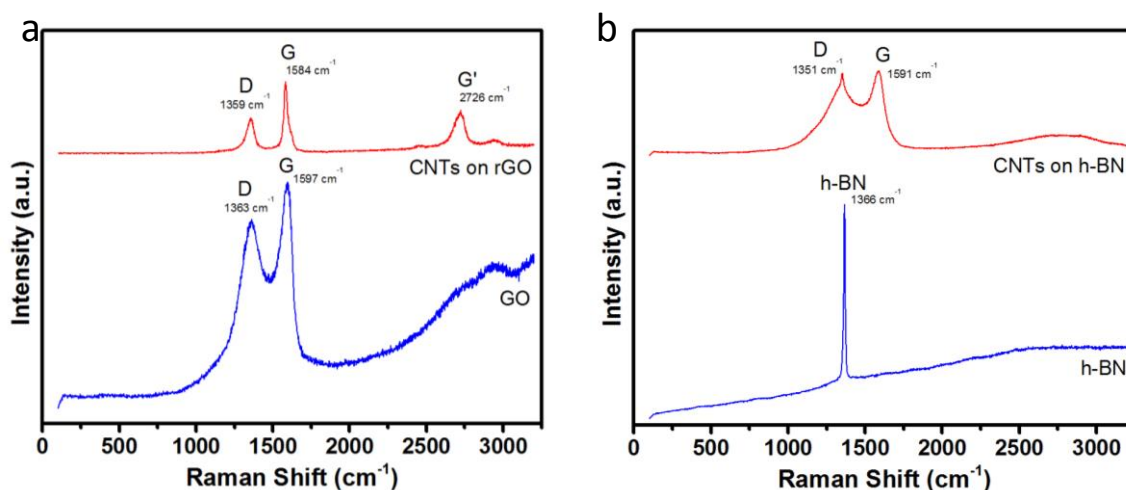
Figure 3.9 – a) Raman spectra of CNTs on rGO. There are clear peaks of the D band, G band and G' band, and the value of I_D/I_G is less than half after CNT growth. b) Raman spectra of CNTs on h-BN. There are relatively dull peaks of the D band and G band, and the value of I_D/I_G is almost 1 after CNT growth.

3.3.3. Characterization by XRD

XRD pattern was measured by Rigaku D/Max Ultima II Powder XRD using a CuKα x-ray tube. Figure 3.10a shows XRD patterns of CNTs on rGO samples. The XRD patterns show a typical GO peak of 10.68° (2θ) before CNT growth while show typical CNT peaks which are (002) at 26.16° (2θ) and (100) at 44.5° (2θ) after the CNT growth[164]. This result shows CNTs were detected and the GO peak disappeared after the growth procedure. Although the GO was dried by a hotplate when it was prepared, this XRD pattern shows the GO was not reduced during drying but rather was reduced during the CNT synthetic procedure.

Figure 3.10b shows XRD patterns of CNTs on h-BN samples. The XRD pattern shows typical h-BN peaks which are (002) at 26.65° (2θ), (100) at 41.56° (2θ), (101) at 43.90° (2θ), (102) at 50.12° (2θ), (004) at 55.05° (2θ) and (110) at 75.91° (2θ) before CNT growth[178]. On the other hand, XRD pattern shows typical CNTs and h-BN's peaks which are (002) at 26.73° (2θ), (100) at 41.68° (2θ), (101) at 44.00° (2θ), (102) at 50.12° (2θ), (004) at 55.14° (2θ) and (110) at 75.98° (2θ) after CNT growth[178]. The result shows h-BN retained its structure even after the CNT growth. However, since the degree positions of typical CNT peaks which are C(002) and C(100) are almost same as h-BN's, it is hard to determine that there are CNTs by this XRD pattern.
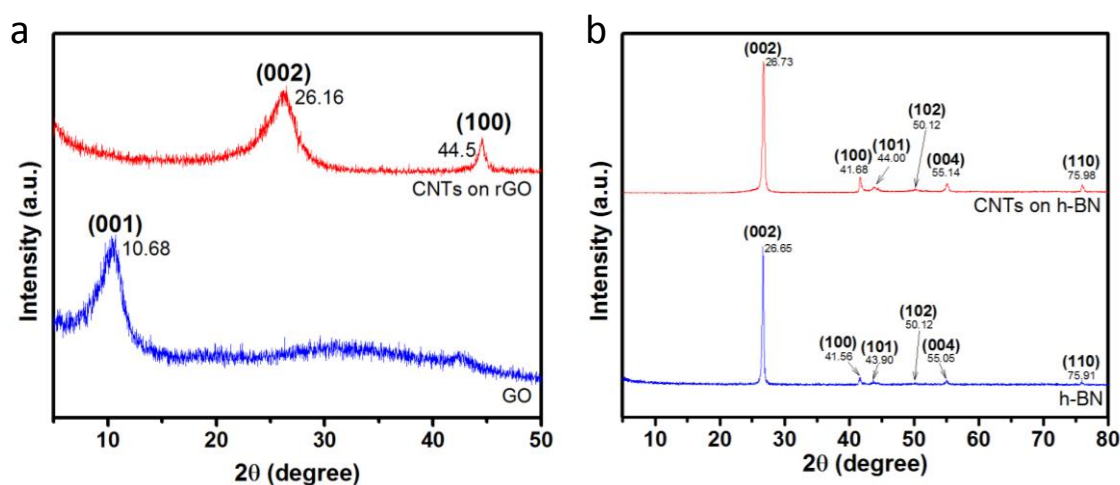
Figure 3.10 – a) XRD patterns of CNTs on rGO. There are two major peaks which are C(002) at 26.16° and C(100) at 44.5° after the CNTs' growth. b) XRD patterns of CNTs on h-BN. There are typical h-BN peaks.

3.3.4. Characterization by XPS

XPS pattern was examined by PHI Quantera XPS using an AlKα x-ray tube. Figure 3.11 shows an XPS pattern of a survey scan for CNT on rGO samples. This XPS pattern shows C1s and O1s peaks before the CNT growth while XPS pattern shows larger C1s peak and smaller O1s peak after CNT growth. The lower inset of Figure 3.11 shows C1s detail scan of CNTs on rGO sample before CNT growth. This pattern shows a typical GO pattern which corresponds to C-C bonding at 284.4 eV, C-O bonding at 286.6 eV, C=O bonding at 287.9 eV and O-C=O bonding at 289.1 eV[80]. The upper inset of Figure 3.11 shows a C1s detail scan of CNTs on rGO sample after CNT growth. This pattern shows a typical CNT pattern which is C-C bonding at 284.5 eV, C-O bonding at 286.3 eV, C=O bonding at 288.9 eV and O-C=O bonding at 291.0 eV. This same inset also shows that the C-O and C=O peaks are much more decreased[165]. This exhibits that GO was reduced during the CNT synthesis and was no longer existed after the CNT growth. It also shows GO was not reduced during drying by a hotplate.

Figure 3.12 shows the XPS pattern of a survey scan for CNTs on h-BN samples. This XPS pattern shows B1s, C1s, O1s and N1s peaks before CNT growth while XPS pattern shows larger C1s peak and smaller O1s peak after CNT growth. The inset of Figure 3.12 shows a C1s detail scan of CNTs on h-BN after CNT growth. This pattern is a typical CNT pattern which incorporates C-C bonding at 284.5 eV, C-O bonding at 286.3 eV, C=O bonding at 288.7 eV and O-C=O bonding at 291.0 eV, and almost the same as CNTs on rGO (after CNT growth)[165]. Since XPS measures the surface area of a sample, the pattern after the CNT growth shows the surface of

CNTs on h-BN was covered mainly with CNTs because B1s and N1s peaks were almost disappeared. Also the CNTs are mainly consisted of carbon atoms due to a larger C1s peak; however, h-BN retained its structure under the surface of the sample according to XRD result.
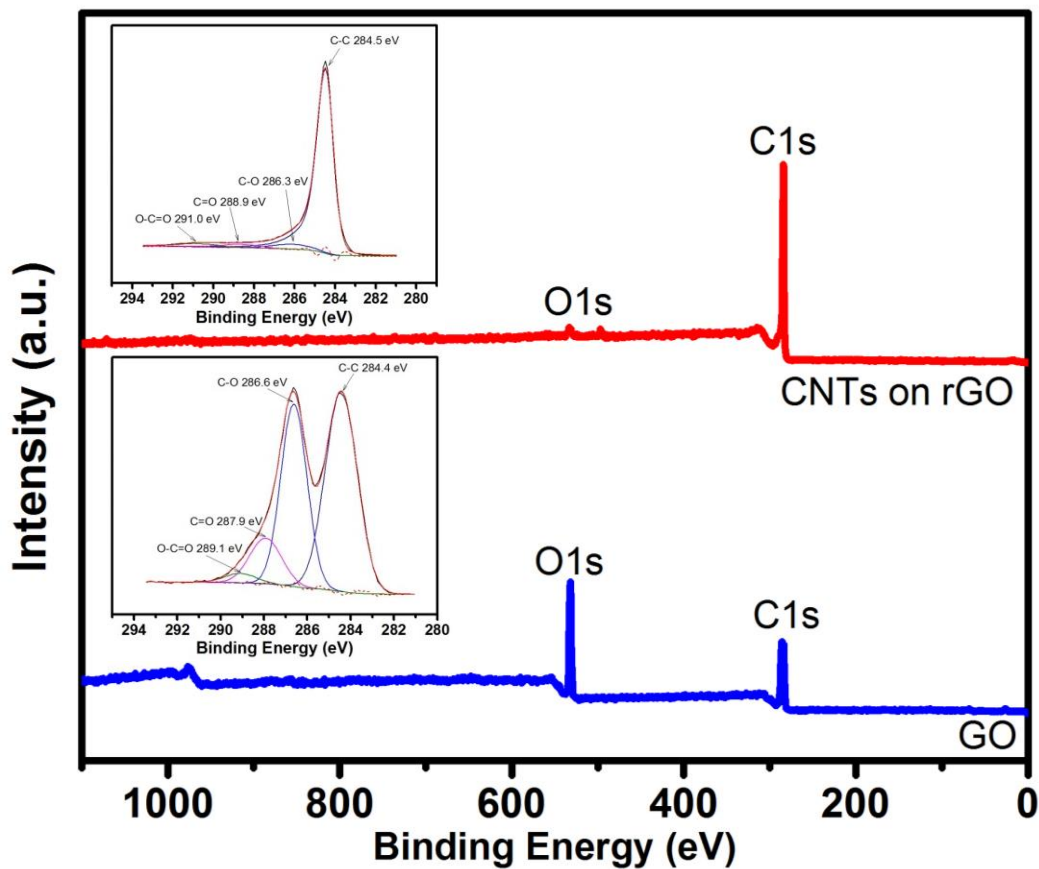
Figure 3.11 – XPS patterns of CNTs on a rGO sample. The red line shows the pattern of CNTs on rGO (After CNT growth). The blue line shows the pattern of GO (Before CNT growth). The upper inset shows a detail scan of the C1s peak for CNTs on rGO sample. The lower inset shows detail scan of a C1s peak for GO.
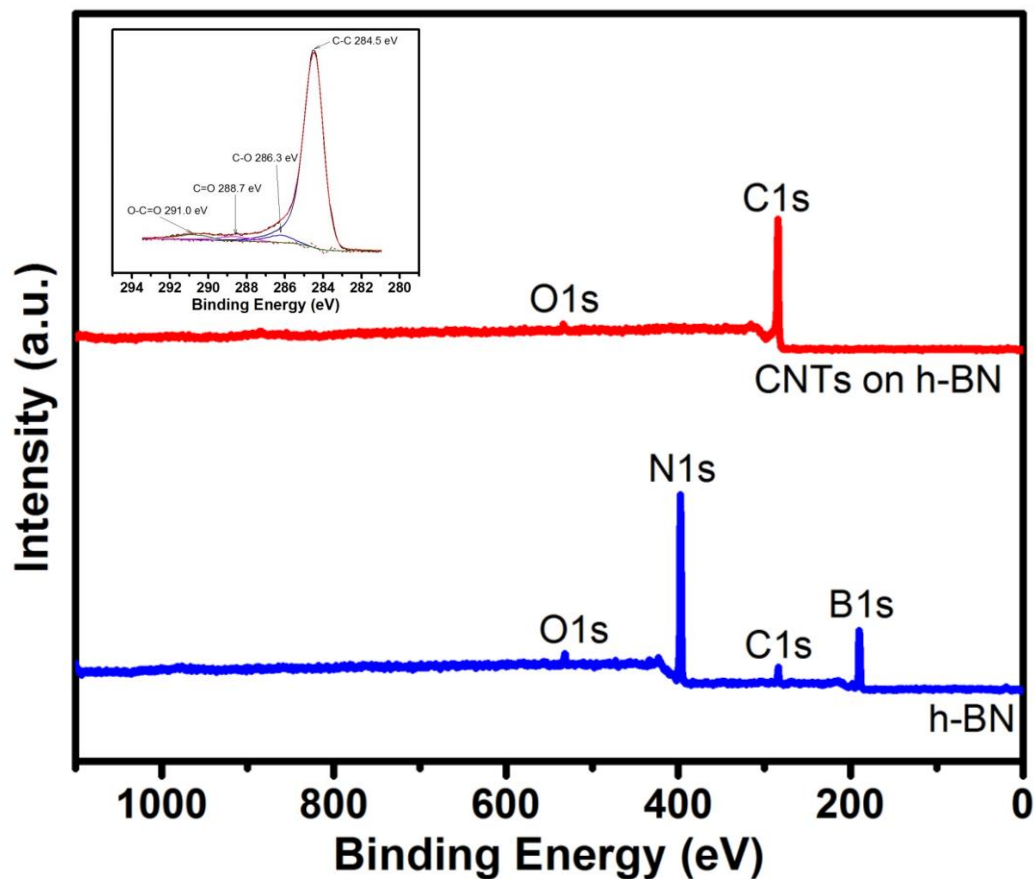
Figure 3.12 – XPS pattern of CNTs on h-BN sample. The red line shows the pattern of CNTs on h-BN (After CNT growth). The blue line shows the pattern of h-BN (Before CNT growth). The inset shows a detail scan of the C1s peak for CNTs on h-BN sampe.

3.3.5. Electrochemical Testing

The electrochemical performance of CNTs on rGO and h-BN samples for supercapacitors was measured using a polypyrrole (PPy) electrode. In order to evaluate the performance, 4 types of electrodes--rGO-PPy, CNTs on rGO-PPy, h-BN on rGO and CNTs on h-BN-PPy--were prepared. Two electrodes for a two-electrodes design were made for each type and aqueous 1 mol/L potassium chloride (KCl) was used as the electrolyte (Figure 3.13). Each basic material was electrodeposited on carbon fiber paper (Spectracarb 2050A-1050, Engineered Fibers Technology- Fuell Cell Store with electrical resistivity (through plane) of 18 mΩcm^2 and (in-plane) of 5.4 mΩcm) in the presence of a pyrrole (Py) monomer (Sigma Aldrich, reagent grade 98%) previously purified by distillation. Approximately 10 mg of each material was mixed with 0.1 mol/L of Py and 0.1 mol/L of sodium para toluene sulfonate (NaPTS, Sigma Aldrich) in 20 mL of DI water and was sonicated for 2 hours at room temperature. The electrodeposition of the composites was carried out during 30 minutes by the application of +0.8 V by the chronoamperometric method. The reference electrode was Ag/AgCl and the counter electrode was a platinum wire.
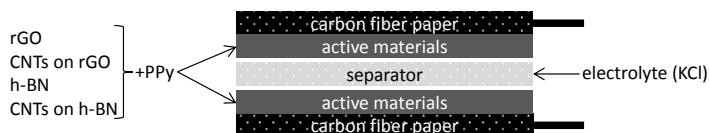
Figure 3.13 – The schematic of the two electrode setup. The electrolyte (KCl) was soaked into the separator between the two of electrodes with active materials (basic material with PPy) electrodeposited on carbon fiber paper.

Figure 3.14a shows the CV results whose scan rate was 30 mV/s. For both rGO and h-BN sample, with CNTs samples performed better than without CNTs samples. However, CNTs on rGO-PPy sample performed almost 3 times greater than the rGO-PPy sample. Figure 3.14b shows the specific capacitance of the samples. The specific capacitance values were calculated by Equation 3.1 where *I* is the average current, *m* is the mass of the active material of an electrode and *dV/dt* is the scan rate expressed as;

$$C_{esp} = 2 \cdot \frac{I}{m \cdot \frac{dV}{dt}}$$

Equation 3.1 – specific capacitance

This figure also shows that with CNTs samples performed better than without CNTs samples. The specific capacitance of CNTs on rGO-PPy sample reached 148.9 F/g at the scan rate of 5 mV/s, and CNTs on h-BN-PPy sample reached 91.5 F/g at 5 mV/s. Figure 3.14c shows the Nyquist plots for the samples of CNTs on rGO-PPy and rGO-PPy, and Figure 3.14d is the Nyquist plots for CNTs on h-BN-PPy and h-BN-PPy. For high frequencies, the insets of each figure show semicircle profile for all samples, which indicates low resistance. For intermediate frequencies with a slope of 45° related to diffusion process due to the porosity of the electrodes surface, the insets of each figure show straight lines for all samples. For low frequencies with a slope close to 90°, the insets of each figure also show straight lines for all samples. Over all,

these Nyquist plots figures show interconnected CNTs improved the electrical conductivity, and also the straight lines of low and intermediate frequencies display a good capacitor behavior. Figure 3.15a shows the galvanostatic charge and discharge curves. All of the samples performed symmetric and triangular shape during several charge and discharge cycles. Figure 3.15b shows specific capacitance based on current density which was calculated by Equation 3.1 where I is the average current and dV/dt is the slope of the discharge curve after the IR drop expressed as Equation 3.2;

$$\frac{dV}{dt} = \frac{V_{max2} - \frac{1}{2}V_{max1}}{t_2 - t_1}$$

Equation 3.2 – the slope of the discharge curve after the IR drop

Like the result of specific capacitance based on scan rate (Figure 3.14b), CNTs on rGO-PPy sample performed the best having a specific capacitance of 85.2 F/g at a current density of 0.5 A/g. Figure 3.15c shows the long-term cycling stability verified by charge and discharge methods at 1 A/g current density. Even after 1,000 cycles, all of the samples can maintain their specific capacitance stably.
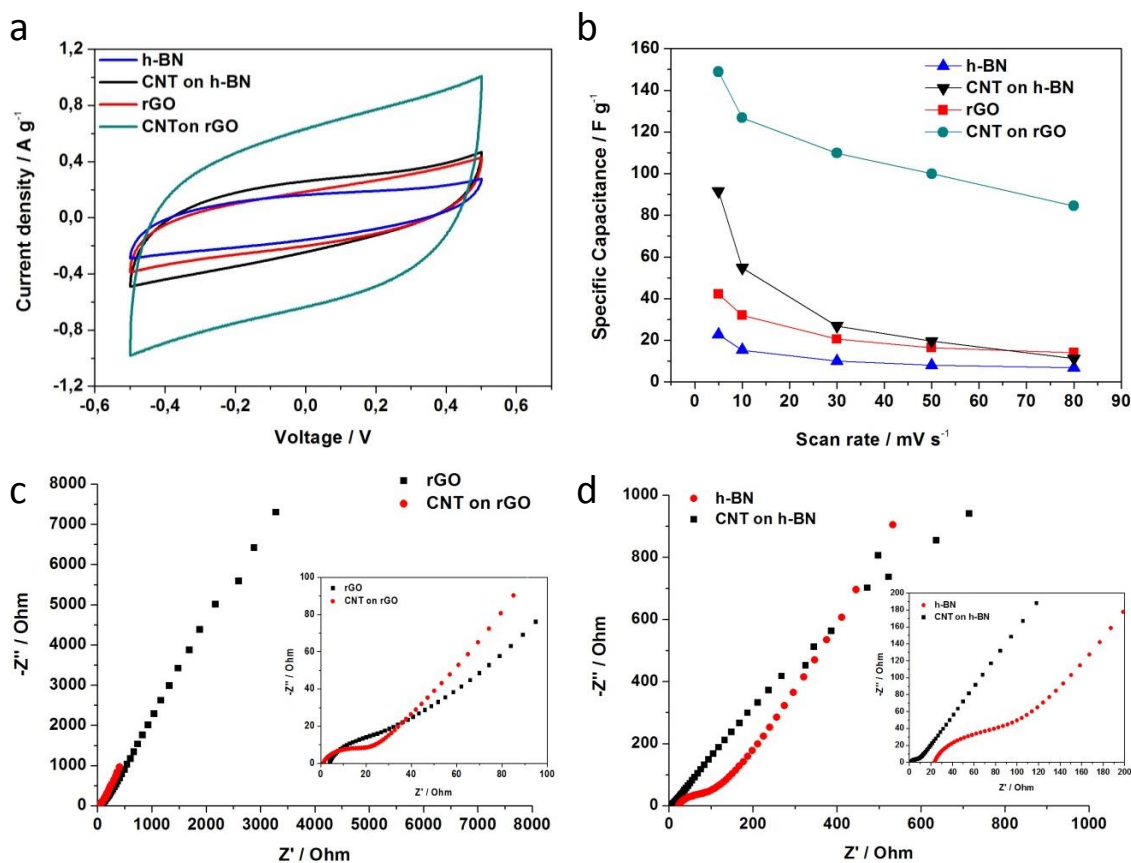
Figure 3.14 – The results of electrochemical testing. a) The comparison of CV results at scan rate 30 mV/s. CNTs on rGO-PPy sample performed the best of all. b) The specific capacitance of each sample. CNTs on rGO-PPy sample reached 148.9 F/g at the scan rate of 5 mV/s. c,d) The Nyquist plots for the samples CNTs on rGO-PPy and rGO-PPy (c), and for CNTs on h-BN-PPy and h-BN-PPy (d). Each of Nyquist plot shows interconnected CNTs improved the electrical conductivity.
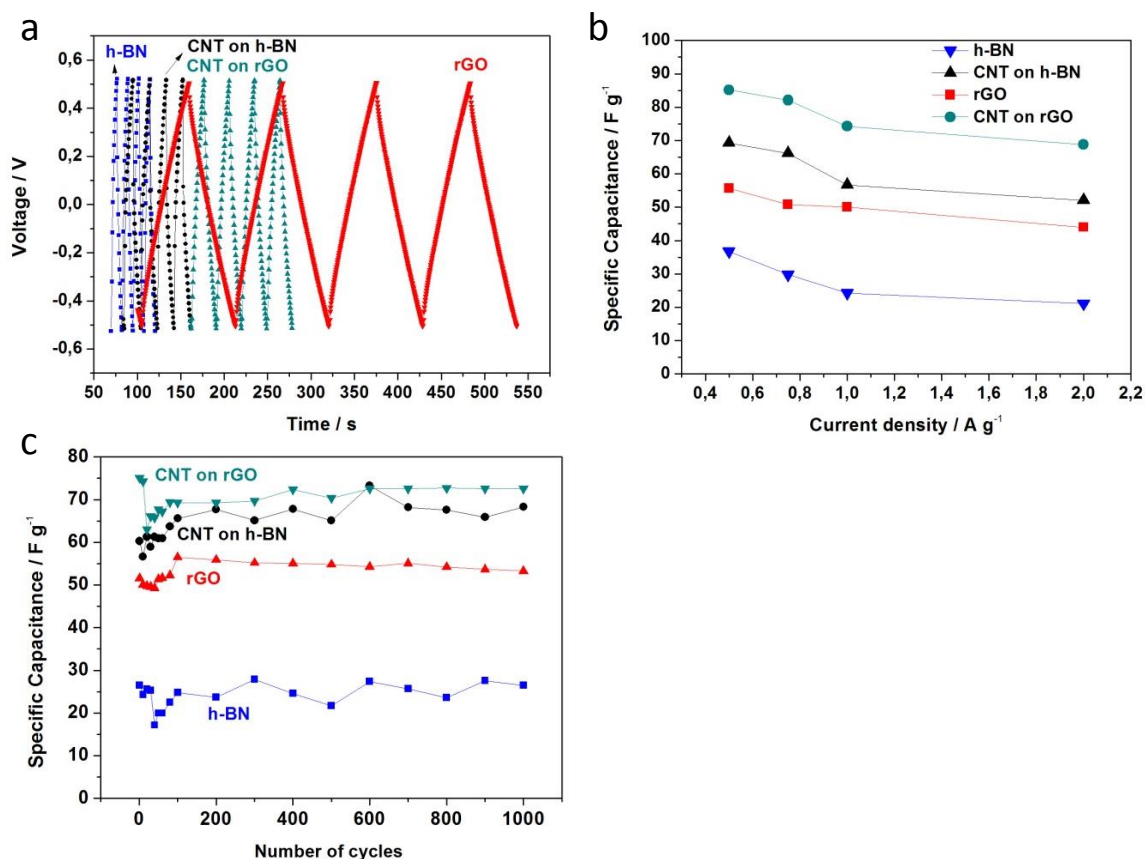
Figure 3.15 – The results of electrochemical testing. a) The galvanostatic charge and discharge curves of each sample. All of the samples performed symmetric and triangular shape stably. b) The specific capacitance based on current density of each sample. CNTs on rGO-PPy sample performed the best which is 85.2 F/g at current density of 0.5 A/g. c) The long-term cycling stability verified by charge and discharge method at 1 A/g.

Comparing all 4 samples, CNTs on rGO-PPy sample performed the best as an electrode for a supercapacitor. CNTs on h-BN-PPy sample performed the second best. Therefore, interconnected CNTs can play a significant role for increasing the

capacitance. Since h-BN is not a conductive material, rGO containing samples have superior ability supercapacitor. Moreover, each sample can maintain its specific capacitance stably even after 1,000 cycles.

Figure 3.16 shows the schematic images of electrodes and electrolyte ions. Figure 3.16a shows the image for 2D materials only while Figure 3.16b shows the image for CNTs on 2D materials. As the ions stay close to the all surfaces, CNTs on 2D materials perform well due to larger surface areas. Figure 3.17 shows SEM images of the electrodes after cycling tests. Figure 3.17a shows that the rGO-PPy electrode that contained the PPy particles retained the structure. Figure 3.17b shows the CNTs on rGO-PPy electrode that contained the PPy particles almost retained the structure while small cracks can be seen. Figure 3.17c shows the h-BN-PPy electrode that the PPy particles almost retained the structure while small cracks can be seen as well. Figure 3.17d shows the CNTs on h-BN-PPy electrode that the PPy particles almost retained the structure whereas the electrode structure was damaged.
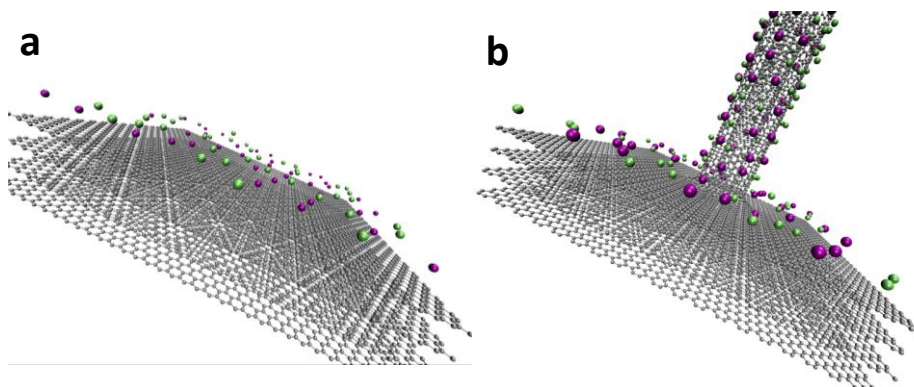
Figure 3.16 – Schematic images of electrode and electrolyte. a) For 2D materials, b) For CNTs on 2D materials.
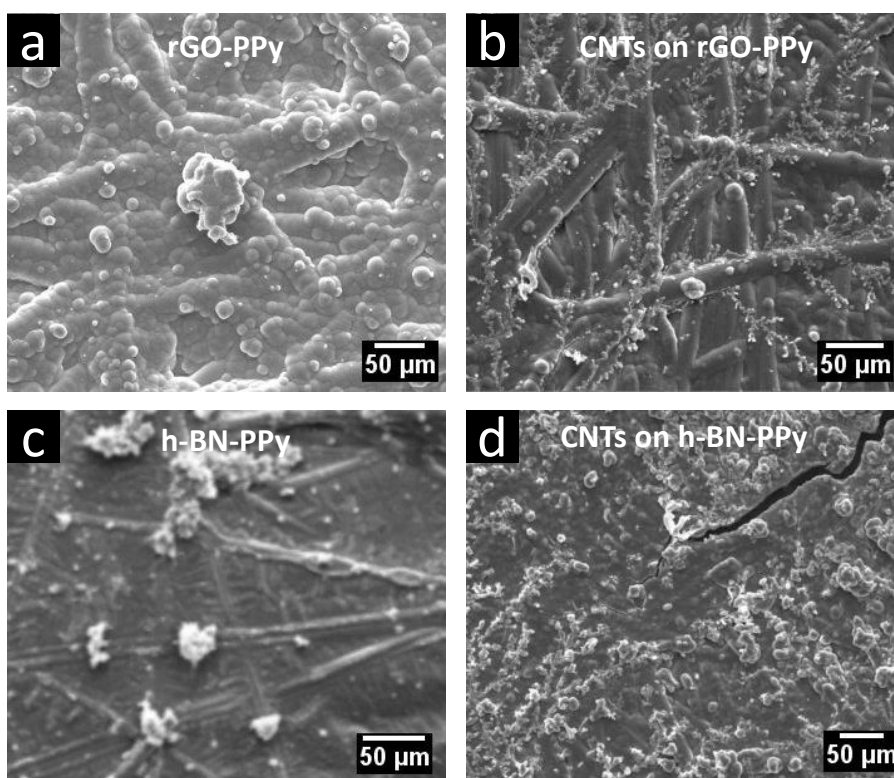
Figure 3.17 – SEM images of the electrodes after cycling tests. a) rGO-PPy, b) CNTs on rGO-PPy, c) h-BN-PPy, d) CNTs on h-BN-PPy.

3.4. Summary

This chapter is focused on the interconnection of CNTs and 2D materials namely, rGO and h-BN. In order to obtain interconnected CNTs, CVD methods were used to synthesize CNTs on 2D materials. Although there are many kinds of ways of synthesizing CNTs on graphene related materials, the feature of this method is the simultaneous synthesis of CNTs and reduction of GO. Moreover, while there are few reports about CNT synthesis on h-BN, one synthetic method was proposed in this chapter. By SEM and TEM images, both CNTs on rGO and CNTs on h-BN samples were confirmed that CNTs and rGO or h-BN can be chemically interconnected.

For CNTs on rGO sample, the synthetic method in this chapter shows that CNTs can be grown without any further catalysts or templates despite many methods for CNTs, graphene, or rGO hybrid materials which are connected chemically require catalysts. Among some methods for CNTs and graphene or rGO hybrid materials synthesize CNTs directly on graphene or rGO surface, this chapter's method puts emphasis on synthesizing CNTs from the surface of GO. The merit of this method is that it is possible for some kinds of functional groups on GO might work well to initiate CNT growth, but GO would be reduced to rGO after CNT growth procedure. The challenges of this chapter's method are; 1) it is hard to retain rGO (GO) entirely on a nickel foam because some parts of rGO (GO) have gone after CNT growth procedure, 2) the CNTs on rGO is not aligned or straight but grown randomly. When these CNTs on rGO sample is applied for a mechanical damper or

an electrical supercapacitor, straight and aligned CNTs on rGO might behave better performance due to its stronger structure and larger surface area.

For CNTs on h-BN sample, the characteristic of the synthetic method in this chapter is CNTs can be grown on h-BN surface. Since the structure of h-BN is similar to graphene's, some material properties of h-BN are closed to graphene's. There are few reports about CNTs and h-BN hybrid structures whereas there are many reports about boron nitride nanotubes. Although CNTs can be grown on the surface of h-BN and the two materials were connected chemically, the inside structure of the CNTs were not a hollow tube but filled. Since there are boron, carbon, nitrogen, aluminum, iron and nickel atoms, these other atoms might be inside, filling the nanotubes. The 200 kV that the TEM uses for its operation might also cause damage to the structure of the nanotubes. The D band peak of the Raman pattern is almost same as the G band, indicating that the quality of the CNTs is not favorable. Therefore, the challenges of this chapter's method are; 1) the CNTs on h-BN were not aligned but grown randomly, and 2) it is necessary to examine the inside structure of the filled CNTs.

Since interconnected CNTs and 2D materials usually have large surface area because of their structure, these interconnected materials typically perform well as an electrode of supercapacitors. The electrochemical tests using rGO, CNTs on rGO, h-BN and CNTs on h-BN samples were carried out. CNTs on rGO sample performed favorably with respect to the specific capacitances. The electrochemical tests revealed interconnected CNTs can improve the performance as a supercapacitor.

3.5. Application and Future Work

This work has focused on the synthesis of hybridized CNTs and 2D materials. While there are a lot of attempts of these kinds of 3D structures, the connection between CNTs and 2D materials is not still clear especially for chemically bonded hybrids. As far as examining TEM figures, CNTs on rGO and h-BN were combined together for this study but it is difficult to show the bonding is of a covalent nature.

Chapter 4

Ellipse Oval Flake Interconnected Structure of Molybdenum Carbide

4.1. Overview and Motivation

Molybdenum carbide--a family of TMCs--is desirable because it may serve as an alternative to platinum, which is a scarce and expensive rare earth metal[92-99]. Molybdenum carbide has the ability for a catalyst of HER activity as well as an electrode for a supercapacitor[103,107]. There are many kinds of ways to synthesize molybdenum carbide, and it is used in a number of commercial products[179,180]. Although commercial forms of molybdenum carbide are usually powder state, other types of samples have been reported. In 2010, for instance, Cetinkaya et al. reported "porous Mo_2C sponge" synthesized from molybdenum trioxide (MoO_3) through a CVD method with thermodynamics study[181]. In 2015, Xu et al. reported ultrathin 2D molybdenum carbide crystals[182]. In 2016, Ojha et

al. published about a catalyst of HER activity consisting of "graphene-Mo_2C rods" composites, which behaves with stable HER activity and 59 mV of onset over potential[183]. Also in 2016, Valk et al. reported electrochemical performance of "partially chlorinated molybdenum carbide composites", with a maximum of 140 F/g with up to 2,020 m^2/g of SSA[184].

This chapter discusses a new synthetic method to produce molybdenum carbide which is suitable for mass production and its application. By the new method of its synthesis, oval or hexagonal molybdenum carbide flakes which are interconnected with each other and form chains with several flakes have been developed. This method uses a CVD method for molybdenum carbide growth. Molybdenum trioxide is used as a molybdenum source, and xylene is used as a carbon source. The CVD method allows obtaining 20 mg of sample at one procedure tops. The sample right after the growth procedure was in a sponge state, and the several molybdenum carbide flakes retained the interconnection even after 30 minutes of sonication dispersed in IPA. The intriguing flake structures performed well for a catalyst of HER activity and an electrode of a supercapacitor.

4.2. Synthesis of the Molybdenum Carbide

The setup of molybdenum carbide synthesis is similar to CNTs on h-BN procedure. There was a CVD setup with liquid injection. The carbon source was xylene, and the molybdenum source was molybdenum trioxide powder (Sigma-Aldrich, 267856, Molybdenum (VI) oxide, ACS reagent, ≥99.5%). Figure 4.1 shows schematic figure of synthetic procedure of the molybdenum carbide. The growth

temperature was 790°C, and the growth time was 1.5 hours. The substrate was silicon wafer deposited aluminum (10 nm) and iron (1.5 nm). Before the synthetic process, the glass tube was burned clean. The amount of molybdenum carbide produced was usually low after the first cleaning. However, after the first growth, the molybdenum carbide sample can be found not only on silicon wafer but also inside the glass tube. The sample's structure was that of a sponge (Figure 4.2, Figure 4.3).
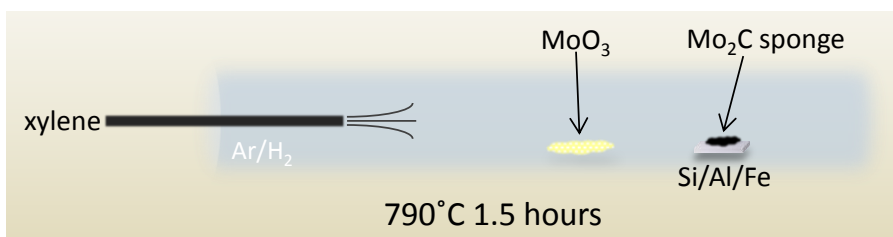
Figure 4.1 – Schematic figure of Mo$_2$C synthetic procedure. Liquid xylene was injected with 15 % hydrogen balanced argon gas to the glass tube. Mo$_2$C sponge was formed from xylene and MoO$_3$.

Figure 4.2 – The optical image of the Mo$_2$C sample on a substrate (the right hole). The Mo$_2$C covered the substrate and the side of seramic boat.

Figure 4.3 – The optical image of the Mo$_2$C sponge.

4.3. Results and Discussion

4.3.1. Characterization by Electron Microscopy

The characterization by electron microscopies were carried out by FEI Quanta 400 SEM at accelerating voltage of 20 kV and JEOL 2100 field emission gun TEM at operating at 200 kV. Figure 4.4 shows SEM images of molybdenum carbide sponge samples. Figure 4.4A shows an overview of molybdenum carbide sponge, and Figure 4.4B shows a magnified image. Molybdenum carbide sponge samples consist of interconnected oval shape pieces. Figure 4.4C-F show the figures that the sample was dispersed in IPA and sonicated 30 minutes. After sonication, the oval shape pieces retained their interconnection. Figure 4.4D-F show magnified images of the oval shape pieces, and the images reveal the interconnection among the pieces forms randomly. The size of the oval shape pieces varies around 500 nm to a

few μm. Each piece of the oval shape looks like a "Koban," which is a Japanese traditional coin.

Figure 4.5 shows TEM images of molybdenum carbide sponge samples. Figure 4.5A-D are low magnification TEM images, and they show interconnected oval shape pieces like Figure 4.4D-F. These flake structures look like the shape of "nano animals." Figure 4.5A looks like a "fox," Figure 4.5B looks like a "butterfly," Figure 4.5C looks like a "rabbit," and Figure 4.5D looks like a "hummingbird." Figure 4.5E is a high magnification TEM image, and it reveals molybdenum carbide layer and amorphous carbon layer on the surface of the oval shape piece. Figure 4.5F is also a high magnification TEM image, and it shows there are some amorphous carbon areas (blacken parts) on the surface of the oval shape piece. Therefore, high magnification TEM images reveal the oval shape piece consists of not only molybdenum carbide but also amorphous carbon.

Since the synthesis temperature was 790℃ which is less than 1,400℃ (the crystal structure's transformation temperature), the crystal structure of the molybdenum carbide sample can be estimated as alpha phase molybdenum carbide (α-Mo_2C)[109]. Figure 4.6 shows an electron diffraction image of molybdenum carbide sample. The zone axis of the image was estimated as [01-2], and some of molybdenum carbide peaks were indexed as alpha phase molybdenum carbide[108-110]. Since the molybdenum carbide sample contained amorphous carbon, the peaks or rings related to amorphous carbon showed up.
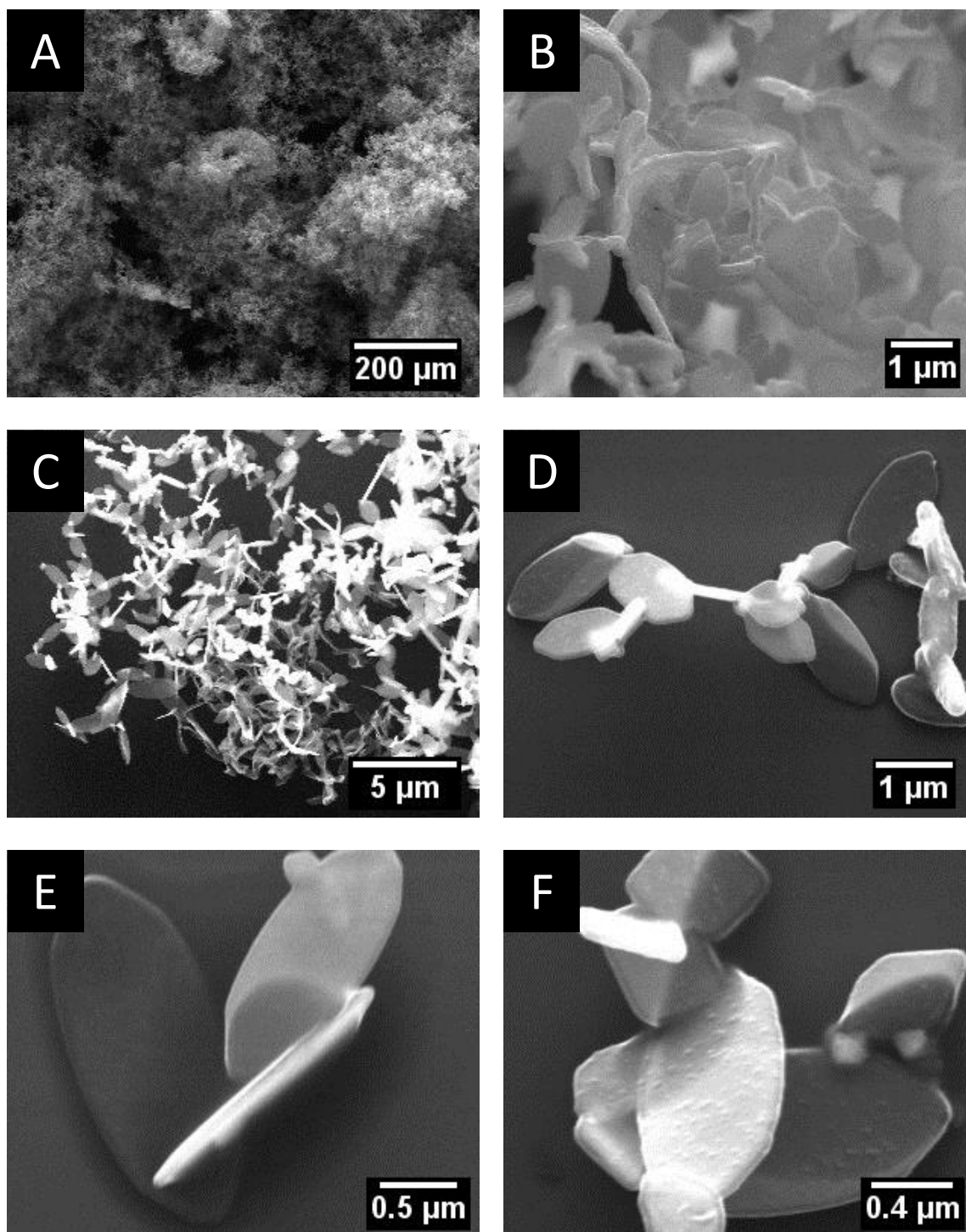
Figure 4.4 – SEM images of Mo$_2$C sample. A-C) Magnified images of Mo$_2$C
sponge. D-F) High magnification images of interconnected Mo$_2$C flake "Koban."

Fox: Image courtesy of Serge Bertasius Photography at FreeDigitalPhotos.net

Butterfly: Image courtesy of panuruangjan at FreeDigitalPhotos.net

Rabbit: Image courtesy of dan at FreeDigitalPhotos.net

Hummingbird: Image courtesy of Gualberto107 at FreeDigitalPhotos.net
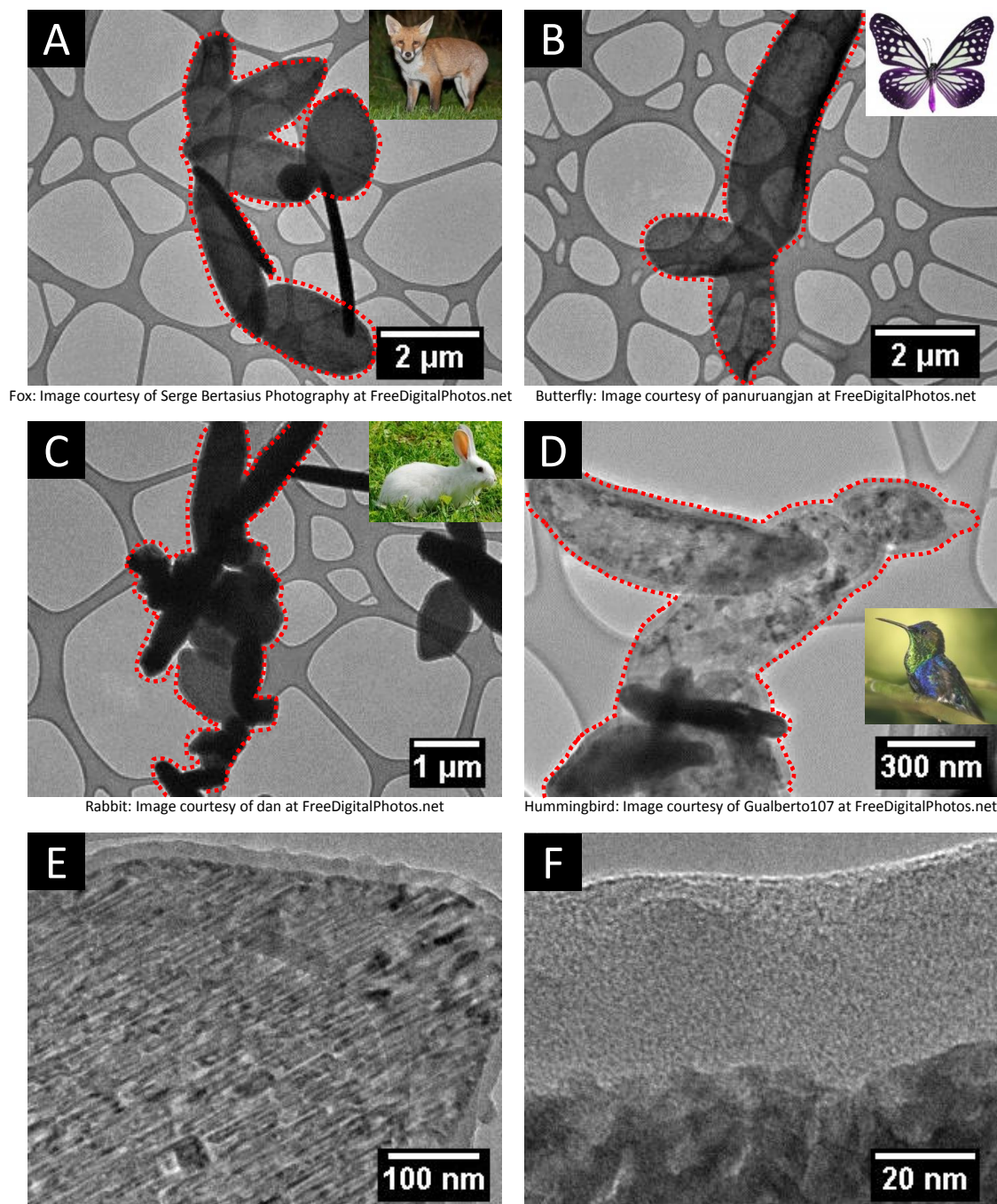
Figure 4.5 – TEM images of Mo$_2$C sample. A-D) Low magnification images of "animal" like Mo2C sample, a "fox" (A), a "butterfly" (B), a "rabbit" (C), and a "hummingbird" (D). E-F) High magnification images of Mo$_2$C flake "Koban."
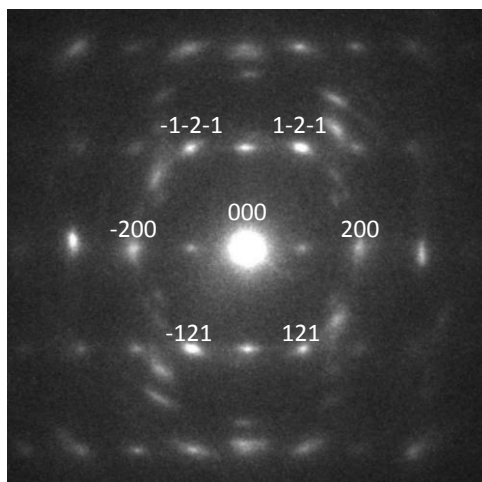
Figure 4.6 – Electron diffraction image of Mo$_2$C sample (Zone axis: [01-2]).

4.3.2. Characterization by Raman Microscopy and FTIR Spectroscopy

Raman spectrum of the samples was carried out by RENISHAW inVia Raman Microscope using a 514 nm laser. FTIR pattern was measured using Thermo Fisher Scientific Model: Nicolet iS50. Figure 4.7a shows the Raman spectrum of the molybdenum carbide sponge sample. It shows D band and G band relating it to amorphous carbon[163]; therefore, the Raman measurement also reveals the existence of amorphous carbon on the flake. Figure 4.7b is a FTIR pattern of the molybdenum carbide sample. According to literatures, FTIR of metal-carbon stretching vibration peak appears around 450-520 cm^{-1}[185,186]. The inset of Figure 4.7b is the magnification between 450 and 520 cm^{-1}, and it shows several peaks which might be related to the metal-carbon stretching vibration peak.
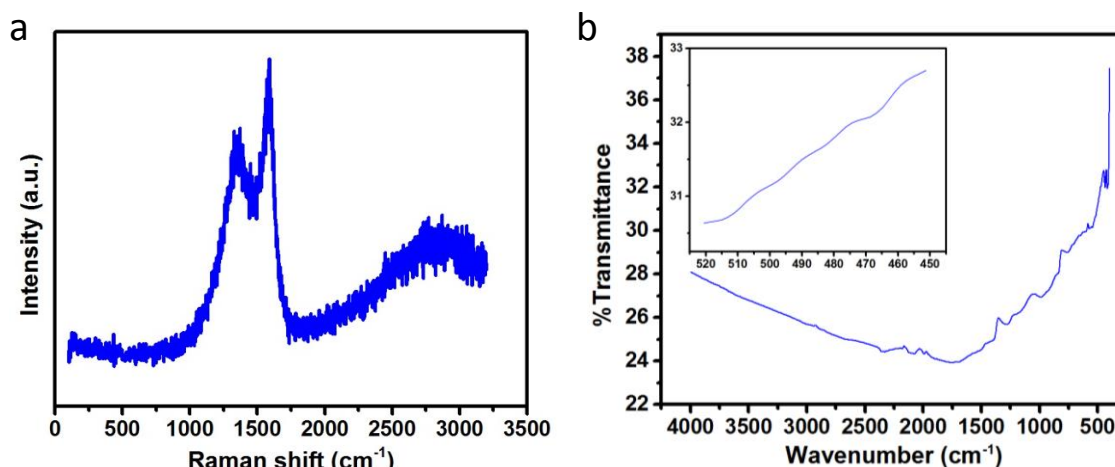
Figure 4.7 – a) Raman spectrum of Mo$_2$C samples. b) FTIR spectrum of Mo$_2$C

samples. The inset shows the magnification between 450 and 520 cm^{-1}.

4.3.3. Characterization by XRD

XRD pattern was measured by Rigaku D/Max Ultima II Powder XRD using a CuKα x-ray tube. Figure 4.8 shows a XRD pattern of molybdenum carbide sample, and it reveals typical molybdenum carbide peaks. The red squares on the graph show reference peaks of α-Mo$_2$C[108-110]. There is a wide peak around 25° but the reference does not have any peaks at that angle. The peak appears to be amorphous carbon because the peak corresponding to carbon is very wide. However, the measured data and the reference data are very close to both in terms of relative intensity and peak positions between 30° and 90°. Therefore, XRD result shows the sample mainly consists of as α-Mo$_2$C and also contains amorphous carbon.
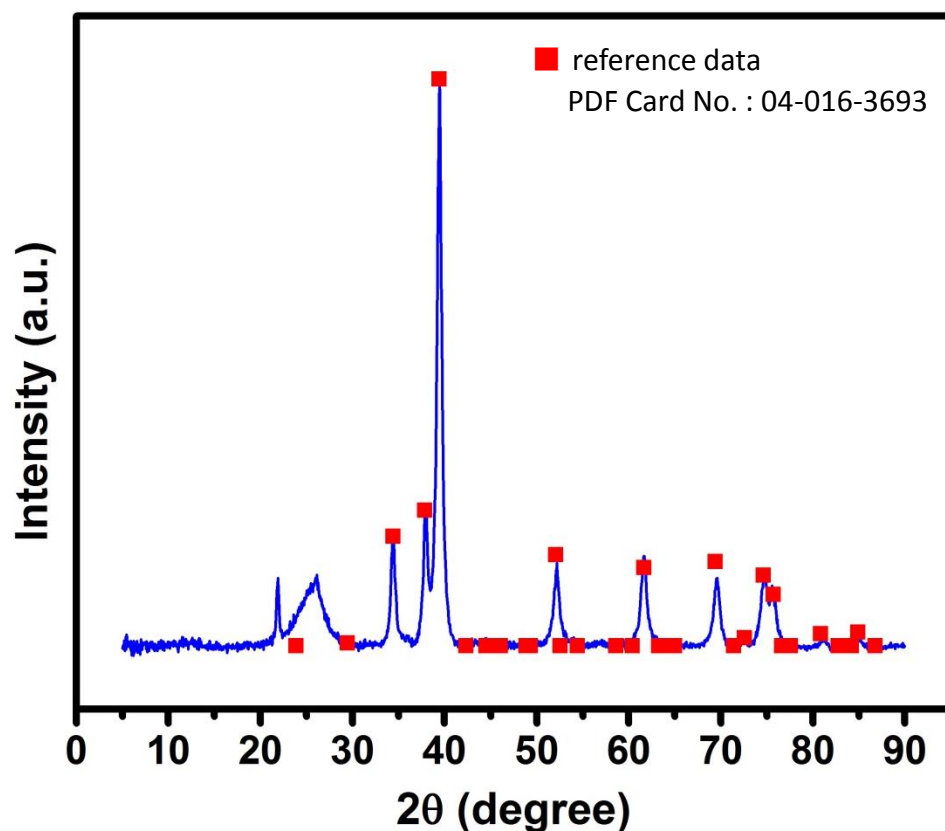
Figure 4.8 – XRD pattern of Mo$_2$C sample. The measured line (blue line) and the reference squares (red) are really close to each other between 30° and 90°[108-110].

4.3.4. Characterization by XPS

XPS data was examined by PHI Quantera XPS using an AlKα x-ray tube. Figure 4.9 shows XPS survey scan for molybdenum carbide sample, and it shows mainly carbon 1s peak. Although there is molybdenum 3d peak, the intensity of molybdenum 3d peak is very weak. The inset of Figure 4.9 is detail scan result of molybdenum 3d peak, and it shows the existence of molybdenum. Figure 4.9 reveals

the surface of the oval shape piece was coated by amorphous carbon, which was found using XPS to measure the sample surface area.
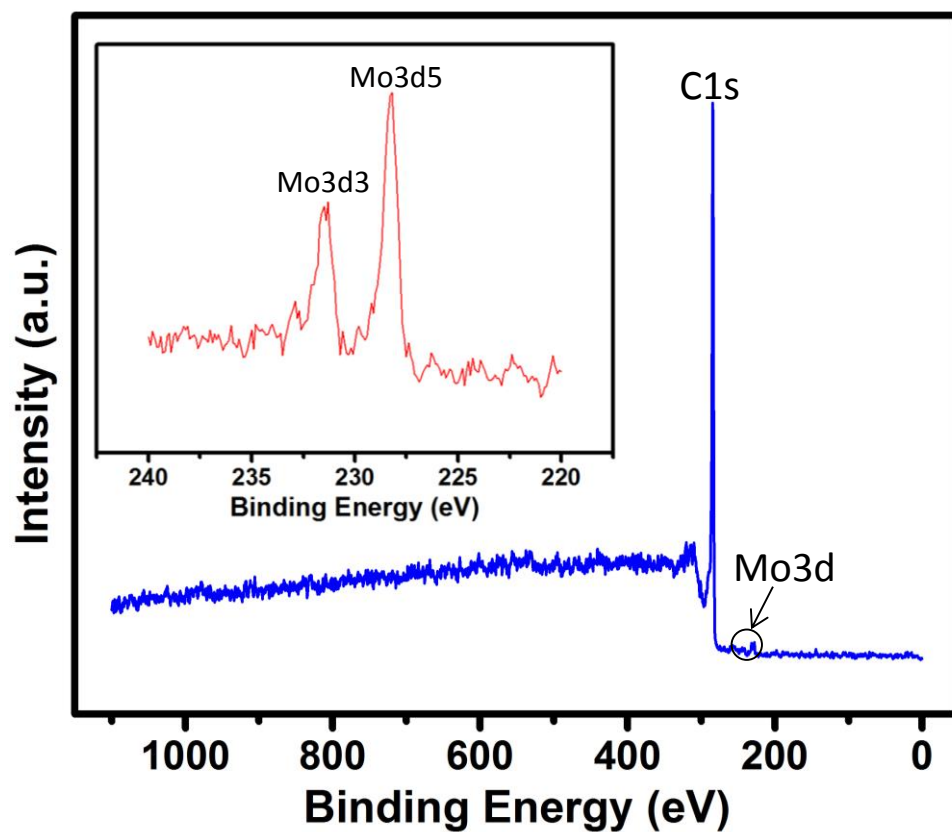
Figure 4.9 – XPS pattern of Mo₂C sample. C1s has a large peak while Mo3d has a little peak. The inset shows the detail scan of Mo3d peak.

4.3.5. Characterization by TGA

TGA was carried out by TA Instruments' Q-600 in air (the flow rate of 100 mL/min) and argon gas atmosphere (the flow rate of 45 mL/min). TGA results show the molybdenum carbide sample burned out around 600°C in air whereas it retained

more than 88 % of its weight at 900°C in argon gas condition. Although the melting temperature of molybdenum carbide is more than 1,000°C, it burned out around 600°C in air[102]. However, the weight of the molybdenum carbide sample did not change drastically in argon gas condition even though the weight reduced to approximately 88 % at 900°C. As TEM images show, some parts of molybdenum carbide samples were covered by amorphous carbon. Therefore, the initial weight reduction (less than 600°C) might be evaporation of amorphous carbon.
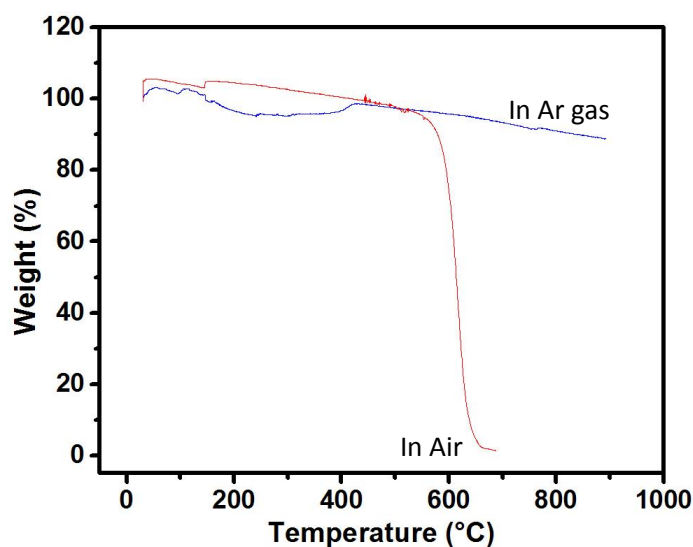
Figure 4.10 – TGA result of the Mo₂C sample. The weight of the Mo₂C sample remained more than 88 % in argon gas while it burned out at around 600°C in air.

4.3.6. Characterization of SSA

The SSA of molybdenum carbide sample was measured by the surface analyzer (Quantachrome Autosorb-3b) based on BET's equation (Equation 2.1). Nitrogen gas was used for this measurement. Figure 4.11 shows the plots of the measurement and its trend line whose R^2 is 0.0129. Although the slop of the trend line is negative value and R^2 value is quite low, the SSA of the molybdenum carbide sponge was calculated as approximately 298 m^2/g.

y = -7.7625x + 19.44
R^2 = 0.0129
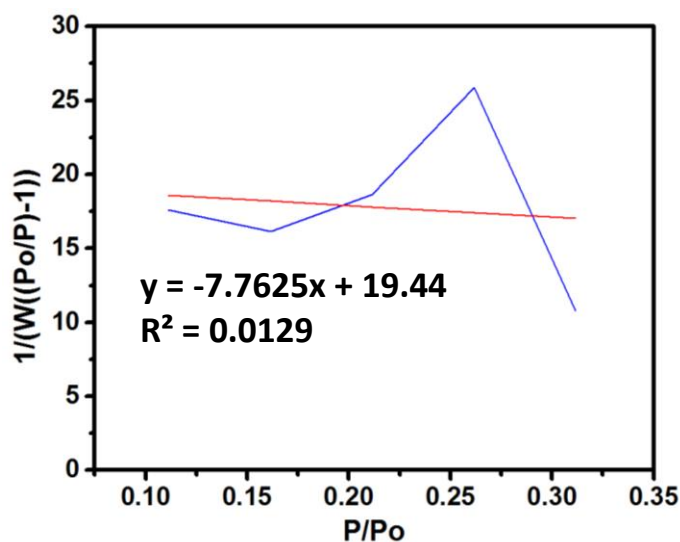
Figure 4.11 – The plots of SSA measurement of the Mo₂C and its trend line whose R^2 is 0.0129.

4.3.7. In-situ Mechanical Testing

The mechanical behavior of the molybdenum carbide was tested by quasi-static uniaxial compression loading inside an SEM using an SEM PicoIndenter, xrPI85 (Hysitron, Inc., USA). The micro-indenting in-situ mechanical tests showed the stiffness and elastic modulus of the molybdenum carbide sponge. A piece of the sponge remained almost half deformed after loading and unloading compression tests (a deformation of 10 % strain). Figure 4.12a shows the load displacement curve of a sponge shows 40–50 % deformation after the loading, and Figure 4.12b shows the SEM figure during the test. The load-displacement curves also exhibit a small hysteresis loop in cyclic loading resulting in 8 GPa elastic modulus. In addition, the tip of the chains consisting of molybdenum carbide flakes was compressed using a smaller indentor. Figure 4.12c shows the loading-unloading curves which also recovered almost original shape with low hysteresis, and Figure 4.12d shows the SEM figure during the test. The elastic modulus resulted 15 GPa.
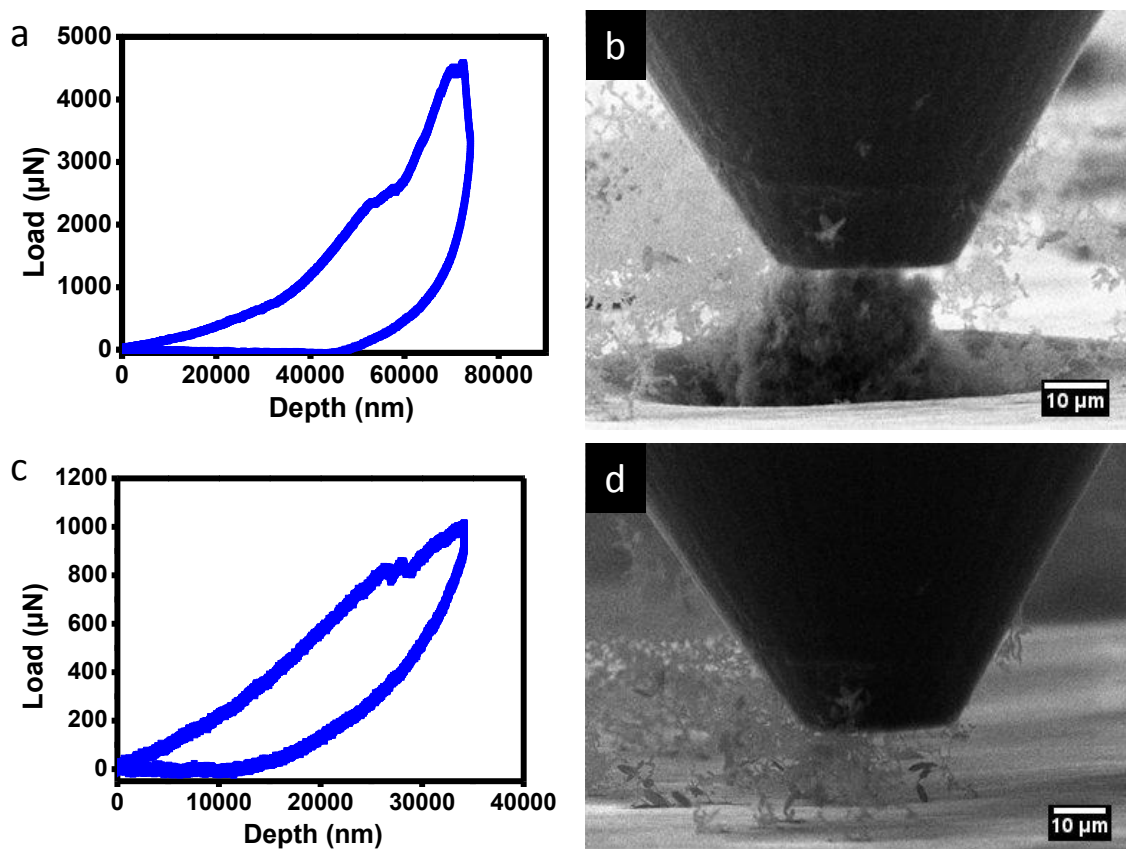
Figure 4.12 – In-situ mechanical testing for the Mo₂C sponge. a) The load and unload curve for a piece of Mo₂C sponge. Almost half of deformation occured after compression. b) The SEM image for the test (a). c) The load and unload curve for a tip of Mo₂C sponge. This result shows almost elastic performance. d) The SEM image fot the test (c)

4.3.8. Electrochemical Testing

The electrochemical performance of the molybdenum carbide sample was studied as an active material for application in supercapacitor devices. In order to evaluate the performance, the composite based on Mo_2C and PPy was prepared the same way of CNTs on rGO and h-BN samples. The two-electrodes supercapacitor design was constructed using aqueous 1 mol/L KCl as the electrolyte (Figure 3.13). The molybdenum carbide was electrodeposited in the presence of Py monomer (Sigma Aldrich, reagent grade 98%) previously purified by distillation on carbon fiber paper (Spectracarb 2050A-1050, Engineered Fibers Technology- Fuell Cell Store with electrical resistivity (through plane) of 18 $m\Omega cm^2$ and (in-plane) of 5.4 $m\Omega cm$). The solution was consisted of 1 mg/mL molybdenum carbide sample that was mixed with 0.1 mol/L of Py and 0.1 mol/L of sodium para toluene sulfonate (NaPTS, Sigma Aldrich) in DI water and was sonicated for 2 hours at room temperature. The electrodeposition of the composite was carried out during 30 minutes by application of +0.8 V by chronoamperometric method. The reference electrode was Ag/AgCl and the counter electrode was a platinum wire. The pure PPy electrode was tested for comparison and it was prepared as the same way without the presence of Mo_2C.

Figure 4.13a shows the CV results comparing with the electrode without molybdenum carbide sponge (pure PPy) and the electrode with the molybdenum carbide (PPy-Mo_2C) whose scan rate was 30 mV/s. The PPy/Mo_2C performed almost 5 times greater than pure PPy. Figure 4.13b shows specific capacitance of the samples, which was calculated by Equation 3.1 where *I* is the average current, *m* is

the mass of the active material of an electrode and dV/dt is the scan rate. This figure also shows PPy-Mo$_2$C performed better than PPy. The specific capacitance of PPy-Mo$_2$C reached 191.3 F/g at the scan rate of 5 mV/s, and PPy reached 41.9 F/g at the same scan rate. Figure 4.13c is the Nyquist plots for the samples. The resistance was found through the intersection of the semicircle in x-axis in high frequencies and represents the electrode material-electrolyte interface resistance. These curves showed very low values for both samples indicating high conductivity; however, the composite showed a lower charge transfer resistance than pure PPy. For intermediate frequencies, a straight line with a slope of 45° related to diffusion process due to the porosity of the electrodes surface was observed. For low frequencies the straight line with a slope close to 90° was observed and this means a good capacitive behavior. Over all, these Nyquist plots shows molybdenum carbide improved the electrical conductivity. Figure 4.13d shows the galvanostatic charge and discharge curves. Both samples performed symmetric and triangular shape stably during the charge and discharge cycles. Figure 4.13e shows specific capacitance based on charge/discharge curves which was calculated by Equation 3.1 where I is the average current and dV/dt is the slope of the discharge curve after the IR drop expressed as Equation 3.2. PPy-Mo$_2$C sample performed as 278.5 F/g at current density of 0.5 A/g which was almost 8 times higher than pure PPy. Figure 4.13f shows the long-term cycling stability verified by charge and discharge method at 1 A/g current density. After the 1,000 cycles, the specific capacity decreased about 60 F/g.
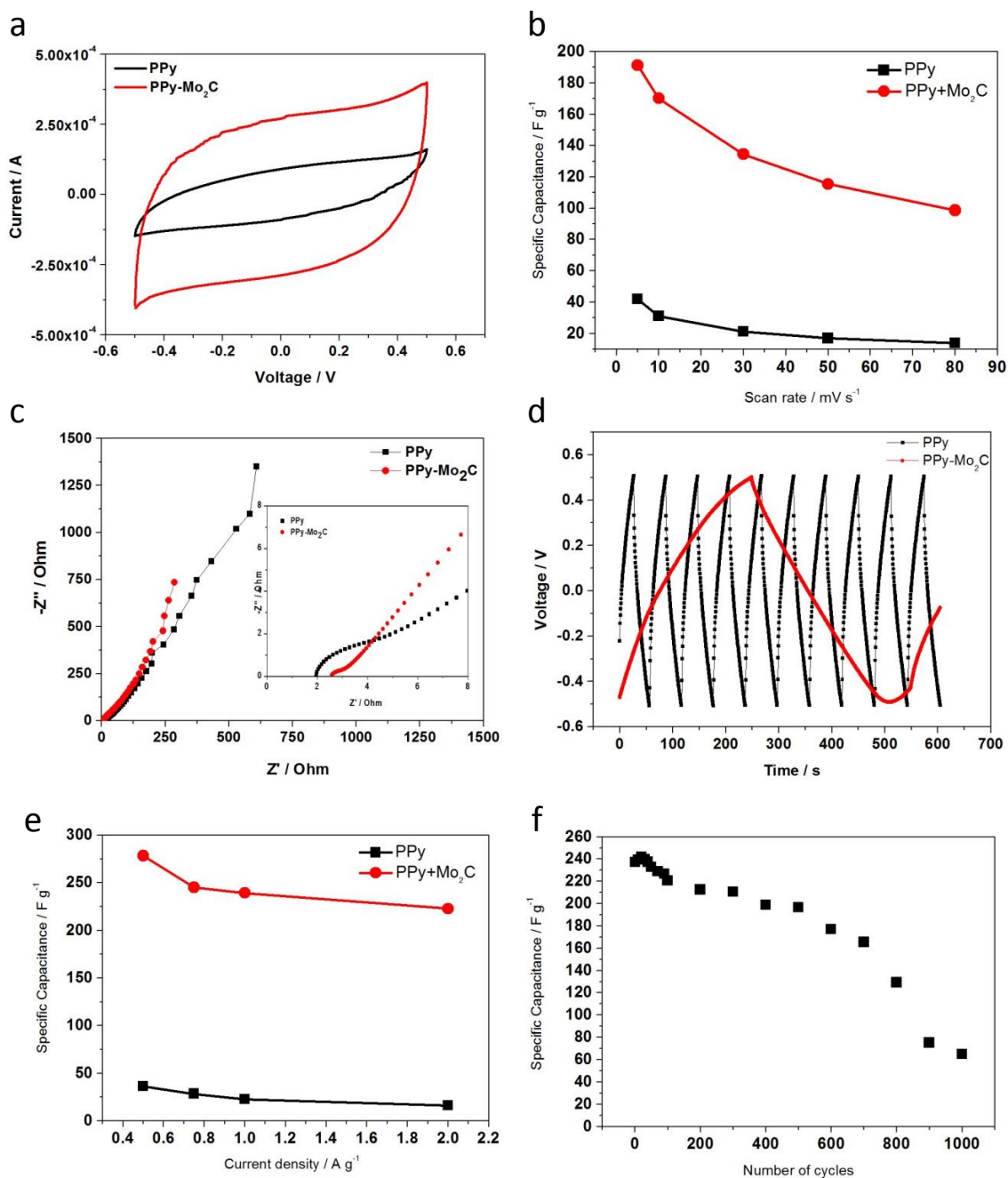
Figure 4.13 – Electrochemical measurement for the Mo₂C sample.

4.3.9. HER Catalyst Testing

HER activity of the molybdenum carbide samples was measured by at a standard three-electrode electrochemical cell setup (Figure 4.14)[187]. In order to evaluate the performance, 3 μL of the molybdenum carbide with 0.5% nafion solution was used as the working electrode. The reference electrode was Ag/AgCl and the counter electrode was a platinum wire. The electrolyte for this test was 0.5 M sulfuric acid (H_2SO_4). The applied potential was 0 to −0.7 V.
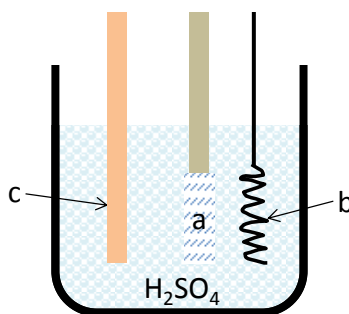
Figure 4.14 – The schematic of the three-electrode electrochemical cell setup. a) working electrode (Mo_2C with nafion), b) counter electrode (Pt), c) reference electrode (Ag/AgCl). The electrolyte is H_2SO_4.

Figure 4.15 shows linear sweep voltammogram (LSV) pattern of the molybdenum carbide electrode. The performance of the molybdenum carbide electrode became better after 5,000 cycles, and between 5,000 and 10,000 cycles the performance almost kept stable. The inset of Figure 4.15 shows the magnification of the onset over potential area. The onset over potential values, η_{onset},

of each cycle are summarized in Table 4.1. The onset over potential was determined by taking the intersection of two tangent lines (The inset of Figure 4.15). The onset over potential values of 5,000 and 10,000 cycles were -16 and -25 mV respectively. The over potential values at 10 mA/cm^2, η_{10}, are -240 mV (for 5,000 cycles) and -234 mV (10,000 cycles), and also the values at 20 mA/cm^2, η_{20}, are -282 mV (for 5,000 cycles) and -276 mV (10,000 cycles). Since the some part of surface of the molybdenum carbide samples was covered with amorphous carbon according to the TEM images, the initial cycle of HER activity might not be good compared with after 5,000 cycles. However, the amorphous carbon might be removed and the electrolyte might penetrate into the sponge after a few thousand cycles of HER activities. The surface area of the molybdenum carbide samples could be increased after a few thousand cycles of HER activities. According to the SSA measurement, the plots are not straight because the surface area might not be stable due to the amorphous carbon. Therefore, after 10,000 cycles of HER activities, the SSA might be increased though it is difficult to measure SSA after measurements of HER activities because it is hard to remove only the molybdenum carbide from the electrode.

Although the onset over potential was low, the over potential at 10 mA/cm^2 was not high performance comparing with previous work which was -182 mV[188]. There are many studies regarding HER activity, that are not single materials, but are composites, such as base materials (molybdenum disulfide), and additives (CNTs)[189]. In 2014, for example, Li et al. reported the electrode made by molybdenum sulfide (MoS$_x$) and CNTs behaved -110 mV (the over potential at 10 mA/cm^2)[190]. Many reports have shown carbon materials--such as CNTs, GO and

graphite--are typical candidates of the additives[191]. Therefore, the mixture of the

molybdenum carbide samples and these additives might behave better.
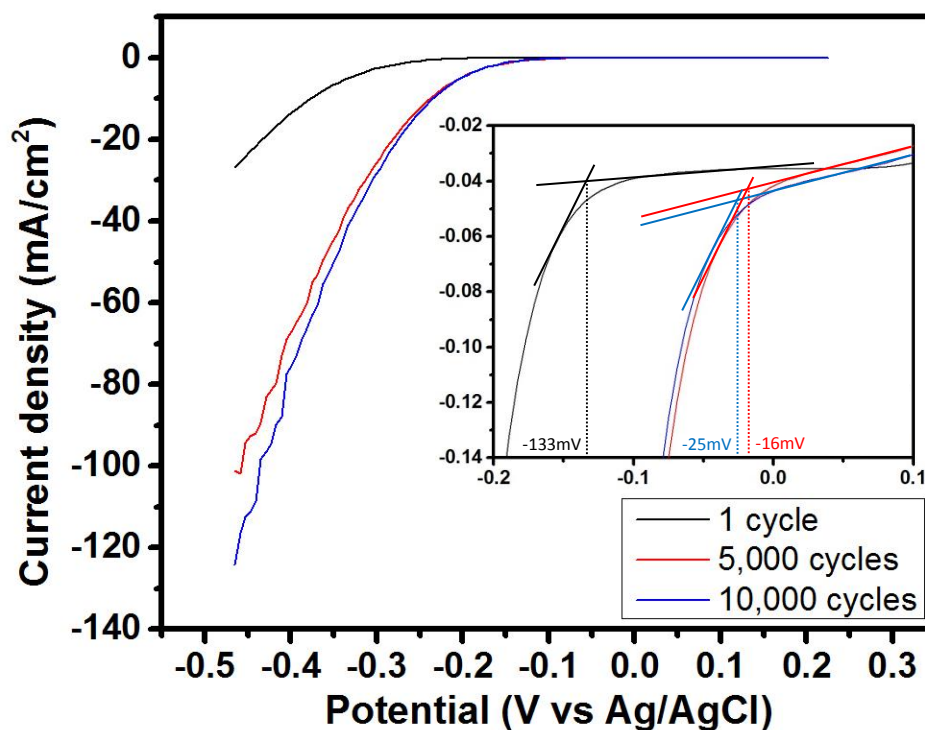
Figure 4.15 – LSV pattern of the Mo$_2$C samples for a catalyst of HER activity.

The inset shows the onset over potential.

cycles	η_{onset} (mV)	η_{10} (mV)	η_{20} (mV)
1	-133	-378	-432
5,000	-16	-240	-282
10,000	-25	-234	-276

Table 4.1 – Comparison of over potential based on cycles.

4.4. Summary

This chapter is focused on an interconnected flake structure of molybdenum carbide. The unique structure was synthesized by a CVD method using xylene as a carbon source and molybdenum trioxide as a molybdenum source. Although the molybdenum carbide formed a sponge shape when it was synthesized, the sponge structures were separated to independently interconnected chains by sonication. Each flake had an ellipse shape, and its major axis was about a few μm and its minor axis was about 1 μm. Since xylene is a carbon rich material, each flake was partially covered with amorphous carbon according to the TEM figures. The XPS measurement also suggests the existence of carbon on the surface area. The flakes interconnected with each other, and each chain had several flakes. The low magnification TEM images show these chains look like some animal shapes such as a hummingbird. Based on the growth temperature (790°C) and the XRD pattern, the crystal phase of the molybdenum carbide sponge was estimated as mainly α-Mo_2C but it was also covered with amorphous carbon.

Since molybdenum carbide is a good candidate material for an electrode of a supercapacitor and HER activity, their performance was measured using the molybdenum carbide sample. The electrode for a supercapacitor test was carried out by a PPy electrode, and the electrode containing the molybdenum carbide sponge sample performed as 278.5 F/g at current density of 0.5 A/g. This value is approximately three times greater performance comparing with CNT on rGO sample at the same condition which is 85.2 F/g. Whereas the Nyquist plots and

galvanostatic charge and discharge curves showed good behavior for an electrode, the stability got worse when the test cycles increased. The HER activity test was carried out by a typical three electrode setup. The performance of the HER activity using the molybdenum carbide electrode increased after a few thousand cycles, while the first cycle behavior was not good. The onset over potential values of 5,000 and 10,000 cycles were -16 and -25 mV respectively, and the over potential at 10 mA/cm^2 is approximately -240 mV. Because the surface of the molybdenum carbide flakes was covered with amorphous carbon, the amorphous carbon might be removed from the electrode during the tests. For the electrode for a supercapacitor test, the molybdenum carbide samples might be removed with amorphous carbon from the PPy electrode when the test cycle increased. Since the amount of molybdenum carbide reduced, the performance of the electrode worsened. For HER activity test, the amorphous carbon might be removed, but the molybdenum carbide might still remain on the electrode during the test. Since the amorphous carbon was removed, the surface area of the molybdenum carbide increased and it behaved better.

The molybdenum carbide structure of this work is very unique, but the formation mechanism of the chained flake structures does not become clear yet. The existence of amorphous carbon on the surface is also major obstacle for the performance. As molybdenum carbide has a potential application supercapacitors electrodes and HER activity, developing high purity samples is a very important and still remains a challenge.

4.5. Application and Future Work

This work is focused on interconnected flake structures of molybdenum carbide. Not only could molybdenum carbide see applications as electrodes for a supercapacitor and HER activity, but also quantum dots[188-192]. Molybdenum carbide has great potential for these applications and it is a sulfur free material. Molybdenum disulfide also performs well for these application, but has the downside of containing sulfur[187]. Although the synthetic method for this work is unique, the amorphous carbon on the surface remains a problem. Therefore, the high purity molybdenum carbide sample should be developed for applications in commercial devices.

As well as pursuing high purity, mixing some additives--such as carbon materials--also improves the performance of molybdenum carbide[191]. In order to obtain its better performance, studies for determining the best additives for molybdenum carbide are also important.

Chapter 5

Conclusion

This thesis highlights novel 3D nanomaterials and nanostructures based on interconnected carbon nanomaterials using solution chemistry and CVD methods. Many scientists have revealed that the structures of interconnected carbon nanomaterials provide high mechanical and electrochemical properties. There are still many challenges to clarify the mechanism of interconnection between carbon nanomaterials such as types of combination and control of the interconnection. Therefore, pursuing new 3D nanomaterials and nanostructures paves the way for obtaining a better comprehension of the field, which in turn, leads to their utilization as materials in a considerable amount of applications.

The CNT spheres that have porous and scaffold structures consisting of interconnected CNTs were synthesized by solution chemistry followed by freeze-drying. Previous work exhibited a lyophilization process that helps the shaping of the 3D architecture by sublimating the inside water. On the inside of the CNT

spheres, functionalized CNTs (CNT-COOH) can be interconnected with the aid of GAD, resorcinol and borax. Since the raw solution of the CNT spheres are water based, freeze-drying works well to bring porous structures by the sublimation process. SEM and TEM images showed the porous and scaffold structures of the CNT interconnection. In order to evaluate the mechanical properties, nano-indentation tests were carried out and the results revealed the high elasticity that the Young's modulus of a CNT sphere was measured at 4.2 KPa and the Young's modulus of the tip of a CNT sphere was measured as 102.5 ± 0.5 GPa at a low load compression of $10\mu N$. This allows the CNT spheres to be potentially applied to mechanical dampers with the aggregation. Although a CNT sphere itself cannot resist practical compression (the order of N or kN), the composite of aggregation of CNT spheres coated by PDMS can be an application for mechanical dampers due to the feasible mass production of CNT spheres. The performance as an electrode for supercapacitors, however, was relatively not good compared with other similar materials. TGA results also pointed the drawback of the CNT spheres in the fact that the weight was reduced to 60 % of the initial weight at $600℃$ in argon gas atmosphere. Since GAD and resorcinol have their melting points around $100\text{-}200℃$, the CNT spheres above the temperature is not stable.

CNTs were also grown on 2D materials (rGO and h-BN) by CVD methods. CNTs and 2D materials--such as graphene--usually have larger surface areas that can improve the performance of supercapacitors. In order to increase the surface area, many kinds of hybrid materials, which consist of some interconnected materials, have been developed. This thesis introduced two types of hybrid

structures consisting of CNTs and 2D materials (rGO and h-BN). Both of them were synthesized by CVD methods, and these hybrid CNTs and 2D materials were chemically interconnected. For CNTs on rGO hybrid structures, the initial state of the material was GO. When CNTs were grown on the GO, no additional catalyst was used. After the CNT growth, GO was reduced to rGO and CNTs were synthesized on the surface of the rGO randomly as well as inside the rGO layers. TEM images showed there were some metal particles inside the CNTs, which might be nickel particles from the nickel foam that worked as a catalyst. For CNTs on h-BN hybrid structures, the initial state of the material was h-BN onto a nickel foam. When CNTs were grown on the h-BN, aluminum and iron were deposited on the h-BN for the catalysts. CNTs were also synthesized on the surface of the h-BN randomly as well as inside the h-BN layers. TEM images showed CNTs were not hollow states and the CNTs incorporated encapsulated metal particles. Although there is similar work regarding vertically aligned CNTs synthesized on graphene, this work shows merit in the fact that there are randomly interconnected CNTs networks on 2D materials. So as to evaluate the performance of electrodes for supercapacitors, 4 types of electrodes which contain rGO, CNTs on rGO, h-BN, or CNTs on h-BN were made and tested for electrochemical performance. The results showed each 3D hybrid structure performed better compared to that without CNTs. CNTs on rGO performed the best which was 85.2 F/g at a current density of 0.5 A/g. Although the mechanism of these interconnections is not still clear, these two types of hybrid structures proposed instances of chemically interconnected structures.

Furthermore, unique interconnected flake structures of alpha-phase molybdenum carbide were developed by a CVD method. Since TMCs are expected to perform well as catalysts of HER activity and as electrodes for supercapacitors, many types of TMCs have been developed and evaluated for performance. The molybdenum carbide that was synthesized by a CVD method has novel interconnected structures. The molybdenum carbide shaped an oval structure that looks like a "Koban," and interconnected to form a chain with several flakes. According to the SEM and TEM images, the interconnection occurred randomly. The unique flakes were characterized as mainly alpha-phase molybdenum carbide by electron diffraction and XRD patterns. However, the surface was partially covered with amorphous carbon. Although the initial cycle of HER activity was not good, the molybdenum carbide performed low onset over potential (-16 mV at 5,000 cycles) after 5,000 cycles. The specific capacitance of the electrode for supercapacitors was 278.5 F/g at a current density of 0.5 A/g but had poor stability. Many reports demonstrate composites that are mixtures of base materials, such as molybdenum carbide and molybdenum disulfide, and additives, such as CNTs and graphene, behave with a better performance for both electrodes for supercapacitors and catalysts of HER activity. This thesis only evaluated the performance of the molybdenum carbide itself; therefore, finding good combinations of the molybdenum carbide and additives that can make the performance better is a future challenge. In addition, since each flake interconnects, the molybdenum carbide might have favorable mechanical properties because TMCs are usually strong materials.

Overall, this thesis discussed various types of novel 3D interconnected nanostructures based on carbon nanomaterials. Each of the study revealed intriguing characteristics and great potential for many applications. These results may help better understanding for 3D nanomaterials and nanostructures.

References

1. Kroto, H. W.; Heath, J. R.; O'brien, S. C.; Curl, R. F.; Smalley, R. E. C_{60}: Buckminsterfullerene. *Nature* **1985**, *318*, 162–163.

2. Endo, K.; Koizumi, S.; Otsuka, T.; Ida, T.; Morohashi, T.; Onoe, J.; Nakao, A.; Kurmaev, E. Z.; Moewes, A.; Chong, D. P. Analysis of Electron Spectra of Carbon Allotropes (Diamond, Graphite, Fullerene) by Density Functional Theory Calculations Using the Model Molecules. *J. Phys. Chem. A* **2003**, *107*, 9403–9408.

3. Saito, R.; Dresselhaus, G.; Dresselhaus, M. S. *Physical Properties of Carbon Nanotubes*; Imperial College Press: London, 1999.

4. Arnold, M. S.; Green, A. A.; Hulvat, J. F.; Stupp, S. I.; Hersam, M. C. Sorting Carbon Nanotubes by Electronic Structure Using Density Differentiation. *Nature Nanotech.* **2006**, *1*, 60–65.

5. Galano, A. Carbon Nanotubes: Promising Agents against Free Radicals. *Nanoscale* **2010**, *2*, 373.

6. Bellucci, S. Carbon Nanotubes: Physics and Applications. *phys. stat. sol. (c)* **2005**, *2*, 34–47.

7. Chae, H. G.; Kumar, S. Rigid-Rod Polymeric Fibers. *J. Appl. Polym. Sci.* **2006**, *100*, 791–802.

8. Meo, M.; Rossi, M. Prediction of Young's Modulus of Single Wall Carbon Nanotubes by Molecular-Mechanics Based Finite Element Modelling. *Composites Science and Technology* **2006**, *66*, 1597–1605.

9. Bahr, J. L.; Yang, J.; Kosynkin, D. V.; Bronikowski, M. J.; Smalley, R. E.; Tour, J. M. Functionalization of Carbon Nanotubes by Electrochemical Reduction of Aryl Diazonium Salts: A Bucky Paper Electrode. *J. Am. Chem. Soc.* **2001**, *123*, 6536–6542.

10. Derycke, V.; Martel, R.; Appenzeller, J.; Avouris, P. Carbon Nanotube Inter- and Intramolecular Logic Gates. *Nano Lett.* **2001**, *1*, 453–456.

11. Seike, K.; Fujii, Y.; Ohno, Y.; Maehashi, K.; Inoue, K.; Matsumoto, K. Floating-Gated Memory Based on Carbon Nanotube Field-Effect Transistors with Si Floating Dots. *Jpn. J. Appl. Phys.* **2014**, *53*, 04EN07.

12. Sitko, R.; Zawisza, B.; Malicka, E. Modification of Carbon Nanotubes for Preconcentration, Separation and Determination of Trace-Metal Ions. *TrAC* **2012**, *37*, 22–31.

13. Sayago, I.; Santos, H.; Horrillo, M.; Aleixandre, M.; Fernandez, M.; Terrado, E.; Tacchini, I.; Aroz, R.; Maser, W.; Benito, A. Carbon Nanotube Networks as Gas Sensors for NO_2 Detection. *Talanta* **2008**, *77*, 758–764.

14. Wu, H.-C.; Chang, X.; Liu, L.; Zhao, F.; Zhao, Y. Chemistry of Carbon Nanotubes in Biomedical Applications. *J. Mater. Chem.* **2010**, *20*, 1036–1052.

15. Lee, J.; Lee, K.; Park, S. S. Environmentally Friendly Preparation of Nanoparticle-Decorated Carbon Nanotube or Graphene Hybrid Structures and Their Potential Applications. *J. Mater. Sci.* **2015**, *51*, 2761–2770.

16. Liu, Z.; Tabakman, S.; Welsher, K.; Dai, H. Carbon Nanotubes in Biology and Medicine: In Vitro and in Vivo Detection, Imaging and Drug Delivery. *Nano Res.* **2009**, *2*, 85–120.

17. Hahm, M. G.; Reddy, A. L. M.; Cole, D. P.; Rivera, M.; Vento, J. A.; Nam, J.; Jung, H. Y.; Kim, Y. L.; Narayanan, N. T.; Hashim, D. P.; *et al.* Carbon Nanotube–Nanocup Hybrid Structures for High Power Supercapacitor Applications. *Nano Lett.* **2012**, *12*, 5616–5621.

18. Goodwin, D. G.; Marsh, K. M.; Sosa, I. B.; Payne, J. B.; Gorham, J. M.; Bouwer, E. J.; Fairbrother, D. H. Interactions of Microorganisms with Polymer Nanocomposite Surfaces Containing Oxidized Carbon Nanotubes. *Environ. Sci. Technol.* **2015**, *49*, 5484–5492.

19. Du, J.; Pei, S.; Ma, L.; Cheng, H.-M. 25th Anniversary Article: Carbon Nanotube- and Graphene-Based Transparent Conductive Films for Optoelectronic Devices. *Adv. Mater.* **2014**, *26*, 1958–1991.

20. Hanaei, H.; Assadi, M. K.; Saidur, R. Highly Efficient Antireflective and Self-Cleaning Coatings That Incorporate Carbon Nanotubes (CNTs) into Solar Cells: A Review. *Renewable and Sustainable Energy Reviews* **2016**, *59*, 620–635.

21. Patiño, J.; López-Salas, N.; Gutiérrez, M. C.; Carriazo, D.; Ferrer, M. L.; Monte, F. D. Phosphorus-Doped Carbon–Carbon Nanotube Hierarchical Monoliths as True Three-Dimensional Electrodes in Supercapacitor Cells. *J. Mater. Chem. A* **2016**, *4*, 1251–1263.

22. Tour, J. M. Materials Chemistry: Seeds of Selective Nanotube Growth. *Nature* **2014**, *512*, 30–31.

23. Kitiyanan, B.; Alvarez, W.; Harwell, J.; Resasco, D. Controlled Production of Single-Wall Carbon Nanotubes by Catalytic Decomposition of CO on Bimetallic Co–Mo Catalysts. *Chemical Physics Letters* **2000**, *317*, 497–503.

24. Technology/Fullerene http://www.vc60.com/en/tech/ (accessed Feb 1, 2016).

25. Scientists delve deeper into carbon nanotubes http://physicsworld.com/cws/article/news/2013/feb/19/scientists-delve-deeper-into-carbon-nanotubes (accessed Feb 1, 2016).

26. Iijima, S. Helical Microtubules of Graphitic Carbon. *Nature* **1991**, *354*, 56–58.

27. Iijima, S.; Ichihashi, T. Single-Shell Carbon Nanotubes of 1-Nm Diameter. *Nature* **1993**, *363*, 603–605.

28. Gao, Y.; Jin, B.; Shen, W.; Sinko, P. J.; Xie, X.; Zhang, H.; Jia, L. China and the United States—Global Partners, Competitors and Collaborators in Nanotechnology Development. *Nanomedicine: Nanotechnology, Biology and Medicine* **2016**, *12*, 13–19.

29. Bethune, D. S.; Klang, C. H.; Vries, M. S. D.; Gorman, G.; Savoy, R.; Vazquez, J.; Beyers, R. Cobalt-Catalysed Growth of Carbon Nanotubes with Single-Atomic-Layer Walls. *Nature* **1993**, *363*, 605–607.

30. Thess, A.; Lee, R.; Nikolaev, P.; Dai, H.; Petit, P.; Robert, J.; Xu, C.; Lee, Y. H.; Kim, S. G.; Rinzler, A. G.; *et al.* Crystalline Ropes of Metallic Carbon Nanotubes. *Science* **1996**, *273*, 483–487.

31. Kong, J.; Soh, H. T.; Cassell, A. M.; Quate, C. F.; Dai, H. Synthesis of Individual Single-Walled Carbon Nanotubes on Patterned Silicon Wafers. *Nature* **1998**, *395*, 878–881.

32. Endo, M.; Kroto, H. W. Formation of Carbon Nanofibers. *J. Phys. Chem.* **1992**, *96*, 6941–6944.

33. Dai, H.; Wong, E. W.; Lieber, C. M. Probing Electrical Transport in Nanomaterials: Conductivity of Individual Carbon Nanotubes. *Science* **1996**, *272*, 523–526.

34. Mansoor, M.; Shahid, M.; Habib, A. Optimization of Ethanol Flow Rate for Improved Catalytic Activity of Ni Particles to Synthesize MWCNTs Using a CVD Reactor. *Mat. Res.* **2014**, *17*, 739–746.

35. Kumar, M.; Ando, Y. ChemInform Abstract: Chemical Vapor Deposition Of Carbon Nanotubes: A Review on Growth Mechanism and Mass Production. *ChemInform* **2010**, *41*.

36. Nikolaev, P.; Bronikowski, M. J.; Bradley, R.; Rohmund, F.; Colbert, D. T.; Smith, K.; Smalley, R. E. Gas-Phase Catalytic Growth of Single-Walled Carbon Nanotubes from Carbon Monoxide. *Chemical Physics Letters* **1999**, *313*, 91–97.

37. Maruyama, S.; Kojima, R.; Miyauchi, Y.; Chiashi, S.; Kohno, M. Low-Temperature Synthesis of High-Purity Single-Walled Carbon Nanotubes from Alcohol. *Chemical Physics Letters* **2002**, *360*, 229–234.

38. Murakami, Y.; Chiashi, S.; Miyauchi, Y.; Hu, M.; Ogura, M.; Okubo, T.; Maruyama, S. Growth of Vertically Aligned Single-Walled Carbon Nanotube Films on Quartz

Substrates and Their Optical Anisotropy. *Chemical Physics Letters* **2004**, *385*, 298–303.

39. Hata, K. Water-Assisted Highly Efficient Synthesis of Impurity-Free Single-Walled Carbon Nanotubes. *Science* **2004**, *306*, 1362–1364.

40. Saito, T.; Ohshima, S.; Okazaki, T.; Ohmori, S.; Yumura, M.; Iijima, S. Selective Diameter Control of Single-Walled Carbon Nanotubes in the Gas-Phase Synthesis. *J. Nanosci. Nanotech.* **2008**, *8*, 6153–6157.

41. Miyata, Y.; Mizuno, K.; Kataura, H. Purity and Defect Characterization of Single-Wall Carbon Nanotubes Using Raman Spectroscopy. *Journal of Nanomaterials* **2011**, *2011*, 1–7.

42. Lei, T.; Chen, X.; Pitner, G.; Wong, H.-S. P.; Bao, Z. Removable and Recyclable Conjugated Polymers for Highly Selective and High-Yield Dispersion and Release of Low-Cost Carbon Nanotubes. *J. Am. Chem. Soc.* **2016**, *138*, 802–805.

43. Liu, H.; Nishide, D.; Tanaka, T.; Kataura, H. Large-Scale Single-Chirality Separation of Single-Wall Carbon Nanotubes by Simple Gel Chromatography. *Nat. Comms.* **2011**, *2*, 309.

44. Tanaka, T.; Liu, H.; Fujii, S.; Kataura, H. From Metal/Semiconductor Separation to Single-Chirality Separation of Single-Wall Carbon Nanotubes Using Gel. *Phys. Status Solidi RRL* **2011**, *5*, 301–306.

45. Bachilo, S. M.; Balzano, L.; Herrera, J. E.; Pompeo, F.; Resasco, D. E.; Weisman, R. B. Narrow (n,m)-Distribution of Single-Walled Carbon Nanotubes Grown Using a Solid Supported Catalyst. *J. Am. Chem. Soc.* **2003**, *125*, 11186–11187.

46. Endo, M.; Muramatsu, H.; Hayashi, T.; Kim, Y. A.; Terrones, M.; Dresselhaus, M. S. Nanotechnology: 'Buckypaper' from Coaxial Nanotubes. *Nature* **2005**, *433*, 476–476.

47. Villalpando-Paez, F.; Moura, L. G.; Fantini, C.; Muramatsu, H.; Hayashi, T.; Kim, Y. A.; Endo, M.; Terrones, M.; Pimenta, M. A.; Dresselhaus, M. S. Tunable Raman Spectroscopy Study of CVD and Peapod-Derived Bundled and Individual Double-Wall Carbon Nanotubes. *Phys. Rev. B* **2010**, *82*, 155416.

48. Hitosugi, S.; Yamasaki, T.; Isobe, H. Bottom-Up Synthesis and Thread-in-Bead Structures of Finite (n,0)-Zigzag Single-Wall Carbon Nanotubes. *J. Am. Chem. Soc.* **2012**, *134*, 12442–12445.

49. Sanchez-Valencia, J. R.; Dienel, T.; Gröning, O.; Shorubalko, I.; Mueller, A.; Jansen, M.; Amsharov, K.; Ruffieux, P.; Fasel, R. Controlled Synthesis of Single-Chirality Carbon Nanotubes. *Nature* **2014**, *512*, 61–64.

50. Yang, F.; Wang, X.; Zhang, D.; Yang, J.; Luo, D.; Xu, Z.; Wei, J.; Wang, J.-Q.; Xu, Z.; Peng, F.; *et al.* Chirality-Specific Growth of Single-Walled Carbon Nanotubes on Solid Alloy Catalysts. *Nature* **2014**, *510*, 522–524.

51. Omachi, H.; Nakayama, T.; Takahashi, E.; Segawa, Y.; Itami, K. Initiation of Carbon Nanotube Growth by Well-Defined Carbon Nanorings. *Nature Chem.* **2013**, *5*, 572–576.

52. Yu, X.; Zhang, J.; Choi, W.; Choi, J.-Y.; Kim, J. M.; Gan, L.; Liu, Z. Cap Formation Engineering: From Opened C_{60} To Single-Walled Carbon Nanotubes. *Nano Lett.* **2010**, *10*, 3343–3349.

53. Yao, Y.; Feng, C.; Zhang, J.; Liu, Z. "Cloning" of Single-Walled Carbon Nanotubes via Open-End Growth Mechanism. *Nano Lett.* **2009**, *9*, 1673–1677.

54. Artyukhov, V. I.; Penev, E. S.; Yakobson, B. I. Why Nanotubes Grow Chiral. *Nat. Comms.* **2014**, *5*, 4892.

55. O'connell, M. J. Band Gap Fluorescence from Individual Single-Walled Carbon Nanotubes. *Science* **2002**, *297*, 593–596.

56. Chen, C.; Liang, B.; Ogino, A.; Wang, X.; Nagatsu, M. Oxygen Functionalization of Multiwall Carbon Nanotubes by Microwave-Excited Surface-Wave Plasma Treatment. *J. Phys. Chem. C* **2009**, *113*, 7659–7665.

57. Zhao, J.; Park, H.; Han, J.; Lu, J. P. Electronic Properties of Carbon Nanotubes with Covalent Sidewall Functionalization. *J. Phys. Chem. B* **2004**, *108*, 4227–4230.

58. Novoselov, K. S. Electric Field Effect in Atomically Thin Carbon Films. *Science* **2004**, *306*, 666–669.

59. Carlsson, J. M. Graphene: Buckle or Break. *Nat. Mater.* **2007**, *6*, 801–802.

60. Pang, J.; Bachmatiuk, A.; Ibrahim, I.; Fu, L.; Placha, D.; Martynkova, G. S.; Trzebicka, B.; Gemming, T.; Eckert, J.; Rümmeli, M. H. CVD Growth of 1D and 2D sp2 Carbon Nanomaterials. *J. Mater. Sci.* **2015**, *51*, 640–667.

61. Boland, C. S.; Barwich, S.; Khan, U.; Coleman, J. N. High Stiffness Nano-Composite Fibres from Polyvinylalcohol Filled with Graphene and Boron Nitride. *Carbon* **2016**, *99*, 280–288.

62. Kumar, P.; Shahzad, F.; Yu, S.; Hong, S. M.; Kim, Y.-H.; Koo, C. M. Large-Area Reduced Graphene Oxide Thin Film with Excellent Thermal Conductivity and

Electromagnetic Interference Shielding Effectiveness. *Carbon* **2015**, *94*, 494–500.

63. Geim, A. K.; Novoselov, K. S. The Rise of Graphene. *Nat. Mater.* **2007**, *6*, 183–191.

64. Illustrated Information http://www.nobelprize.org/nobel_prizes/physics/laureates/2010/illpres.html (accessed Jan 30, 2016).

65. Kim, K. S.; Zhao, Y.; Jang, H.; Lee, S. Y.; Kim, J. M.; Kim, K. S.; Ahn, J.-H.; Kim, P.; Choi, J.-Y.; Hong, B. H. Large-Scale Pattern Growth of Graphene Films for Stretchable Transparent Electrodes. *Nature* **2009**, *457*, 706–710.

66. Son, Y.-W.; Cohen, M. L.; Louie, S. G. Energy Gaps in Graphene Nanoribbons. *Phys. Rev. Lett.* **2006**, *97*, 216803.

67. Yang, H.; Heo, J.; Park, S.; Song, H. J.; Seo, D. H.; Byun, K.-E.; Kim, P.; Yoo, I.; Chung, H.-J.; Kim, K. Graphene Barristor, a Triode Device With a Gate-Controlled Schottky Barrier. *Science* **2012**, *336*, 1140–1143.

68. Bolotin, K.; Sikes, K.; Jiang, Z.; Klima, M.; Fudenberg, G.; Hone, J.; Kim, P.; Stormer, H. Ultrahigh Electron Mobility in Suspended Graphene. *Solid State Communications* **2008**, *146*, 351–355.

69. Novoselov, K. S.; Geim, A. K.; Morozov, S. V.; Jiang, D.; Katsnelson, M. I.; Grigorieva, I. V.; Dubonos, S. V.; Firsov, A. A. Two-Dimensional Gas of Massless Dirac Fermions in Graphene. *Nature* **2005**, *438*, 197–200.

70. Zhang, Y.; Tan, Y.-W.; Stormer, H. L.; Kim, P. Experimental Observation of the Quantum Hall Effect and Berry's Phase in Graphene. *Nature* **2005**, *438*, 201–204.

71. Cai, C.; Jia, F.; Li, A.; Huang, F.; Xu, Z.; Qiu, L.; Chen, Y.; Fei, G.; Wang, M. Crackless Transfer of Large-Area Graphene Films for Superior-Performance Transparent Electrodes. *Carbon* **2016**, *98*, 457–462.

72. Zhu, Y.; Sun, Z.; Yan, Z.; Jin, Z.; Tour, J. M. Rational Design of Hybrid Graphene Films for High-Performance Transparent Electrodes. *ACS Nano* **2011**, *5*, 6472–6479.

73. Li, X.; Cai, W.; An, J.; Kim, S.; Nah, J.; Yang, D.; Piner, R.; Velamakanni, A.; Jung, I.; Tutuc, E.; *et al.* Large-Area Synthesis of High-Quality and Uniform Graphene Films on Copper Foils. *Science* **2009**, *324*, 1312–1314.

74. Bae, S.; Kim, H.; Lee, Y.; Xu, X.; Park, J.-S.; Zheng, Y.; Balakrishnan, J.; Lei, T.; Kim, H. R.; Song, Y. I.; *et al.* Roll-to-Roll Production of 30-Inch Graphene Films for Transparent Electrodes. *Nature Nanotech.* **2010**, *5*, 574–578.

75. Zhang, X.; Wang, L.; Xin, J.; Yakobson, B. I.; Ding, F. Role of Hydrogen in Graphene Chemical Vapor Deposition Growth on a Copper Surface. *J. Am. Chem. Soc.* **2014**, *136*, 3040–3047.

76. Chua, C. K.; Pumera, M. Chemical Reduction of Graphene Oxide: a Synthetic Chemistry Viewpoint. *Chem. Soc. Rev.* **2014**, *43*, 291–312.

77. Li, X.; Magnuson, C. W.; Venugopal, A.; Tromp, R. M.; Hannon, J. B.; Vogel, E. M.; Colombo, L.; Ruoff, R. S. Large-Area Graphene Single Crystals Grown by Low-Pressure Chemical Vapor Deposition of Methane on Copper. *J. Am. Chem. Soc.* **2011**, *133*, 2816–2819.

78. Brodie, B. C. On The Atomic Weight of Graphite. *Philosophical Transactions of the Royal Society of London* **1859**, *149*, 249–259.

79. Hummers, W. S.; Offeman, R. E. Preparation of Graphitic Oxide. *J. Am. Chem. Soc.* **1958**, *80*, 1339–1339.

80. Marcano, D. C.; Kosynkin, D. V.; Berlin, J. M.; Sinitskii, A.; Sun, Z.; Slesarev, A.; Alemany, L. B.; Lu, W.; Tour, J. M. Improved Synthesis of Graphene Oxide. *ACS Nano* **2010**, *4*, 4806–4814.

81. Mao, S.; Pu, H.; Chen, J. Graphene Oxide and Its Reduction: Modeling and Experimental Progress. *RSC Adv.* **2012**, *2*, 2643.

82. Compton, O. C.; Nguyen, S. T. Graphene Oxide, Highly Reduced Graphene Oxide, and Graphene: Versatile Building Blocks for Carbon-Based Materials. *Small* **2010**, *6*, 711–723.

83. Dreyer, D. R.; Park, S.; Bielawski, C. W.; Ruoff, R. S. The Chemistry of Graphene Oxide. *Chem. Soc. Rev.* **2010**, *39*, 228–240.

84. Pei, S.; Cheng, H.-M. The Reduction of Graphene Oxide. *Carbon* **2012**, *50*, 3210–3228.

85. Li, L.; Zhang, J.; Peng, Z.; Li, Y.; Gao, C.; Ji, Y.; Ye, R.; Kim, N. D.; Zhong, Q.; Yang, Y.; *et al.* High-Performance Pseudocapacitive Microsupercapacitors from Laser-Induced Graphene. *Adv. Mater.* **2015**, *28*, 838–845.

86. Ye, G.; Gong, Y.; Keyshar, K.; Husain, E. A. M.; Brunetto, G.; Yang, S.; Vajtai, R.; Ajayan, P. M. 3D Reduced Graphene Oxide Coated V_2O_5 Nanoribbon Scaffolds for

High-Capacity Supercapacitor Electrodes. *Part. Part. Syst. Charact.* **2015**, *32*, 817–821.

87. Jana, M.; Kumar, J. S.; Khanra, P.; Samanta, P.; Koo, H.; Murmu, N. C.; Kuila, T. Superior Performance of Asymmetric Supercapacitor Based on Reduced Graphene Oxide–Manganese Carbonate as Positive and Sono-Chemically Reduced Graphene Oxide as Negative Electrode Materials. *Journal of Power Sources* **2016**, *303*, 222–233.

88. Quan, H.; Cheng, B.; Xiao, Y.; Lei, S. One-Pot Synthesis of α-Fe_2O_3 Nanoplates-Reduced Graphene Oxide Composites for Supercapacitor Application. *Chemical Engineering Journal* **2016**, *286*, 165–173.

89. Zou, Y.; Wang, Q.; Xiang, C.; She, Z.; Chu, H.; Qiu, S.; Xu, F.; Liu, S.; Tang, C.; Sun, L. One-Pot Synthesis of Ternary Polypyrrole–Prussian-Blue–Graphene-Oxide Hybrid Composite as Electrode Material for High-Performance Supercapacitors. *Electrochimica Acta* **2016**, *188*, 126–134.

90. Tsuchiya, T.; Terabe, K.; Aono, M. In Situ and Non-Volatile Bandgap Tuning of Multilayer Graphene Oxide in an All-Solid-State Electric Double-Layer Transistor. *Adv. Mater.* **2014**, *26*, 1087–1091.

91. Gao, W.; Singh, N.; Song, L.; Liu, Z.; Reddy, A. L. M.; Ci, L.; Vajtai, R.; Zhang, Q.; Wei, B.; Ajayan, P. M. Direct Laser Writing of Micro-Supercapacitors on Hydrated Graphite Oxide Films. *Nature Nanotech.* **2011**, *6*, 496–500.

92. Morales-Guio, C. G.; Stern, L.-A.; Hu, X. Nanostructured Hydrotreating Catalysts for Electrochemical Hydrogen Evolution. *Chem. Soc. Rev.* **2014**, *43*, 6555.

93. Michalsky, R.; Zhang, Y.-J.; Peterson, A. A. Trends in the Hydrogen Evolution Activity of Metal Carbide Catalysts. *ACS Catal.* **2014**, *4*, 1274–1278.

94. Meyer, S.; Nikiforov, A. V.; Petrushina, I. M.; Köhler, K.; Christensen, E.; Jensen, J. O.; Bjerrum, N. J. Transition Metal Carbides (WC, Mo_2C, TaC, NbC) as Potential Electrocatalysts for the Hydrogen Evolution Reaction (HER) at Medium Temperatures. *International Journal of Hydrogen Energy* **2015**, *40*, 2905–2911.

95. Eames, C.; Islam, M. S. Ion Intercalation into Two-Dimensional Transition-Metal Carbides: Global Screening for New High-Capacity Battery Materials. *J. Am. Chem. Soc.* **2014**, *136*, 16270–16276.

96. Yang, E.; Ji, H.; Kim, J.; Kim, H.; Jung, Y. Exploring the Possibilities of Two-Dimensional Transition Metal Carbides as Anode Materials for Sodium Batteries. *Phys. Chem. Chem. Phys.* **2015**, *17*, 5000–5005.

97. Vesborg, P. C. K.; Seger, B.; Chorkendorff, I. Recent Development in Hydrogen Evolution Reaction Catalysts and Their Practical Implementation. *J. Phys. Chem. Lett.* **2015**, *6*, 951–957.

98. Esposito, D. V.; Hunt, S. T.; Stottlemyer, A. L.; Dobson, K. D.; Mccandless, B. E.; Birkmire, R. W.; Chen, J. G. Low-Cost Hydrogen-Evolution Catalysts Based on Monolayer Platinum on Tungsten Monocarbide Substrates. *Angewandte Chemie International Edition* **2010**, *49*, 9859–9862.

99. Zhang, N.; Ma, W.; Wu, T.; Wang, H.; Han, D.; Niu, L. Edge-Rich MoS_2 Naonosheets Rooting into Polyaniline Nanofibers as Effective Catalyst for Electrochemical Hydrogen Evolution. *Electrochimica Acta* **2015**, *180*, 155–163.

100. Zheng, Y.; Jiao, Y.; Jaroniec, M.; Qiao, S. Z. Advancing the Electrochemistry of the Hydrogen-Evolution Reaction through Combining Experiment and Theory. *Angew. Chem. Int. Ed.* **2014**, *54*, 52–65.

101. Ting, L. R. L.; Deng, Y.; Ma, L.; Zhang, Y.-J.; Peterson, A. A.; Yeo, B. S. Catalytic Activities of Sulfur Atoms in Amorphous Molybdenum Sulfide for the Electrochemical Hydrogen Evolution Reaction. *ACS Catal.* **2016**, *6*, 861–867.

102. Shatynski, S. R. The Thermochemistry of Transition Metal Carbides. *Oxid. Met.* **1979**, *13*, 105–118.

103. Tuomi, S.; Guil-Lopez, R.; Kallio, T. Molybdenum Carbide Nanoparticles as a Catalyst for the Hydrogen Evolution Reaction and the Effect of PH. *Journal of Catalysis* **2016**, *334*, 102–109.

104. Li, Z.; Dai, X.; Du, K.; Ma, Y.; Liu, M.; Sun, H.; Ma, X.; Zhang, X. Reduced Graphene Oxide/O-MWCNT Hybrids Functionalized with p-Phenylenediamine as High-Performance MoS_2 Electrocatalyst Support for Hydrogen Evolution Reaction. *J. Phys. Chem. C* **2016**, *120*, 1478–1487.

105. Hinnemann, B.; Moses, P. G.; Bonde, J.; Jørgensen, K. P.; Nielsen, J. H.; Horch, S.; Chorkendorff, I.; Nørskov, J. K. Biomimetic Hydrogen Evolution: MoS_2 Nanoparticles as Catalyst for Hydrogen Evolution. *J. Am. Chem. Soc.* **2005**, *127*, 5308–5309.

106. Luo, Q.; Wang, T.; Walther, G.; Beller, M.; Jiao, H. Molybdenum Carbide Catalysed Hydrogen Production from Formic Acid – A Density Functional Theory Study. *Journal of Power Sources* **2014**, *246*, 548–555.

107.   Chen, M.; Zhang, J.; Chen, Q.; Qi, M.; Xia, X. Construction of Reduced Graphene Oxide Supported Molybdenum Carbides Composite Electrode as High-Performance Anode Materials for Lithium Ion Batteries. *Materials Research Bulletin* **2016**, *73*, 459–464.

108.   Parthé, E.; Sadogopan, V. The Structure of Dimolybdenum Carbide by Neutron Diffraction Technique. *Acta Cryst.* **1963**, *16*, 202–205.

109.   Dubois, J.; Epicier, T.; Esnouf, C.; Fantozzi, G.; Convert, P. Neutron Powder Diffraction Studies of Transition Metal Hemicarbides M_2C_{1-x}—I. Motivation for a Study on W_2C and Mo_2C and Experimental Background for an in Situ Investigation at Elevated Temperature. *Acta Metallurgica* **1988**, *36*, 1891–1901.

110.   Page, K.; Li, J.; Savinelli, R.; Szumila, H. N.; Zhang, J.; Stalick, J. K.; Proffen, T.; Scott, S. L.; Seshadri, R. Reciprocal-Space and Real-Space Neutron Investigation of Nanostructured Mo_2C and WC. *Solid State Sciences* **2008**, *10*, 1499–1510.

111.   Lee, J.-K.; Kim, S.-Y.; Ott, R. T.; Kim, J.-Y.; Eckert, J.; Lee, M.-H. Effect of Reinforcement Phase on the Mechanical Property of Tungsten Nanocomposite Synthesized by Spark Plasma Sintering. *International Journal of Refractory Metals and Hard Materials* **2016**, *54*, 14–18.

112.   Gui, X.; Zeng, Z.; Cao, A.; Lin, Z.; Zeng, H.; Xiang, R.; Wu, T.; Zhu, Y.; Tang, Z. Elastic Shape Recovery of Carbon Nanotube Sponges in Liquid Oil. *J. Mater. Chem.* **2012**, *22*, 18300.

113.   Hashim, D. P.; Narayanan, N. T.; Romo-Herrera, J. M.; Cullen, D. A.; Hahm, M. G.; Lezzi, P.; Suttle, J. R.; Kelkhoff, D.; Muñoz-Sandoval, E.; Ganguli, S.; *et al*

Covalently Bonded Three-Dimensional Carbon Nanotube Solids via Boron Induced Nanojunctions. *Sci. Rep.* **2012**, *2*.

114.   Chen, Z.; Ren, W.; Gao, L.; Liu, B.; Pei, S.; Cheng, H.-M. Three-Dimensional Flexible and Conductive Interconnected Graphene Networks Grown by Chemical Vapour Deposition. *Nat Mater.* **2011**, *10*, 424–428.

115.   Seo, J.; Lee, T. J.; Ko, S.; Yeo, H.; Kim, S.; Noh, T.; Song, S.; Sung, M. M.; Lee, H. Hierarchical and Multifunctional Three-Dimensional Network of Carbon Nanotubes for Microfluidic Applications. *Adv. Mater.* **2012**, *24*, 1975–1979.

116.   Kotal, M.; Bhowmick, A. K. Multifunctional Hybrid Materials Based on Carbon Nanotube Chemically Bonded to Reduced Graphene Oxide. *J. Phys. Chem. C* **2013**, *117*, 25865–25875.

117.   Fan, Z.; Yan, J.; Zhi, L.; Zhang, Q.; Wei, T.; Feng, J.; Zhang, M.; Qian, W.; Wei, F. A Three-Dimensional Carbon Nanotube/Graphene Sandwich and its Application as Electrode in Supercapacitors. *Adv. Mater.* **2010**, *22*, 3723–3728.

118.   Tylianakis, E.; Dimitrakakis, G. K.; Martin-Martinez, F. J.; Melchor, S.; Dobado, J. A.; Klontzas, E.; Froudakis, G. E. Designing Novel Nanoporous Architectures of Carbon Nanotubes for Hydrogen Storage. *International Journal of Hydrogen Energy* **2014**, *39*, 9825–9829.

119.   Cui, Y.; Cheng, Q.-Y.; Wu, H.; Wei, Z.; Han, B.-H. Graphene Oxide-Based Benzimidazole-Crosslinked Networks for High-Performance Supercapacitors. *Nanoscale* **2013**, *5*, 8367.

120. Lin, Z.; Gui, X.; Zeng, Z.; Liang, B.; Chen, W.; Liu, M.; Zhu, Y.; Cao, A.; Tang, Z. Biomimetic Carbon Nanotube Films with Gradient Structure and Locally Tunable Mechanical Property. *Adv. Funct. Mater.* **2015**, *25*, 7173–7179.

121. Ozden, S.; Ge, L.; Narayanan, T. N.; Hart, A. H. C.; Yang, H.; Sridhar, S.; Vajtai, R.; Ajayan, P. M. Anisotropically Functionalized Carbon Nanotube Array Based Hygroscopic Scaffolds. *ACS Appl. Mater. Interfaces* **2014**, *6*, 10608–10613.

122. Ozden, S.; Tiwary, C. S.; Hart, A. H. C.; Chipara, A. C.; Romero-Aburto, R.; Rodrigues, M.-T. F.; Taha-Tijerina, J.; Vajtai, R.; Ajayan, P. M. Density Variant Carbon Nanotube Interconnected Solids. *Adv. Mater.* **2015**, *27*, 1842–1850.

123. Ye, S.; Feng, J.; Wu, P. Highly Elastic Graphene Oxide–Epoxy Composite Aerogels via Simple Freeze-Drying and Subsequent Routine Curing. *J. Mater. Chem. A* **2013**, *1*, 3495.

124. Zhang, Q.; Xu, X.; Lin, D.; Chen, W.; Xiong, G.; Yu, Y.; Fisher, T. S.; Li, H. Hyperbolically Patterned 3D Graphene Metamaterial with Negative Poisson's Ratio and Superelasticity. *Adv. Mater.* **2016**.

125. Sudeep, P. M.; Narayanan, T. N.; Ganesan, A.; Shaijumon, M. M.; Yang, H.; Ozden, S.; Patra, P. K.; Pasquali, M.; Vajtai, R.; Ganguli, S.; *et al.* Covalently Interconnected Three-Dimensional Graphene Oxide Solids. *ACS Nano* **2013**, *7*, 7034–7040.

126. Cong, H.-P.; Ren, X.-C.; Wang, P.; Yu, S.-H. Macroscopic Multifunctional Graphene-Based Hydrogels and Aerogels by a Metal Ion Induced Self-Assembly Process. *ACS Nano* **2012**, *6*, 2693–2703.

127. Kim, S.; Zhou, S.; Hu, Y.; Acik, M.; Chabal, Y. J.; Berger, C.; Heer, W. D.; Bongiorno, A.; Riedo, E. Room-Temperature Metastability of Multilayer Graphene Oxide Films. *Nat. Mater.* **2012**, *11*, 544–549.

128. Vinod, S.; Tiwary, C. S.; Autreto, P. A. D. S.; Taha-Tijerina, J.; Ozden, S.; Chipara, A. C.; Vajtai, R.; Galvao, D. S.; Narayanan, T. N.; Ajayan, P. M. Low-Density Three-Dimensional Foam Using Self-Reinforced Hybrid Two-Dimensional Atomic Layers. *Nat. Comms.* **2014**, *5*.

129. Jansen, M. High Performance Non-Oxide Ceramics II; Springer: Berlin.

130. Catellani, A.; Posternak, M.; Baldereschi, A.; Freeman, A. J. Bulk and Surface Electronic Structure of Hexagonal Boron Nitride. *Phys. Rev. B* **1987**, *36*, 6105–6111.

131. Kubota, Y.; Watanabe, K.; Tsuda, O.; Taniguchi, T. Deep Ultraviolet Light-Emitting Hexagonal Boron Nitride Synthesized at Atmospheric Pressure. *Science* **2007**, *317*, 932–934.

132. Lin, Y.; Williams, T. V.; Xu, T.-B.; Cao, W.; Elsayed-Ali, H. E.; Connell, J. W. Aqueous Dispersions of Few-Layered and Monolayered Hexagonal Boron Nitride Nanosheets from Sonication-Assisted Hydrolysis: Critical Role of Water. *J. Phys. Chem. C* **2011**, *115*, 2679–2685.

133. Liu, Z.; Ma, L.; Shi, G.; Zhou, W.; Gong, Y.; Lei, S.; Yang, X.; Zhang, J.; Yu, J.; Hackenberg, K. P.; *et al.* In-Plane Heterostructures of Graphene and Hexagonal Boron Nitride with Controlled Domain Sizes. *Nature Nanotech.* **2013**, *8*, 119–124.

134.   Rafiee, M. A.; Narayanan, T. N.; Hashim, D. P.; Sakhavand, N.; Shahsavari, R.; Vajtai, R.; Ajayan, P. M. Hexagonal Boron Nitride and Graphite Oxide Reinforced Multifunctional Porous Cement Composites. *Adv. Funct. Mater.* **2013**, *23*, 5624–5630.

135.   Song, L.; Ci, L.; Lu, H.; Sorokin, P. B.; Jin, C.; Ni, J.; Kvashnin, A. G.; Kvashnin, D. G.; Lou, J.; Yakobson, B. I.; *et al.* Large Scale Growth and Characterization of Atomic Hexagonal Boron Nitride Layers. *Nano Lett.* **2010**, *10*, 3209–3215.

136.   Nag, A.; Raidongia, K.; Hembram, K. P. S. S.; Datta, R.; Waghmare, U. V.; Rao, C. N. R. Graphene Analogues of BN: Novel Synthesis and Properties. *ACS Nano* **2010**, *4*, 1539–1544.

137.   Hahm, M. G.; Lee, J.-H.; Hart, A. H. C.; Song, S. M.; Nam, J.; Jung, H. Y.; Hashim, D. P.; Li, B.; Narayanan, T. N.; Park, C.-D.; *et al.* Carbon Nanotube Core Graphitic Shell Hybrid Fibers. *ACS Nano* **2013**, *7*, 10971–10977.

138.   Ratha, S.; Marri, S. R.; Behera, J. N.; Rout, C. S. High-Energy-Density Supercapacitors Based on Patronite/Single-Walled Carbon Nanotubes/Reduced Graphene Oxide Hybrids. *Eur. J. Inorg. Chem.* **2015**, *2016*, 259–265.

139.   Kim, N. D.; Li, Y.; Wang, G.; Fan, X.; Jiang, J.; Li, L.; Ji, Y.; Ruan, G.; Hauge, R. H.; Tour, J. M. Growth and Transfer of Seamless 3D Graphene–Nanotube Hybrids. *Nano Lett.* **2016**.

140.   Yang, S.-Y.; Chang, K.-H.; Tien, H.-W.; Lee, Y.-F.; Li, S.-M.; Wang, Y.-S.; Wang, J.-Y.; Ma, C.-C. M.; Hu, C.-C. Design and Tailoring of a Hierarchical Graphene-Carbon

Nanotube Architecture for Supercapacitors. *J. Mater. Chem.* **2011**, *21*, 2374–2380.

141.   Xue, Y.; Ding, Y.; Niu, J.; Xia, Z.; Roy, A.; Chen, H.; Qu, J.; Wang, Z. L.; Dai, L. Rationally Designed Graphene-Nanotube 3D Architectures with a Seamless Nodal Junction for Efficient Energy Conversion and Storage. *Science Advances* **2015**, *1*.

142.   Cui, X.; Lv, R.; Sagar, R. U. R.; Liu, C.; Zhang, Z. Reduced Graphene Oxide/Carbon Nanotube Hybrid Film as High Performance Negative Electrode for Supercapacitor. *Electrochimica Acta* **2015**, *169*, 342–350.

143.   Pham, D. T.; Lee, T. H.; Luong, D. H.; Yao, F.; Ghosh, A.; Le, V. T.; Kim, T. H.; Li, B.; Chang, J.; Lee, Y. H. Carbon Nanotube-Bridged Graphene 3D Building Blocks for Ultrafast Compact Supercapacitors. *ACS Nano* **2015**, *9*, 2018–2027.

144.   Zhu, Y.; Li, L.; Zhang, C.; Casillas, G.; Sun, Z.; Yan, Z.; Ruan, G.; Peng, Z.; Raji, A.-R. O.; Kittrell, C.; *et al.* A Seamless Three-Dimensional Carbon Nanotube Graphene Hybrid Material. *Nat. Comms.* **2012**, *3*, 1225.

145.   Terse-Thakoor, T.; Komori, K.; Ramnani, P.; Lee, I.; Mulchandani, A. Electrochemically Functionalized Seamless Three-Dimensional Graphene-Carbon Nanotube Hybrid for Direct Electron Transfer of Glucose Oxidase and Bioelectrocatalysis. *Langmuir* **2015**, *31*, 13054–13061.

146.   Yan, Z.; Ma, L.; Zhu, Y.; Lahiri, I.; Hahm, M. G.; Liu, Z.; Yang, S.; Xiang, C.; Lu, W.; Peng, Z.; *et al.* Three-Dimensional Metal–Graphene–Nanotube Multifunctional Hybrid Materials. *ACS Nano* **2013**, *7*, 58–64.

147.   Du, F.; Yu, D.; Dai, L.; Ganguli, S.; Varshney, V.; Roy, A. K. Preparation of Tunable 3D Pillared Carbon Nanotube–Graphene Networks for High-Performance Capacitance. *Chem. Mater.* **2011**, *23*, 4810–4816.

148.   Singh, A. P.; Mishra, M.; Hashim, D. P.; Narayanan, T.; Hahm, M. G.; Kumar, P.; Dwivedi, J.; Kedawat, G.; Gupta, A.; Singh, B. P.; *et al.* Probing the Engineered Sandwich Network of Vertically Aligned Carbon Nanotube–Reduced Graphene Oxide Composites for High Performance Electromagnetic Interference Shielding Applications. *Carbon* **2015**, *85*, 79–88.

149.   Shahriary, L.; Nair, R.; Sabharwal, S.; Athawale, A. A. One-Step Synthesis of Ag–Reduced Graphene Oxide–Multiwalled Carbon Nanotubes for Enhanced Antibacterial Activities. *New J. Chem.* **2015**, *39*, 4583–4590.

150.   Wang, Y.-S.; Li, S.-M.; Hsiao, S.-T.; Liao, W.-H.; Yang, S.-Y.; Ma, C.-C. M.; Hu, C.-C. Electrochemical Composite Deposition of Porous Cactus-like Manganese Oxide/Reduced Graphene Oxide–Carbon Nanotube Hybrids for High-Power Asymmetric Supercapacitors. *J. Mater. Chem. C* **2015**, *3*, 4987–4996.

151.   Yang, X.; Li, Z.; He, F.; Liu, M.; Bai, B.; Liu, W.; Qiu, X.; Zhou, H.; Li, C.; Dai, Q. Enhanced Field Emission From a Carbon Nanotube Array Coated with a Hexagonal Boron Nitride Thin Film. *Small* **2015**, *11*, 3710–3716.

152.   Muthu, R. N.; Rajashabala, S.; Kannan, R. Hexagonal Boron Nitride (h-BN) Nanoparticles Decorated Multi-Walled Carbon Nanotubes (MWCNT) for Hydrogen Storage. *Renewable Energy* **2016**, *85*, 387–394.

153. Lee, K. H.; Shin, H.-J.; Lee, J.; Lee, I.-Y.; Kim, G.-H.; Choi, J.-Y.; Kim, S.-W. Large-Scale Synthesis of High-Quality Hexagonal Boron Nitride Nanosheets for Large-Area Graphene Electronics. *Nano Lett.* **2012**, *12*, 714–718.

154. Watanabe, K.; Taniguchi, T.; Kanda, H. Direct-Bandgap Properties and Evidence for Ultraviolet Lasing of Hexagonal Boron Nitride Single Crystal. *Nat. Mater.* **2004**, *3*, 404–409.

155. Shayeganfar, F.; Shahsavari, R. Electronic and Pseudomagnetic Properties of Hybrid Carbon/Boron-Nitride Nanomaterials via Ab-Initio Calculations and Elasticity Theory. *Carbon* **2016**, *99*, 523–532.

156. Vickery, J. L.; Patil, A. J.; Mann, S. Fabrication of Graphene-Polymer Nanocomposites With Higher-Order Three-Dimensional Architectures. *Adv. Mater.* **2009**, *21*, 2180–2184.

157. Liu, J.; Rinzler, A. G.; Dai, H.; Hafner, J. H.; Bradley, R. K.; Boul, P. J.; Lu, A.; Iverson, T.; Shelimov, K.; Huffman, C. B.; Rodriguez-Macias, F.; Shon, Y. S.; Lee, T. R.; Colbert, D. T.; Smalley, R. E. Fullerene Pipes. *Science* **1998**, *280*, 1253–1256.

158. Worsley, K. A.; Kondrat, R. W.; Pal, S. K.; Kalinina, I.; Haddon, R. C. Isolation and Identification of Low Molecular Weight Carboxylated Carbons Derived from the Nitric Acid Treatment of Single-Walled Carbon Nanotubes. *Carbon* **2011**, *49*, 4982–4986.

159. Kabbani, M. A.; Tiwary, C. S.; Autreto, P. A.; Brunetto, G.; Som, A.; Krishnadas, K.; Ozden, S.; Hackenberg, K. P.; Gong, Y.; Galvao, D. S.; *et al.* Ambient Solid-State

Mechano-Chemical Reactions between Functionalized Carbon Nanotubes. *Nat. Comms.* **2015**, *6*, 7291.

160. Murugan, E.; Arumugam, S. New Dendrimer Functionalized Multi-Walled Carbon Nanotube Hybrids for Bone Tissue Engineering. *RSC Adv.* **2014**, *4*, 35428.

161. Rubinson, K. A.; Rubinson, J. F. *Contemporary Instrumental Analysis*; Prentice Hall: Upper Saddle River, NJ, 2000.

162. Multi Walled Carbon Nanotubes 20-30nm | Cheap Tubes https://www.cheaptubes.com/product/multi-walled-carbon-nanotubes-20-30nm/ (accessed Apr 2, 2016).

163. Sharma, P.; Bhalla, V.; Dravid, V.; Shekhawat, G.; J.-W.; Prasad, E. S.; Suri, C. R. Enhancing Electrochemical Detection on Graphene Oxide-CNT Nanostructured Electrodes Using Magneto-Nanobioprobes. *Sci. Rep.* **2012**, *2*.

164. Rajendran, R.; Shrestha, L. K.; Minami, K.; Subramanian, M.; Jayavel, R.; Ariga, K. Dimensionally Integrated Nanoarchitectonics for a Novel Composite from 0D, 1D, and 2D Nanomaterials: $RGO/CNT/CeO_2$ Ternary Nanocomposites with Electrochemical Performance. *J. Mater. Chem. A* **2014**, *2*, 18480–18487.

165. Zhao, Z.; Dai, Y.; Ge, G.; Guo, X.; Wang, G. Facile Simultaneous Defect Production and O,N-Doping of Carbon Nanotubes with Unexpected Catalytic Performance for Clean and Energy-Saving Production of Styrene. *Green Chem.* **2015**, *17*, 3723–3727.

166. Material Safety Data Sheet, Glutaraldehyde Solution, G6257, Sigma-Aldrich, 2015.

167. Material Safety Data Sheet, Resorcinol, 398047, Sigma-Aldrich, 2015.

168. Brunauer, S.; Emmett, P. H.; Teller, E. Adsorption of Gases in Multimolecular Layers. *J. Am. Chem. Soc.* **1938**, *60*, 309–319.

169. Xu, X.; Liu, Y.; Wang, M.; Zhu, C.; Lu, T.; Zhao, R.; Pan, L. Hierarchical Hybrids with Microporous Carbon Spheres Decorated Three-Dimensional Graphene Frameworks for Capacitive Applications in Supercapacitor and Deionization. *Electrochimica Acta* **2016**, *193*, 88–95.

170. Yoo, J. J.; Balakrishnan, K.; Huang, J.; Meunier, V.; Sumpter, B. G.; Srivastava, A.; Conway, M.; Reddy, A. L. M.; Yu, J.; Vajtai, R.; *et al.* Ultrathin Planar Graphene Supercapacitors. *Nano Lett.* **2011**, *11*, 1423–1427.

171. Jung, H. Y.; Karimi, M. B.; Hahm, M. G.; Ajayan, P. M.; Jung, Y. J. Transparent, Flexible Supercapacitors from Nano-Engineered Carbon Films. *Sci. Rep.* **2012**, *2*.

172. Kaempgen, M.; Chan, C. K.; Ma, J.; Cui, Y.; Gruner, G. Printable Thin Film Supercapacitors Using Single-Walled Carbon Nanotubes. *Nano Lett.* **2009**, *9*, 1872–1876.

173. Sambasivarao, S. V. The biomolecular simulation program. *J. Chem. Inf. Model.* **2013**, *18*, 1199–1216.

174. Vanommeslaeghe, K.; MacKerell, A. D. Automation of the CHARMM general force field (CGenFF) I: Bond perception and atom typing. *J. Chem. Inf. Model.* **2012**, *52*, 3144–3154.

175. Plimpton, S. Fast Parallel Algorithms for Short-Range Molecular Dynamics. *J. Comput. Chem.* **1995**, *117*, 1–19.

176. Steffen, C.; Thomas, K.; Huniar, U.; Hellweg, A.; Rubner, O.; Schroer, A. TmoleX-A Graphical User Interface for TURBOMOLE. *J. Comput. Chem.* **2010**, *31*, 2967–2970.

177. Lian, G.; Zhang, X.; Zhu, L.; Tan, M.; Cui, D.; Wang, Q. A Facile Solid State Reaction Route towards Nearly Monodisperse Hexagonal Boron Nitride Nanoparticles. *J. Mater. Chem.* **2010**, *20*, 3736.

178. Xiong, Y.; Yang, S.; Xiong, C.; Pi, H.; Zhang, J.; Ren, Z.; Mai, Y.; Xu, W.; Dai, G.; Song, S.; *et al.* Preparation And Characterization of CBN Ternary Compounds with Nano-Structure. *Physica B: Condensed Matter* **2006**, *382*, 151–155.

179. Molybdenum carbide http://www.sigmaaldrich.com/catalog/product/aldrich/399531?lang=en (accessed Apr 2, 2016).

180. Molybdenum Carbide Powder http://www.us-nano.com/inc/sdetail/6714 (accessed Apr 2, 2016).

181. Cetinkaya, S.; Eroglu, S. Thermodynamic Analysis and Synthesis of Porous Mo2C Sponge by Vapor-Phase Condensation and in Situ Carburization of MoO3. *Journal of Alloys and Compounds* **2010**, *489*, 36–41.

182. Xu, C.; Wang, L.; Liu, Z.; Chen, L.; Guo, J.; Kang, N.; Ma, X.-L.; Cheng, H.-M.; Ren, W. Large-area High-quality 2D Ultrathin Mo_2C Superconducting Crystals. *Nat. Mater.* **2015**, *14*, 1135–1141.

183. Ojha, K.; Saha, S.; Kolev, H.; Kumar, B.; Ganguli, A. K. Composites of Graphene-Mo_2C Rods: Highly Active and Stable Electrocatalyst for Hydrogen Evolution Reaction. *Electrochimica Acta* **2016**, *193*, 268–274.

184. Valk, P.; Nerut, J.; Tallo, I.; Tee, E.; Vaarmets, K.; Romann, T.; Kurig, H.; Palm, R.; Lust, E. Structure and Stability of Partially Chlorinated Molybdenum Carbide Composite Materials Synthesised via High Temperature Chlorination. *Electrochimica Acta* **2016**, *191*, 337–345.

185. Karge, H. G.; Weitkamp, J. *Characterization I*; Springer: Berlin, 2003.

186. King, D. A.; Richardson, N. V.; Holloway, S. Vibrations at Surfaces 1985: Proceedings of the Fourth International Conference, Bowness-on-Windermere, United Kingdom, 15-19 September 1985; Elsevier: Amsterdam, 1986.

187. Ye, G.; Gong, Y.; Lin, J.; Li, B.; He, Y.; Pantelides, S. T.; Zhou, W.; Vajtai, R.; Ajayan, P. M. Defects Engineered Monolayer MoS_2 for Improved Hydrogen Evolution Reaction. *Nano Lett.* **2016**, *16*, 1097–1103.

188. Lin, H.; Shi, Z.; He, S.; Yu, X.; Wang, S.; Gao, Q.; Tang, Y. Heteronanowires of MoC–Mo_2C as Efficient Electrocatalysts for Hydrogen Evolution Reaction. *Chem. Sci.* **2016**.

189. Chhetri, M.; Maitra, S.; Chakraborty, H.; Waghmare, U. V.; Rao, C. N. R. Superior Performance of Borocarbonitrides, $B_xC_yN_z$, as Stable, Low-Cost Metal-Free Electrocatalysts for the Hydrogen Evolution Reaction. *Energy Environ. Sci.* **2016**, *9*, 95–101.

190. Li, D. J.; Maiti, U. N.; Lim, J.; Choi, D. S.; Lee, W. J.; Oh, Y.; Lee, G. Y.; Kim, S. O. Molybdenum Sulfide/N-Doped CNT Forest Hybrid Catalysts for High-Performance Hydrogen Evolution Reaction. *Nano Lett.* **2014**, *14*, 1228–1233.

191. Pham, K.-C.; Chang, Y.-H.; Mcphail, D. S.; Mattevi, C.; Wee, A. T. S.; Chua, D. H. C. Amorphous Molybdenum Sulfide on Graphene–Carbon Nanotube Hybrids as Highly Active Hydrogen Evolution Reaction Catalysts. *ACS Appl. Mater. Interfaces* **2016**, *8*, 5961–5971.

192. Seol, M.; Youn, D. H.; Kim, J. Y.; Jang, J.-W.; Choi, M.; Lee, J. S.; Yong, K. Mo-Compound/CNT-Graphene Composites as Efficient Catalytic Electrodes for Quantum-Dot-Sensitized Solar Cells. *Adv. Energy Mater.* **2013**, *4*.